Dissertation

submitted to the
Combined Faculties of the Natural Sciences and Mathematics
of the Ruperto Carola University of Heidelberg, Germany
for the degree of
Doctor of Natural Sciences

put forward by
Dipl.-Phys. Judith Elena Jordan
born in Tübingen, Germany

Oral examination: 24 November 2015

High-resolution Doppler laser spectroscopy of the laser cooling candidate La$^-$

Referees: **Priv.-Doz. Dr. Alban Kellerbauer**
Prof. Dr. Selim Jochim

Kurzzusammenfassung

Der Übergang zwischen dem $5d^26s^2$ $^3F^e_2$ Grundzustand und dem gebundenen angeregten $5d6s^26p$ $^3D^o_1$ Zustand des negativen Lanthan-Ions wurde zum Laserkühlen vorgeschlagen, was bis zum heutigen Tag für negative Ionen noch nie erfolgreich durchgeführt wurde. Das Laserkühlen von negativen Ionen hat das Potential, ultrakalte Ensembles von beliebigen negativen Ionen zu erzeugen. In dieser Arbeit wird der oben genannte Übergang an einem Ionentrahl aus negativen Lanthan-Ionen mittels hochaufgelöster Laserspektroskopie untersucht. Für die Schwerpunktsfrequenz des Übergangs ergab die Messung 96.592 80(10) THz. Sieben der neun zu erwartenden Hyperfeinstrukturübergänge wurden aufgelöst. Die beobachteten Resonanzen wurden durch einen Fit eindeutig den vorausgesagten Hyperfeinübergängen zugeordnet. Aus der ermittelten Hyperfeinstruktur wurde geschlossen, dass für das Kühlen und Rückpumpen aller Hyperfeinzustände nur drei Laserfrequenzen benötigt würden. Weiterhin deuten die beobachteten relativen Übergangsamplituden darauf hin, dass die Resonanzen bei einer Laserintensität von 45 Wm^{-2} bereits gesättigt sind. Eine grobe Abschätzung des Wirkungsquerschnitts für die Anregung bestätigt, dass La^- ein guter Kandidat für die erste Laserkühlung von negativen Ionen ist.

Abstract

The bound–bound transition from the $5d^26s^2$ $^3F^e_2$ ground state to the $5d6s^26p$ $^3D^o_1$ excited state in negative lanthanum has been proposed as a candidate for laser cooling, which has not yet been achieved for negative ions. Anion laser cooling holds the potential to allow the production of ultracold ensembles of any negatively charged species. In this work the aforementioned transition was studied in a beam of negative La ions by high-resolution laser spectroscopy. The center-of-gravity frequency of the transition was measured to be 96.592 80(10) THz. Seven of the nine expected hyperfine structure resonances were resolved. The observed peaks were unambiguously assigned to the predicted hyperfine transitions by a fit. From the determined hyperfine structure for this transition it was concluded that only three lasers would be required to cool and re-pump all hyperfine levels. Furthermore, the observed relative transition amplitudes suggest that in resonance the transitions are saturated at a laser power of 45 Wm^{-2}. A rough estimate of the transition cross section confirms that La^- is a promising candidate for the first laser cooling of negative ions.

Acknowledgments

At this point I want to thank all the people who have supported and encouraged me during my PhD project. First of all, I most sincerely thank my advisor Alban Kellerbauer for the PhD position in his group, and the interesting topic, for all the support, the helpful advice, the inspiring discussions and for encouraging me to present the progress of this work on international conferences. Sincerely thanks to my co-advisors Andreas Wolf and Selim Jochim for the advice and the discussions. I gratefully acknowledge the generous financial support from the International Max Planck Research School for Precision Tests of Fundamental Symmetries (IMPRS PTFS) and the Heidelberg Graduate School for Fundamental Physics (HGSFP) which allowed me to participate in national and international conferences and in inspiring winterschools. I acknowledge the support by Klaus Blaum, in particular the accommodation in his department offering us such excellent working conditions, and the financial support for the participation in the ’Women in Science Symposium 2015’ in Uppsala which gave me the opportunity to exchange experience with women scientists from various disciplines and of various nationalities.

Mille grazie to my lab- and officemate Giovianni Cerchiari who supported our project through thick and thin, for the lively discussions, for working with me so many days and nights in the lab, for advancing our project with his ingenious ideas and of course, for teaching me some useful Italian words. Warmest thanks to Anke Heilmann, Sophia Haude and Lisa Ringena for the successful and pleasant teamwork and the support for building up the experiment.

I’m indebted to José Crespo for the invaluable pieces of advice and the inspiring discussions. In particular, for the help with the channeltron detector and the Paul trap. I sincerely thank Stephan Fritzsche and Wesley Walter for the collaboration and the helpful discussions. Many thanks to Manfred König for the technical support with the ion source, Holger Kreckel and Florian Grussie for the drawings and the advise how to build the electrostatic deflector, Thorsten Spranz, Martin Beckmann, Uwe Zeiske and all members of the MPIK workshops for the technical support. I also thank the members of the AEgIS collaboration for teaching me experimental methods, for giving me insights into the AEgIS project, for the great collaboration and the inspiring discussions. I’m indebted to Bastian Sikora, Giovanni Cerchiari, Gregor Coennen, Hendrik Bekker, Lisa Schmöger, Sabina Pürckhauer for the careful proof reading. Last but not least, heartfelt thanks to Moritz Köhler and my family for lending me an ear at any time, for the encouragement and the proof reading.

Contents

Chapter 1

Introduction

1.1 Negative ions

Negative ions are everywhere. They are essential for the function of our bodies, they are present in the air of the atmosphere, in the oceans and have even been found in space in interstellar clouds. Therefore they are important in many fields of physics, such as plasma physics, biophysics, atmospheric science and astrophysics [Smit1978, Gupt2007, SK2014, Agún2008]. Negative ions (anions) are atoms or molecules with an extra electron attached. When an electron approaches or penetrates a neutral atom the bound electrons are repelled by the Coulomb force. The positive charge of the nucleus ceases to be fully shielded, so the additional electron can be bound by the nuclear potential. The binding potential of negative ions is short-ranged and shallow. Therefore, atomic anions are weakly bound systems compared to positive ions. The binding energy, also called *electron affinity*, of fluorine $E_{\mathrm{EA}} = 3.99$ eV is the strongest among the atomic anions. The binding energies for different elements vary strongly and can be found in Refs. [Hoto1975, Hoto1985, Ande1999]. Some elements, like He and other noble gases for example, only form metastable anions. The anions autodetach with a relatively long lifetime of ten to hundreds of microseconds, depending on the fine structure state of the ion [Rein2009]. But even Ca and heavier alkaline earth atoms can form stable negative ions [Pegg1987]. Polarization effects and electron–electron correlation play an important role in anions [Pegg2007]. Electron–electron correlation can only be described approximately. In particular for multi-electron systems the theoretical description is challenging, therefore electron affinities of negative ions are an important test for theoretical calculations.

In the last decades a large number of theoretical and experimental studies on the structure and the spectra of negative ions were performed [Sche1989, Pegg2004, Ande2004]. New lasers opened the way for spectroscopic studies at wavelengths from the visible range up to the mid-infrared. Photodetachment spectroscopy and photo-electron spectroscopy are the preferred ways to study anions. Both techniques measure the detachment of the additional electron. In photodetachment spectroscopy the laser frequency is varied and the number of neutralized atoms is counted for each photon energy. In photo-electron spectroscopy the kinetic energies of the photoelectrons are recorded for a fixed photon energy. Even more information about electron–electron correlation can be extracted if the angular distribution of the photoelectrons is also recorded. From the obtained spectra not only the binding energy can be determined, but also information about the internal structure can be deduced.

In contrast to neutrals and positive ions the photoelectron leaves behind a neutral atom. Thus, it is not disturbed by a Coulomb field and can be treated approximately as a plane wave. At the onset of photodetachment the photoelectron is in the lowest angular momentum state. The threshold behaviour of the detachment cross section σ_{det} is approximately described by the Wigner threshold law [Wign1948].

$$\sigma_{\mathrm{det}} \propto E^{l+1/2}, \tag{1.1}$$

where E is the kinetic energy of the outgoing electron and l its angular momentum. This can be used to identify the configuration from which the electron originates. If the detached electron comes out of an s-shell there will be a steep increase of the detachment cross section. In contrast, if the electron carries angular momentum the increase is shallower.

Most negative ions have only a single bound state, but for some anions, like Pd^- for instance, intermediate states were observed as resonances in photoelectron spectra [Feig1981]. The photon energy needed to detach an electron from an excited state is lower than the energy needed to detach an electron from the ground state. Thus in photodetachment spectroscopy, a detachment resonance is observed at a photon energy lower than the binding energy of the ground state. In photoelectron spectroscopy electrons are observed with larger kinetic energy than the kinetic energy of electrons detached from the ground state. The population probability of these higher-lying states follows a Boltzmann distribution.

If an atomic anion has more than one bound state, these levels most often belong to the same fine structure multiplet. Transitions between them are electric-dipole (E1) forbidden. Thus, electric-dipole transitions usually can not be found in atomic anions. Forbidden transitions are difficult to observe because of their low transition rates. Over the past few decades numerous studies were launched to find opposite-parity bound states in an atomic negative ion, which would allow electric-dipole transitions. Ever-increasing computing power allowed to study more and more complex systems in which dipole transitions are more likely, because of the larger number of bound states. The first one to be studied was in Os^-. Norquist and Beck performed relativistic configuration interaction (RCI) calculations on the electron affinity of transition metals. They also calculated the electron affinity for Os^- and pointed out the possibility for bound excited states of opposite parity to the ground state [Norq1999]. The existence of dipole transitions between bound states in negative osmium was confirmed experimentally in 2000 when Bilodeau and Haugen measured the spectrum of Os^- for the first time and found two resonances, one from a bound–bound transition and one between the ground state and a metastable auto-detaching state [Bilo2000].

This important observation led to the idea to laser cool negative ions. Studying negative ions at ultracold temperatures is desirable because precision spectroscopy and other fascinating experiments could be performed. Until today, such experiments, like ultra-cold charge exchange and studies on ultra-cold plasmas for example, have been carried out with positive ions and neutral atoms, but they have not been possible for negative ions. Precision measurements with negative ions could give new insights and more precise tests on theories of many-electron systems. Laser cooling one anion species could clear the way for cooling a vast range of anions by sympathetical cooling. When two ion species are trapped in the same trap, the cold species cools the other species by momentum transfer via Coulomb interactions. This technique has been successfully applied to positive ions [Boll1988].

Even in antimatter research, ultracold negative ions would be of great use. Experimental CPT tests at unprecedented precision could set further constraints on physics beyond the Standard Model. The precision of measurements is mainly limited by the temperature of the studied antimatter systems. Gravity measurements with precision better than 1%, as proposed by the AEgIS Collaboration at CERN, as well as competitive CPT tests by spectroscopy will necessitate antihydrogen temperatures colder than 100 mK [Kell2008]. The temperature of the produced antihydrogen is mainly determined by the temperature of antiprotons, because they are much heavier than the positrons. In order to reach lower temperatures than the trap environment, antiprotons could be sympathetically cooled by negative ions, as proposed by Kellerbauer and Walz [Kell2006]. Since antiprotons are the antiparticles of protons, they annihilate with protons or neutrons whenever they come in contact with ordinary matter. Therefore it is impossible to sympathetically cool antiprotons with atomic positive ions or neutral atoms. Negative ions and antiprotons repel each other, this way annihilation can be prevented. Storage in the same volume is possible, which is the basis for sympathetic cooling.

Until today, there is no method to cool negative ions much below temperatures of the surrounding environment. Ions can either be cooled in a beam, where the transverse momentum spread is reduced by cooling, or in an ion trap, where the total kinetic energy is reduced. Common traps for charged particles are Paul traps, which are electric radiofrequency traps and Penning traps, which are electromagnetic traps. There are several established cooling methods for ions in traps.

Those are

- Buffer gas cooling: particles exchange heat in collisions with a cold buffer gas;
- Resistive cooling: particles lose energy because the induced mirror charge creates a resistance in the trap electrode;
- Adiabatic cooling: a cloud of particles is expanded adiabatically and thus cooled;

- Radiative cooling: light particles, i.e. electrons, irradiate synchrotron radiation during their fast motion in Penning traps and lose energy;
- Evaporative cooling: the hottest particles are removed, reducing the average temperature;
- Laser cooling: the particles absorb red-detuned counter-propagating photons and isotropically scatter them at their resonance frequency;
- Stochastic cooling: the motion of the particles is detected and fed back to an electrode on the subsequent path of the ions to correct for their motion;
- Sympathetic cooling: the particles interact with a trapped, colder species of particles and transfer energy via collisions or Coulomb interactions.

For anions, there is the attractive method to cool sympathetically with electrons [Li1997], provided that the binding energy is large enough that they are not detached in collisions. The electrons self-cool by radiative cooling due to their cyclotron motion in the trap and can be further cooled to ≈ 0.85 K by "feed-back cooling" [D'Ur2003], which is a kind of stochastic cooling. Sympathetic cooling of negative ions by electrons is more efficient than buffer gas cooling, because they interact by long-range Coulomb interactions instead of the short-range collision interaction between buffer gas atoms and negative ions [Li1997]. The lowest temperature reachable by electron cooling is about ≈ 1 K [Hu2007].

1.2 Laser cooling

Laser cooling methods are routinely used to cool positive ions and neutral atoms to temperatures in the μK range. Laser Doppler cooling was proposed in 1975 independently by Hänsch and Schawlow and Wineland and Dehmelt [Hä1975, Wine1987]. The basic principle is that a slightly red-detuned laser is shined onto the atoms or ions to be cooled. Only those particles can absorb the laser for which the Doppler shift matches the detuning. Those are exactly the ones which move toward the laser. Using the Doppler shift a velocity-selective absorption is reached. The absorption of a photon leads to a momentum change of $\Delta p_{\mathrm{abs}} = -\hbar k$, where k is the photon's wave number. After the excitation the ions spontaneously re-emit a photon at their resonance frequency in an arbitrary direction. The momentum transfer by the isotropic re-emission of this process averages out over many emissions $\langle \Delta p_{\mathrm{spon}} = 0 \rangle$. In total the atoms experience a radiation force which decelerates them, the average kinetic energy of the ions is reduced, and the ions are cooled. Since the momentum transfer per absorbed photon is relatively small, a transition with a high spontaneous decay rate is needed for efficient cooling.

For example, for Mg^+ ions at 600 K the absorption–emission process of the red-detuned photons on the singlet resonance at 285.2 nm must occur about 3×10^4 times to bring the atom to rest. The radiative lifetime of the excited state is 2 ns. This allows a cooling time of the order of 10^{-5} s with an appropriate laser sufficiently powerful to saturate the transition [Hä1975].

The optimal laser frequency for cooling is on the lower half of the Doppler line width. In general, the optimal detuning is half the line width $\Gamma/2$. At high temperature, the line width is dominated by Doppler broadening, therefore the laser frequency has to be adjusted during the cooling process as the Doppler width decreases. The laser does not only cool, but also heats if photons are absorbed by ions moving away from the laser. Their probability for absorption is smaller, but still larger than zero. The minimum temperature that can be reached with Doppler cooling is reached when there is equilibrium between heating and cooling, that is $k_B T_D = h\Gamma/2$, where T_D is the so-called Doppler temperature. For many atoms the Doppler temperature is several hundred µK. However the spontaneous emission processes also lead to a recoil. As a consequence the ions move in a random walk in the momentum-space, corresponding to a recoil temperature $k_B T_{\text{rec}} = \Delta p_{\text{abs}}^2/2M = \hbar^2 k^2/2M$, where M is the mass of the ion. The recoil temperature is usually several µK and cannot be reached by usual Doppler cooling, but only by more sophisticated cooling methods, such as Sisyphus cooling or Raman cooling [Dali1985, Monr1995]. For example, for Mg^+ the Doppler temperature is about 2 mK, whereas the recoil temperature is about 5 µK.

For cooling, ions need to be kept within the volume irradiated with the laser. This is done by trapping. The most common traps are magneto-optical traps for atoms and Paul or Penning traps for ions. The first experiments in 1978 were performed by Wineland, Drullinger and Walls cooling Mg^+ ions in a Penning trap [Wine1978] and by Neuhauser, Hohenstatt, Toschek and Dehmelt who carried out sideband laser cooling on Ba^+ ions in a Paul trap [Neuh1978]. Sideband cooling is explained in the following.

In a Paul trap the ions move in a three-dimensional ellipsoidal potential well

$$U(x, y, z) = U_0(x^2 + y^2 + z^2)/(4Z_0^2) \tag{1.2}$$

with a well defined axial oscillation frequency ω_i, which depends on the trapping voltage and the mass of the trapped ions. The z-motion is the superposition of the free secular motion $\bar{z}(t)$, and a forced micromotion $\zeta(t)$ given by

$$z(t) = \bar{z}(t) + \zeta(t) = z_0 \cos\omega_i t + \zeta_0 \cos\omega_i t \cos\Omega t, \tag{1.3}$$

where Ω is the frequency of the trap potential and ω_i is the axial oscillation frequency. An advantageous effect for laser cooling is, that an ion oscillating in the trap perceives sidebands generated by the Doppler effect $\omega_n = \omega \pm n\omega_i,\ \ n = 0, 1, 2, ...$ in addition to the incident laser frequency ω.

The apparent sidebands toward higher frequency $\omega_n' = \omega + n\omega_i$ can be used for sideband cooling. If the frequency of such a sideband falls close to the resonance frequency ω_0 of the ion, the ion can absorb a photon of frequency ω. The frequency of the re-emitted photons is on average ω_n', that is the ions re-emit photons of a higher energy. The energy loss per scattering event is $\Delta E = \hbar(\omega_n' - \omega) = \hbar n\omega_i$. Absorption of photons from the

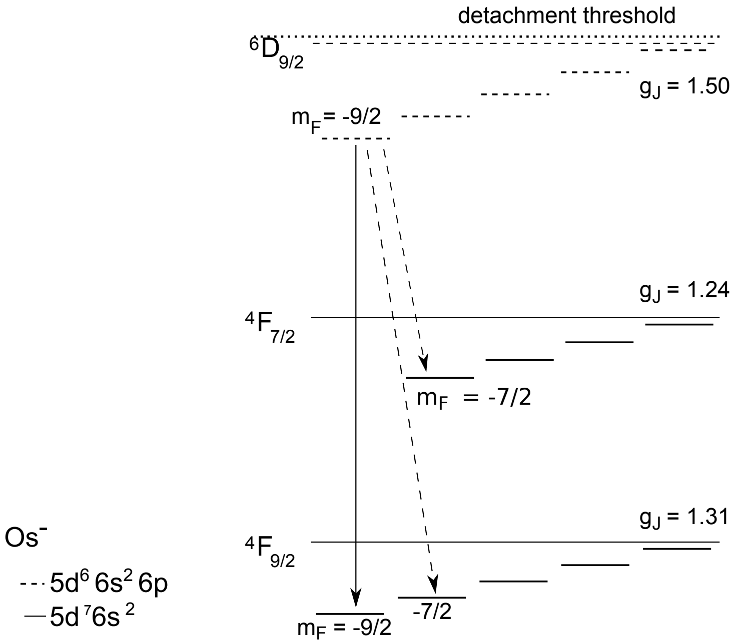

Figure 1.1: Schematic energy level diagram of Os^- with Zeeman levels. The solid arrow indicates the laser cooling π-transition and the dashed arrows indicate the decay channels to dark states. Figure according to Ref. [Kell2014].

red sidebands $\omega_n = \omega - n\omega_i$ will heat the ion plasma. Therefore, for sideband cooling a red-detuned laser ideally adjusted to the sidebands is used. For an ion plasma Coulomb collisions provide a fast thermalization of the plasma on a time scale of ≈ 1 ms, so that only a single laser is needed.

1.3 Candidates for negative ion laser cooling

Until today laser cooling of negative ions has never been demonstrated, due to a lack of suitable cooling transitions. As of 2015 there are three known anions with bound excited states of opposite parity, namely the anions of osmium, cerium and lanthanum. To get an overview about their suitability for laser cooling these candidates are presented in detail in the following.

Os^-

Os^- was the first atomic anion in which a bound–bound E1 transition was observed experimentally. Following the aforementioned theoretical predictions [Norq1999], Bilodeau and Haugen carried out resonant laser photodetachment spectroscopy on Os^- and found a bound–bound E1 transition. They determined the binding energy of the $5\mathrm{d}^7\,6\mathrm{s}^2\,4\mathrm{F}_{9/2}$

ground state to be 1.077 80(12) eV, an excited state of opposite parity with binding energy 11.48(12) meV, and a low-lying shape resonance unbound by 3.52(12) meV. Furthermore, they made a rough estimate of the bound–bound transition cross section to be of the order of $10^{-16}\mathrm{cm}^2$ at a line width of $\Gamma = 5.1$ GHz, resulting in an Einstein coefficient for the spontaneous decay of $A_{21} \approx 10^4$ 1/s [Bilo2000]. Based on these first observations, Os^- seemed to be a promising laser cooling candidate.

However, the total angular momentum quantum number of the excited state remained unknown until it was measured by high-resolution collinear laser spectroscopy at the Max Planck Institute for Nuclear Physics in Heidelberg, Germany. The higher precision was achieved with a narrower laser bandwidth and by using a sophisticated setup. In this experiment the ions were excited with a laser and weakly bound excited ions were detached in an electric field [Warr2009]. This improved the detection efficiency by up to two orders of magnitude compared to two-photon detachment. In this way Warring *et al.* measured the transition frequency at a precision improved by about two orders of magnitude: $f_0 = 257.831\,190(35)$ THz [wavelength 1162 747 06(16) nm] [Warr2009]. The same group performed hyperfine structure measurements on $^{187}\mathrm{Os}^-$ and $^{189}\mathrm{Os}^-$. In the spectrum of $^{189}\mathrm{Os}^-$ they observed ten hyperfine transition peaks, allowing them to identify the upper state as $^6\mathrm{D}_{9/2}$ [Fisc2010]. They also measured the excitation cross section $\sigma = 2.5(7) \times 10^{-15}$ cm^2 at a line width of 45 MHz. This resulted in an Einstein coefficient $A_{21} \approx 330$ 1/s, lower than expected from the previous estimate. The low value for the spontaneous emission is commensurate with a spin-forbidden E1 transition. Finally, they also measured the isotope shift between the 6 isotopes and the Zeeman splitting in $^{192}\mathrm{Os}^-$ [Kell2011, Kell2014].

These results allowed a clear judgment about the suitability of Os^- for laser cooling. The transition between the $^4\mathrm{F}_{9/2}$, $M_J = -9/2$ and $^6\mathrm{D}_{9/2}$, $M_J = -9/2$ levels can be used for laser cooling, as shown in Fig. 1.1. Thanks to the large number of isotopes, an isotope without nuclear spin, and thus without hyperfine splitting, can be chosen for laser cooling. However, with the laser used for the spectroscopic studies and at a detuning of half the laser bandwidth, the cooling rate may be as low as 50 Hz. Thus, when starting from liquid-nitrogen temperature (≈ 80 K), cooling to the Doppler temperature would take prohibitively long. Therefore, pre-cooling to liquid-helium temperature may be required, resulting in a cooling time of roughly 5 min [Warr2009].

One additional difficulty of Os^- is the need for repumping the $^4\mathrm{F}_{7/2} \rightarrow {}^6\mathrm{D}_{9/2}$ transition even in the absence of a magnetic field, since the branching ratio for the transition to this dark state is estimated to be about 8–12% [O'Ma2010]. In a magnetic field the $^4\mathrm{F}_{9/2}$, $M_J = -7/2$ and $^4\mathrm{F}_{7/2}$, $M_J = -7/2$ dark states need to be repumped with two other narrow-bandwidth lasers [Kell2014]. In particular because of the long cooling time, Os^- does not seem to be an ideal candidate for laser cooling.

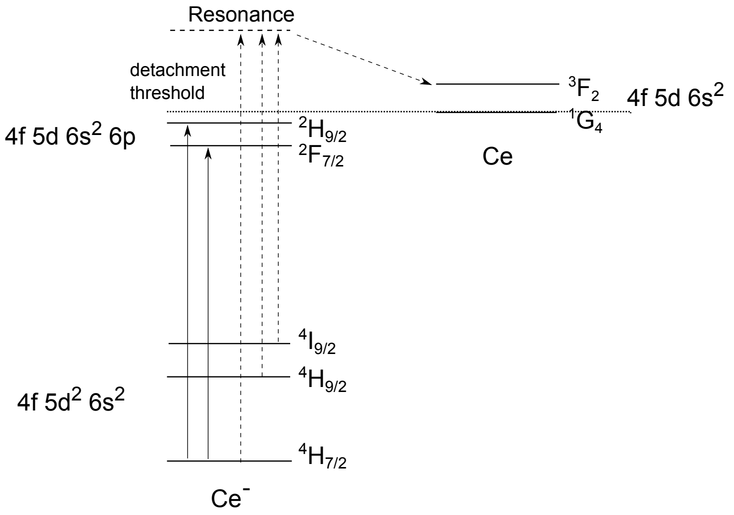

Figure 1.2: Schematic energy level diagram of Ce$^-$ with transitions to bound states indicated by solid arrows and transitions to the quasi-bound state indicated with dotted arrows. Figure according to Ref. [Walt2011].

Ce$^-$

The negative cerium ion was the second anion confirmed to have bound states of opposite parity, for which electric-dipole transitions are allowed [Davi2002, Walt2007, Walt2011]. Cerium is a rare-earth element. The two most abundant isotopes of Ce are ^{140}Ce (88.5%) and ^{142}Ce (11.1%). They both do not carry nuclear spin. Walter *et al.* performed photodetachment spectroscopy in a crossed laser beam – ion beam setup, and Pan and Beck performed theoretical calculations of the photodetachment cross sections with which the transitions responsible for the measured peaks were identified [Walt2011]. The electron affinity of Ce$^-$ was determined to be 0.628(10) eV, the binding energy of the first excited state ^{4}H$_{9/2}$ 0.530(10) eV. The binding energies of the odd states are 32 meV for $J = 7/2$ and 30 meV for $J = 9/2$ [Walt2011]. A schematic energy level diagram for Ce$^-$ is shown in Fig. 1.2. Two out of the twelve observed transition peaks originate from electric-dipole transitions between bound states of Ce$^-$. One is the $4f\,5d^2\,6s^2\,{}^4H_{7/2} \rightarrow 4f\,5d\,6s^2\,6p\,{}^2F_{7/2}$ transition at 0.60023(3) eV [145.135(15) THz], the other the transition $4f\,5d^2\,6s^2\,{}^4H_{7/2} \rightarrow 4f\,5d\,6s^2\,6p\,{}^2H_{9/2}$ transition at 0.61816(3) eV [149.470(15) THz] [Walt2011], corresponding to wavelengths of about 2 μm. Both E1 transitions are spin-forbidden and the upper state can decay to dark states. Therefore Ce$^-$ is of restricted use for laser cooling applications.

La$^-$

An alternative laser cooling candidate is the negative ion of lanthanum. La is, like Ce, a rare-earth element. The prevalent isotope ^{139}La with an abundance of $> 99.9\%$ carries

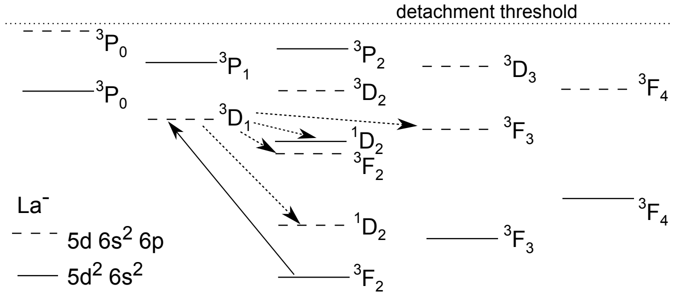

Figure 1.3: Theoretically calculated energy level diagram of La$^-$ by O'Malley and Beck with the laser cooling transition indicated by the solid arrow. The possible decay channels to dark states are indicated by dotted arrows. Figure according to Ref. [O'Ma2010].

a nuclear spin of[1] $I = 7/2$. The bound states of opposite parity in La$^-$ were predicted as early as 1991 by Vosko *et al.* [Vosk1991], who performed density-functional-theory calculations of this "unique anion", and even before, in 1976, the electron affinities of the lanthanides had been estimated by Angelov with a value of 0.5 eV for La$^-$ [Ange1976]. Covington carried out measurements of the photoelectron spectrum of La$^-$, which confirmed that there is at least one bound excited state. He determined the value for the electron affinity of La to be 0.47(2) eV [Covi1998]. In 2009 and 2010 O'Malley and Beck performed detailed relativistic configuration interaction (RCI) calculations to determine lifetimes and branching ratios of excited states in La$^-$, Os$^-$, Lu$^-$, Lr$^-$, and Pr$^-$, leading to the energy level diagram of La$^-$ shown in Fig. 1.3 [O'Ma2009]. The calculations showed that La$^-$ is probably the best candidate among the lanthanide and actinide anions. This recommendation was based on the observation that there is an almost ideal two-level system, a $^3\mathrm{F}_2^e \rightarrow {}^3\mathrm{D}_1^o$ spin-allowed E1 transition whose upper state has three negligible M1/E2 decay branches and a weak spin-forbidden E1 branch to the excited $^1\mathrm{D}_2^e$ level. The branching ratio was estimated to be >99.98% back to the ground level and the lifetime of the upper state to be 34 µs. The Einstein A_{12} coefficient was predicted to be 2.9×10^4 s^{-1} for the cooling transition and 3.7 s^{-1} for the spin-forbidden transition to the dark state [O'Ma2010]. According to the calculations, the spontaneous decay is approximately two orders of magnitude faster than for Os$^-$. However the transition energy in La$^-$ is only about a third of the transition energy in Os$^-$, which reduces the momentum transfer per scattering event. Unfortunately the hyperfine structure was not considered in the calculations.

One possible problem of laser cooling of anions in RF or Penning traps is two-photon detachment. When the ions are neutralized they leave the trap and are lost. Pan and Beck investigated possible detachment channels in La$^-$. Fortunately, their analysis showed no big resonance state according to Fano's theory to be present. Detachment is possible

---

[1] The other naturally occurring isotope ^{138}La with a low abundance of 0.089% carries a nuclear spin of $I = 5$ and the long lived isotope ^{137}La a nuclear spin of $I = 7/2$; the other isotopes are short lived with lifetimes < 41 h. [Inge1973, Magi2006]

via 5d 6s^2 6p ^{3}D$_1$ $\rightarrow$ 5d 6s^2 ^{2}D$_{3/2}$ + ϵl_j transitions. Based on this, the detachment cross section was estimated to be about 10^{-17} cm^2, the same as for Os$^-$ [Pan2010].

Recently Walter *et al.* performed an experimental survey of La$^-$. They used photodetachment spectroscopy with a tunable pulsed optical parametric oscillator (OPO) pumped by a Nd:YAG laser in a crossed-beam setup. The detachment was done in a two-step process of one-photon excitation followed by absorption of a second photon to detach an electron. As expected from the predictions, La$^-$ showed the richest bound-state spectrum ever observed for an negative atomic ion [Walt2014]. The resonances of twelve transitions in the energy range 295 . . . 585 meV were identified and assigned to the calculated levels of Ref. [O'Ma2010]. The proposed laser cooling transition $^3\mathrm{F}_2^e \rightarrow {}^3\mathrm{D}_1^o$ was observed at 96.5793(73) THz (excitation energy ≈ 399 meV) [Walt2014]. This study is a very important prerequisite for laser cooling of La$^-$, however, due to the large bandwidth of the pulsed excitation laser ($\Gamma_L = 3$ GHz), the hyperfine structure of the transition was not resolved.

In order to identify the specific hyperfine transition(s) most suitable for laser cooling, the full hyperfine structure as well as the relative strengths of all allowed transitions between the ground and excited hyperfine states must be determined. For this purpose, in this work high-resolution collinear laser spectroscopy on La$^-$ was carried out.

Chapter 2

Theoretical background

The theory of atomic spectra, as it was developed during the last century, can also be applied to negative ions. Despite the differences in the binding potential, the fine structure and the hyperfine structure are described by the same formalism and with the same quantum numbers as used for neutrals and positive ions. The transition energies in anions are shifted with respect to the energies in neutral atoms, and the most striking difference is the absence of the infinite number of discrete levels. There is no Rydberg series which provides a complex intermediate resonance structure. Therefore, in the case of anions the detachment cross section always starts from zero at threshold.

In contrast to most of the current studies on negative ions, in this work the focus is not just on photodetachment. Instead, one of the dipole-allowed bound–bound transitions in La$^-$ is investigated, which make La$^-$ such a unique anion. In the following a few general aspects of atomic physics which are relevant for this work are discussed. Since the theoretical approaches hold for ions and atoms as well, these words can be exchanged, if not this is stated explicitly.

2.1 Hyperfine structure

The hyperfine structure arises from the interaction of the electron magnetic moment with the nuclear spin. The interaction potential is approximated by

$$V_{\text{mag}} = -\vec{\mu}_I \cdot \vec{H}(0), \tag{2.1}$$

where $\vec{\mu}_I$ is the magnetic-dipole moment of the nucleus and $\vec{H}(0)$ is the magnetic field created by the electron cloud at the position of the nucleus. The magnetic field $\vec{H}(0)$ is usually anti-parallel to the total angular momentum of the electrons $\vec{J}$. The next higher order of the nuclear magnetic moment, the octupole moment, can in most cases be neglected. The absolute values of $\vec{\mu}_I$ and the nuclear spin $\vec{I}$ are connected by the relation $\mu_I = m_e/m_p \mu_B I g_I = \mu_K I g_I$, where m_e is the electron mass, μ_B the Bohr magneton, m_p

the proton mass and $\mu_K = m_e/m_p\mu_B$ the nuclear magneton. The magnetic interaction can be treated as a perturbation to the potential energy of the ion. In order to obtain the magnetic energy ΔW_{mag}, a time average over the magnetic field at the position of the nucleus is taken $\langle\vec{H}(0)\rangle$. With this the additional energy is [Kopf1965]

$$\Delta W_{\text{mag}} = -\mu_I\langle\vec{H}(0)\rangle \cos[\vec{\mu}_I, \vec{H}(0)]. \tag{2.2}$$

Due to the magnetic interaction, $\vec{I}$ couples to $\vec{J}$, forming the total angular momentum of the ion $\vec{F} = \vec{I} + \vec{J}$. Using the z-component of $\vec{\mu}_I$, and the z-component of the average magnetic field, the expression for the interaction energy is given by [Kopf1965]

$$\Delta W_{\text{mag}} = AIJ\cos(\vec{I}, \vec{J}) = AC/2, \tag{2.3}$$

where $C = F^2 - I^2 - J^2 = F(F+1) - I(I+1) - J(J+1)$ and A is the magnetic-dipole hyperfine interaction constant

$$A = \frac{\mu_I\langle\vec{H}(0)\rangle}{IJ} = \frac{\mu_K g_I\langle\vec{H}(0)\rangle}{J}. \tag{2.4}$$

The value of A varies from fine-structure term to term. For closed electronic shells and closed sub-shells $A = 0$.

Another contribution to the hyperfine structure arises from the shape of the nucleus. The nucleus is not point-like, but has a certain extent. This leads to a deviation from the simple Coulomb interaction potential. The difference in the interaction potential for a point-like nucleus and an extended nucleus with charge density $e\rho_K$ is given by

$$V_{el} = e\int \rho_K\phi_e dV - \frac{Ze^2}{4\pi\epsilon_0}\int \frac{\rho_e}{r}dV \ , \tag{2.5}$$

where $e\rho_e$ and ϕ_e are the charge density and the electrostatic potential of the electron cloud and ϵ_0 is the electric field constant. In the following, the nucleus is centered at the origin. Only those electrons with zero charge density at the position of the nucleus are considered. For those electrons ϕ_e is Taylor expanded in the spatial coordinates at the position of the nucleus. Since nuclei have no measurable electric-dipole moment, the only contribution is from the electric-quadrupole moment Q of the nucleus, which interacts with the gradient of the electric field from the electrons. In the coordinate system of the nucleus the quadrupole moment is given by [Kopf1965]

$$Q = e\int r^2(3\cos^2\Theta - 1)\rho_K dV. \tag{2.6}$$

Q has the dimension of an area and is a measure for the deviation of the shape of the nucleus from a sphere. The additional electric energy to the ionic potential is

$$\Delta W_Q = \frac{eQ\overline{\phi_{JJ}(0)}}{4}(\frac{3}{2}\cos^2\theta - \frac{1}{2}) = \frac{B}{4}\left(\frac{3}{2}\cos^2(\vec{I}, \vec{J}) - \frac{1}{2}\right), \tag{2.7}$$

where

$$B = eQ\overline{\phi_{JJ}(0)} \tag{2.8}$$

is the quadrupole interaction constant and $\overline{\phi_{JJ}(0)}$ is the electric-field gradient of the electrons at the position of the nucleus with rotational symmetry around J. For small values of I, J and F the Casimir formula can be applied, resulting in

$$\Delta W_Q = \frac{B}{4}\frac{3/2C(C+1) - 2I(I+1)J(J+1)}{I(2I-1)J(2J-2)}. \tag{2.9}$$

Complete electronic shells and sub-shells do not contribute to the electric-quadrupole interaction. Further, nuclei with $I \leq 1/2$ have a spherically symmetric charge distribution and therefore $\Delta W_Q = 0$.

In the expression for the electric-quadrupole interaction Eq. (2.7) contributions from terms with spherically symmetric charge distributions, such as s and $p_{1/2}$ terms, are not included. The s-electrons generate a non-vanishing charge density in the position of the nucleus which leads to the well-known isotope shift. Here V_{el} is independent from the angle between $\vec{I}$ and $\vec{J}$. This means the interaction shifts all of the fine-structure terms and therefore is only measurable when different isotopes are compared.

To obtain the total energy of the hyperfine-structure terms W_F for one specific isotope, the magnetic-dipole and electric-quadrupole energy are added to the energy of the fine-structure term W_J.

$$\begin{aligned} W_F &= W_J + A\frac{C}{2} + B\frac{D}{2}, && (2.10)\\ \text{with } C &= (F+1) - I(I+1) - J(J+1) && (2.11)\\ \text{and } D &= \frac{3/4C(C+1) - I(I+1)J(J+1)}{I(2I-1)J(2J-1)}, && (2.12) \end{aligned}$$

where A and B are the magnetic-dipole and electric-quadrupole hyperfine structure constants, defined by Eq. (2.4) and Eq. (2.8), respectively.

In order to determine which transitions between the energy levels in an atom or ion are possible, selection rules are applied. A state is called “even” or of even parity if the sum over the angular momenta of all valence electrons $\sum l_i$ is even and “odd” if the sum is odd. Electric-dipole (E1) transitions between fine-structure levels are only possible between states of opposite parity. The selection rules for E1 fine-structure transitions are

1. $\Delta L = \pm 1$,
2. $\Delta S = 0$,

3. $\Delta J = \pm 1$ or 0,
4. $J = 0 \rightarrow 0$ is forbidden.

The transition rules for E1 transitions between hyperfine levels are similar to the rules for fine-structure transitions. For the hyperfine structure, the electron spin $\vec{S}$ in the fine structure is replaced by the nuclear spin $\vec{I}$ in the hyperfine structure, the angular momentum quantum number $\vec{L}$ is replaced by the total angular momentum of the electrons $\vec{J}$, and $\vec{J}$ is replaced by the total angular momentum of the ion $\vec{F}$. The corresponding quantum number F can take the values $F = I + J, I + J - 1, \ldots, |I - J|$. All hyperfine transitions in the absence of a magnetic field follow the selection rules

1. $\Delta F = \pm 1$ or 0,
2. $F = 0 \rightarrow 0$ is forbidden,
3. a) for electric-dipole transitions the states must have opposite parity;
   b) for magnetic-dipole transitions the states must have the same parity.

The relative strengths within a hyperfine-structure multiplet can be obtained by comparing the dipole matrix elements of the transitions. Taking the Wigner–Eckart theorem into account and using the sum rule by Ornstein, Burger and Dorgelo, the relative strengths of the transitions between a ground state characterized by F_i and J_i and an excited state characterized by F_f and J_f can be calculated by [Degl2009]

$$S_{F_i \to F_f} = \frac{(2F_i + 1)(2F_f + 1)}{2I + 1} \left\{ \begin{array}{c} J_i \; J_f \; 1 \\ F_f \; F_i \; I \end{array} \right\}, \tag{2.13}$$

where the bracket denotes a 6-j symbol. For the ${}^3\mathrm{F}_2^e \rightarrow {}^3\mathrm{D}_1^o$ transition in La$^-$ the relative intensities were calculated using Eq. (2.13). The results coincide with the values tabulated in the paper by White and Eliason [Whit1933] and are given in Tab. 2.1.

In saturation, the excitation rate and de-excitation rate are equal. Thus, a steady state is reached in which all sub-states of the upper and lower state of a transition are equally populated. Generally the sum rule for relative intensities applies [Foot2005]: the sum of the intensities to, or from, a given level is proportional to its degeneracy. It also applies

Table 2.1: Relative transition strengths for the hyperfine transitions in La$^-$. Calculated with Eq. (2.13).

$F_{\mathrm{exc}} \downarrow \| F_{\mathrm{gnd}} \rightarrow$	11/2	9/2	7/2	5/2	3/2
9/2	3/10	7/72	7/360		
7/2		11/72	8/63	3/56	
5/2			3/56	27/280	1/10

Table 2.2: Multiplicities and relative transition strengths in saturation for the hyperfine-structure transitions of the $^3\mathrm{F}_2 \rightarrow {}^3\mathrm{D}_1$ transition in La$^-$.

	F_{gnd}	11/2	9/2	7/2	5/2	3/2
F_{exc}	multiplicity	12	10	8	6	4
9/2	10	12/12	10/12	8/12		
7/2	8		10/12	8/12	6/12	
5/2	6			8/12	6/12	4/12

when both upper and lower configurations have hyperfine structure. In that case, the intensity of a given component of the line is proportional to the number of contributing m_F sub-states. According to this rule, the relative transition line strengths change compared to the unsaturated line strengths.

For the $^3\mathrm{F}_2^e \rightarrow {}^3\mathrm{D}_1^o$ transition in La$^-$ the degeneracies of the states are $2F_{\mathrm{gnd}} + 1$ and $2F_{\mathrm{exc}}+1$, respectively. The relative transition strengths in saturation are given in Tab. 2.2.

2.2 Zeeman and Paschen–Back effect

In an external magnetic field the electrons and the nucleus interact with the magnetic field. This leads to an additional splitting for all hyperfine levels with $F \neq 0$. In a weak external magnetic field, where the hyperfine splitting is much larger than the level splitting due to the magnetic field, the magnetic moments of the electron and the nucleus are firmly coupled. The total angular momentum $\vec{F}$ orients itself relative to the external field $\vec{H}$. The component of $\vec{F}$ in the field direction is $m_F = F, F-1, \ldots, -F$. The interaction energy of the ion is given by [Kopf1965]

$$\Delta W_{\mathrm{Zeeman}} = -\mu_F H \cos(\vec{\mu}_F, \vec{H}) = \mu_B g_F m_F H, \tag{2.14}$$

where $\vec{\mu}_F = \mu_J \cos(\vec{J}, \vec{F}) - \mu_I \cos(\vec{I}, \vec{F}) = \mu_B J g_J \cos(\vec{J}, \vec{F}) - \mu_K I g_I \cos(\vec{I}, \vec{F})$ is the total magnetic moment of the ion and the Landé g-factor of the ion is given by

$$g_F = g_J \frac{F(F+1) + J(J+1) - I(I+1)}{2F(F+1)} - g_I \frac{m_e}{m_p} \frac{F(F+1) + I(I+1) - J(J+1)}{2F(F+1)}. \tag{2.15}$$

The second contribution is a factor $m_e/m_p \approx 10^{-3}$ smaller than the first contribution and can therefore often be neglected. The Zeeman regime, where pure Zeeman splitting can be observed, is restricted to external magnetic field strengths $H \ll \frac{\mu_I}{\mu_B}\langle H(0)\rangle$.In the Zeeman regime, every hyperfine-structure multiplet splits up into $(2J+1) \times (2I+1)$ sub-levels according to m_F.

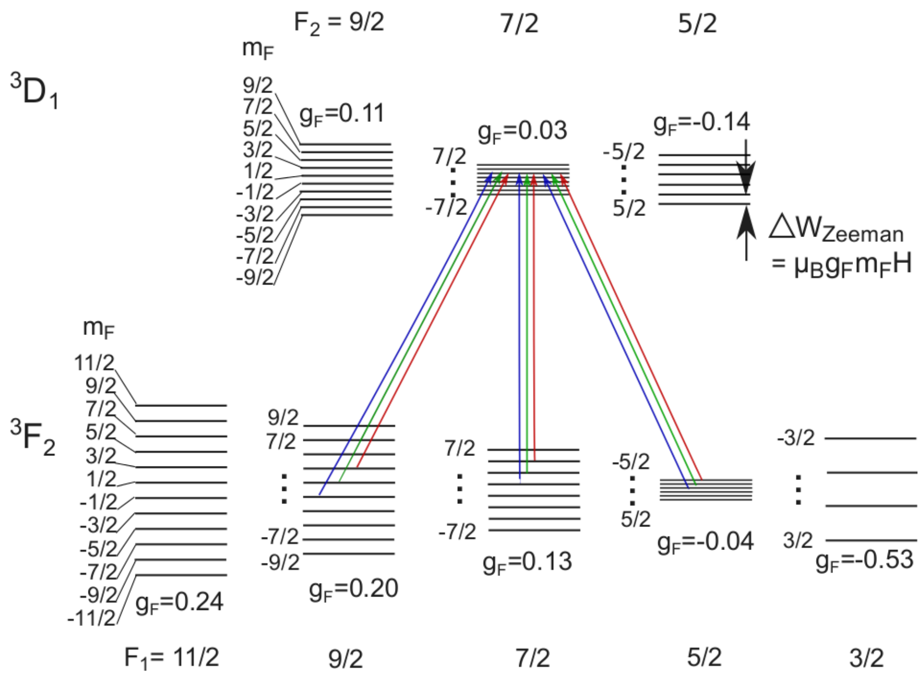

Figure 2.1: Level diagram with Zeeman splitting for the $^3\mathrm{F}_2^e \rightarrow\ ^3\mathrm{D}_1^o$ transition in La$^-$, (fine structure not to scale). Nine of the 192 possible transitions are indicated by arrows. The green lines indicate the π-transitions, the red and blue lines the σ^- and σ^+ transitions, respectively.

For example, in La$^-$ the $^3\mathrm{F}_2^e$ ground state splits up into 40 Zeeman sub-levels, the $^3\mathrm{D}_1^o$ excited state splits up into 24 sub-levels, as shown in Fig. 2.1. The transition splits 192-fold. In the earth's magnetic field the lines are spread over a frequency region of up to 1.4 MHz, as shown in Fig. 2.2.

In a strong external magnetic field, where $\Delta W_{\mathrm{HFS}} \ll -g_F\, m_F\, \mu_B\, H$, $\vec{J}$ and $\vec{I}$ are decoupled and the magnetic moments of the electrons and the nucleus are independently in precession about the magnetic field direction. They precess with the Larmor frequencies $\omega_{\mathrm{L}J} = eg_J H/(4\pi m_e)$ and $\omega_{\mathrm{L}I} = -eg_I H/(4\pi m_p)$, respectively. The magnetic energy in a strong magnetic field has three contributions, one from the magnetic moment of the electrons, a second one from the magnetic moment of the nucleus and a third one from the interaction between $\vec{I}$ and $\vec{J}$. It is given by [Kopf1965]

$$\Delta W_{\mathrm{PB}} = \mu_B H m_J g_J - \mu_K H m_I g_I + A m_I m_J. \tag{2.16}$$

This relationship holds for external magnetic fields H, for which $H \gg \frac{\mu_I}{\mu_B}\langle H(0)\rangle$. Here as well, the term containing $\mu_K \approx 10^{-3}\mu_B$ can be neglected in most cases.

For example, for the $^2S_{1/2}$ state in neutral Cs a pure Paschen–Back effect can be observed from a few T on; the level splitting is of the order of 30 GHz. In this case the external field is still much weaker than $\langle H(0)\rangle$. An intuitive explanation for the observation that

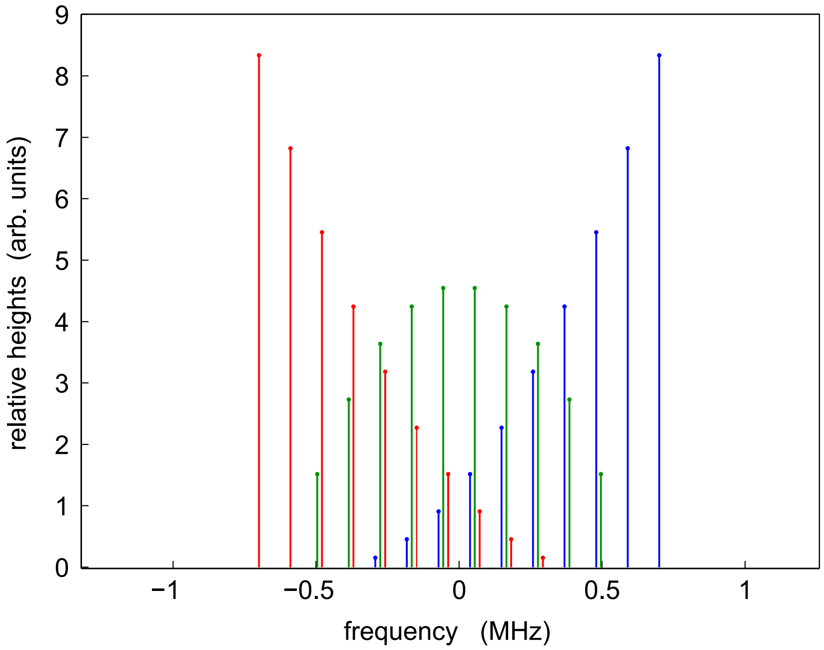

Figure 2.2: Calculated Zeeman spectrum for the transition between the $F = 11/2$ ground state and the $F = 9/2$ excited state in the earth's magnetic field of 60 μT. The π-transitions are indicated by the green lines the σ^+ and σ^--transitions by the blue and red lines, respectively. The transition lines are spread over a frequency range of about 1.4 MHz. The sum of the relative peak heights is normalized to 100.

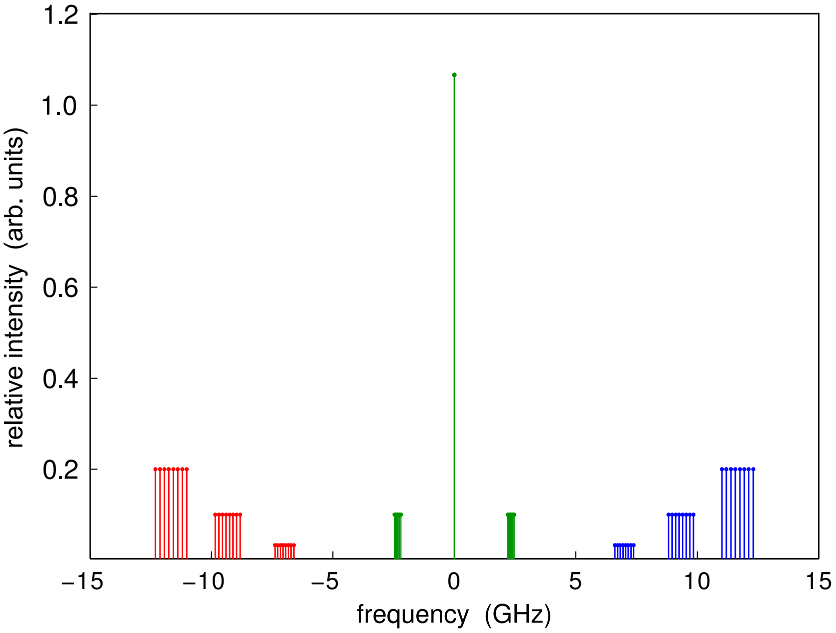

Figure 2.3: Calculated splitting at a magnetic field of 1 T for the $^3\mathrm{F}_2^e \rightarrow {}^3\mathrm{D}_1^o$ transition in La$^-$. The green lines indicate π-transitions, the blue and red lines σ^+- and σ^--transitions, respectively. The central π-transition is the superposition of 8 transitions originating from the energy levels with $m_J = 0$, which do not split.

the nucleus still orients itself in the external field is that the electrons precess too fast for the nucleus to follow.

The splitting in the Paschen–Back regime can be understood as a Zeeman splitting of the fine structure into $2J + 1$ sub-levels and a successive hyperfine Zeeman splitting into $2I + 1$ sub-levels. In total there are $(2J + 1) \times (2I + 1)$ sub-levels, the same number as for the Zeeman effect. In contrast to the Zeeman splitting, they are shifted up and down symmetrically to the center of gravity of the unperturbed hyperfine spectrum. In transverse observation, the frequencies of the π-transitions are in the middle, the σ-transitions are towards lower and higher frequencies. The splitting in the Paschen–Back regime for La$^-$ is shown in Fig. 2.3

In strong external magnetic fields the quadrupole interaction cannot be neglected. It contributes an additional term [Kopf1965]

$$\Delta W_Q^H = B/4 \frac{3m_J^2 - J(J+1)}{J(2J-1)} \frac{3m_I^2 - I(I+1)}{I(2I-1)} \quad . \tag{2.17}$$

The selection rules in the Zeeman regime are $\Delta m_F = 0$ for the π-components and $\Delta m_F = \pm 1$ for the σ-components. The relative line strengths for the transitions between the

Zeeman sub-levels are given by [Degl2009]

$$S_{\Delta m_F}(m_{Fi}, m_{Ff}) = 3 \begin{pmatrix} F_i & F_f & 1 \\ -m_{Fi} & m_{Ff} & \Delta m_F \end{pmatrix}^2 , \tag{2.18}$$

where $\Delta m_F = m_{Fi} - m_{Ff}$ and the bracket is a 3j-symbol. The factor 3 has been introduced such that the strengths are normalized to 1 for each pair of F_i and F_f.

In the Paschen–Back regime the selection rules are $\Delta m_I = 0$ and $\Delta m_J = 0$ for the π-components and $\Delta m_J = \pm 1$ for the σ-components. In addition, the condition $m_I = 0$ reduces the number of transitions compared to the Zeeman regime. With increasing magnetic field the forbidden $F = 0 \to 0$ transitions can become strong. The relative transition strengths also change. In the Paschen–Back regime the strengths of many remaining transitions are equal. The relative line strengths for the transitions between the sub-levels are given by [Degl2009]

$$S_{\Delta m_J}(m_{Ji}, m_I, m_{Jf}) = 3 \begin{pmatrix} J_i & J_f & 1 \\ -m_{Ji} & m_{Jf} & \Delta m_J \end{pmatrix}^2 , \tag{2.19}$$

where $\Delta m_J = m_{Ji} - m_{Jf}$, the bracket is the 3j-symbol. The sum of the strengths of the lines with the same Δm_J is 1.

2.3 Photon–atom interaction and rate equations

Multi-photon processes are of special interest because atoms or ions can be excited to energy states which are too high to be reached with a single photon from a commercial laser. Even forbidden transitions to states of the same parity can be excited. Further interesting phenomena can be observed for negative ions, such as excess photon absorption and threshold shifts in external radiation fields. For negative ions, multi-photon interactions most often result in a neutral core and an unbound electron.

The electric fields of two lasers with frequencies ω_1 and ω_2 can be described by

$$\vec{E}(t) = \vec{E}_1 \cos \omega_1 t + \vec{E}_2 \cos \omega_2 t, \tag{2.20}$$

where $\vec{E}_1 = E_1 \hat{e}_1$ and $\vec{E}_2 = E_2 \hat{e}_2$ are the fields with amplitudes E_1 and E_2 and polarization directions $\hat{e}_1$ and $\hat{e}_2$, respectively. The two-photon transition from state $|i\rangle$ to $|f\rangle$ with the same parity can be described with a (virtual) intermediate state with opposite parity $|a\rangle$, as shown in Fig. 2.4. The first absorbed photon brings the system from $|i\rangle$ to $|a\rangle$ and the second photon brings the system from $|a\rangle$ to $|f\rangle$. The interaction Hamiltonian of the radiation with the electrons for the two-photon process takes the form $\hat{H} = \vec{E}(t) \times \vec{D} = 1/2[\vec{E}_1 \vec{D}(e^{i\omega_1 t} + e^{-i\omega_1 t}) + \vec{E}_2 \vec{D}(e^{i\omega_2 t} + e^{-i\omega_2 t})]$, where $\vec{D}$ is the electric-dipole moment of the ion [Bass1977]. The counter-rotating terms can usually be neglected (rotating-wave

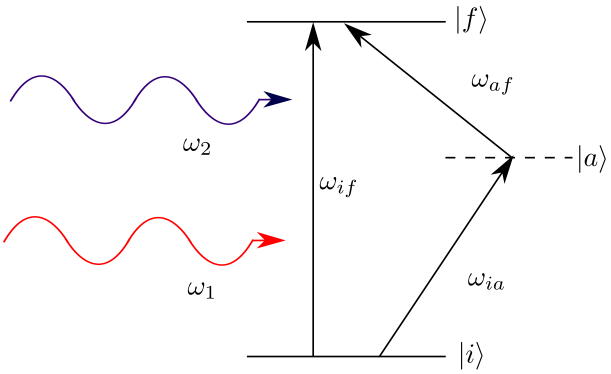

Figure 2.4: Two-photon excitation with two lasers with frequencies ω_1 and ω_2. The intermediate state(s) $|a\rangle$ can be real or virtual. The two-photon transition has the resonance frequency ω_{if}, the first step excitation $|i\rangle \to |a\rangle$ has the resonance frequency ω_{ia}, while the second step $|a\rangle \to |f\rangle$ has the resonance frequency ω_{af}.

approximation). The matrix elements for the first process have the form $\langle a|\hat{H}|i\rangle$. The first-order solution $S^{(1)}$ for the transition amplitude is [Kett2006]

$$\begin{aligned} S_a^{(1)} &= \frac{1}{2i\hbar}\int_0^t dt' \left[\langle a|\vec{E}_1\vec{D}|i\rangle e^{-i(\omega_1-\omega_{ia})t'} + \langle a|\vec{E}_2\vec{D}|i\rangle e^{-i(\omega_2-\omega_{ia})t'}\right] \\ &= \frac{1}{2\hbar}\left[\frac{\langle a|\vec{E}_1\vec{D}|i\rangle(e^{-i(\omega_1-\omega_{ia})t}-1)}{\omega_1-\omega_{ia}} + \frac{\langle a|\vec{E}_2\vec{D}|i\rangle(e^{-i(\omega_2-\omega_{ia})t}-1)}{\omega_2-\omega_{ia}}\right], \end{aligned} \tag{2.21}$$

where $\hbar\omega_{ia}$ is the energy difference between $|a\rangle$ and $|i\rangle$. The second order solution $S^{(2)}$ for the transition amplitude from $|i\rangle$ to $|f\rangle$ via (virtual) intermediate states $|a\rangle$, is found from

$$i\hbar\dot{S}_f^{(2)} = \sum_a \langle f|H|a\rangle e^{i\omega_{af}t} S_a^{(1)}, \tag{2.22}$$

with $\langle f|H|a\rangle = \frac{\langle f|\vec{E}_1\vec{D}|a\rangle}{2}e^{-i\omega_1 t} + \frac{\langle f|\vec{E}_2\vec{D}|a\rangle}{2}e^{-i\omega_2 t}$.

The second order solution $S^{(2)}$ for the transition amplitude is

$$S_f^{(2)} = \frac{1}{i\hbar}\int_0^t dt' \langle f|H|a\rangle e^{-i\omega_{fa}t'} S_a^{(1)}(t') \tag{2.23}$$

$$\begin{aligned} &= \frac{1}{4\hbar^2}\sum_a \left[\frac{\langle f|\vec{E}_1\vec{D}|a\rangle\langle a|\vec{E}_1\vec{D}|i\rangle}{\omega_1 - \omega_{ia}} \frac{e^{i(\omega_{if}-2\omega_1)t} - 1}{\omega_{if} - 2\omega_1} \right. \\ &+ \frac{\langle f|\vec{E}_2\vec{D}|a\rangle\langle a|\vec{E}_2\vec{D}|i\rangle}{\omega_2 - \omega_{ia}} \frac{e^{i(\omega_{if}-2\omega_2)t} - 1}{\omega_{if} - 2\omega_2} \\ &+ \frac{\langle f|\vec{E}_2\vec{D}|a\rangle\langle a|\vec{E}_1\vec{D}|i\rangle}{\omega_1 - \omega_{ia}} \frac{e^{i(\omega_{if}-(\omega_1+\omega_2))t} - 1}{\omega_{if} - (\omega_1+\omega_2)} \\ &+ \left. \frac{\langle f|\vec{E}_1\vec{D}|a\rangle\langle a|\vec{E}_2\vec{D}|i\rangle}{\omega_2 - \omega_{ia}} \frac{e^{i(\omega_{if}-(\omega_1+\omega_2))t} - 1}{\omega_{if} - (\omega_1+\omega_2)} \right]. \end{aligned} \tag{2.24}$$

The first two terms in Eq. (2.24) are due to the absorption of two photons from the same beam, while the third and fourth term describe the absorption of one photon from each of the two beams. If two different lasers are used with frequencies far from resonance, the first terms can be neglected.

In the case of La$^-$, there is an intermediate state leading to a two-step transition. There is one relatively long-lived intermediate state, and the upper "state" is unbound. The excitation can be approximated with a two-step process. All four processes in Eq. (2.24) can occur, but the probability of two-photon processes, in which the ions absorb two photons simultaneously is very low, with cross sections of the order of 10^{-50} cm^{4}s [Stap1991]. This is much lower than the probability for a resonant two-step excitation, where the ion is first resonantly excited to the intermediate state and then to the final state. Generally, in the case of one intermediate state $|k\rangle$ the transition amplitude can be approximated with [Kett2006]

$$S_f \approx \frac{1}{4\hbar^2} \frac{\langle f|\vec{E}_2\vec{D}|k\rangle\langle k|\vec{E}_1\vec{D}|i\rangle}{\omega_1 - \omega_{ik}} \frac{e^{i(\omega_{if}-(\omega_1+\omega_2))t} - 1}{\omega_{if} - (\omega_1+\omega_2)} \tag{2.25}$$

and the transition probability is

$$W_{i\to f} = \frac{1}{16\hbar^4} \frac{|\langle f|\vec{E}_2\vec{D}|k\rangle|^2 |\langle k|\vec{E}_1\vec{D}|i\rangle|^2}{(\omega_1 - \omega_{ik})^2} \frac{\sin^2(\omega_{if} - (\omega_1+\omega_2))t/2}{[(\omega_{if} - \omega_1 - \omega_2)/2]^2}. \tag{2.26}$$

The transition rate is obtained by integrating over the spectral range. For practical purposes, the transition rate is given in terms of the radiation intensity I which is related to the electric-field amplitude by the relation

$$E^2 = 8\pi I/c. \tag{2.27}$$

The transition rate then becomes

$$R_{if} = \frac{8\pi^3}{\hbar^4 c^2} \frac{|D_{ik}|^2 |D_{fk}|^2}{\delta\omega^2} f(\omega_{if}) I_1 I_2, \tag{2.28}$$

where $\delta\omega = \omega_1 - \omega_{ik}$ is the detuning, $f(\omega)$ the line shape function and D_{ik} a dipole matrix element defined by the relation $|\langle k|\vec{E}_1\vec{D}|i\rangle|^2 = 8\pi|D_{ik}|^2 I_1/c$.

The dipole matrix elements can be related to the coefficients in Einstein's theory of black-body radiation. In this empirical theory the transition from state $|1\rangle \to |2\rangle$ is described by a transition rate $R_{12} = B_{12}\rho(\omega_1 2)$, where $\rho(\omega)$ is the spectral energy density and B_{12} is the Einstein coefficient for the absorption. From comparison with the absorption coefficient one obtains the expression [Loud1973]

$$B_{12} = \frac{\pi|D_{12}|^2}{3\epsilon_0\hbar^2}.$$

The Einstein coefficient which describes the spontaneous decay of the states is A_{21}. It is related to B_{12} via the relation

$$A_{21} = \frac{g_1}{g_2} \frac{\hbar\omega^3}{\pi^2 c^3},$$

where g_1 and g_2 are the degeneracies of the lower and the upper state, respectively. The coefficient A_{21} in terms of the elastic scattering cross section $\sigma(\omega)$ is

$$A_{21} = \frac{g_1}{g_2} \frac{\omega}{\pi^2 c^2 f(\omega)} \sigma(\omega). \tag{2.29}$$

At the exact resonance frequency ω_0, a Lorentzian line shape function [Eq. (2.42)] becomes $f_L(\omega_0) = (\gamma/2)^{-1}$, where γ is the FWHM of the Lorentzian. The expression for A_{21} becomes

$$A_{21} = \frac{g_1}{g_2} \frac{2\pi\gamma}{\lambda^2} \sigma(\omega_0) = \frac{g_1}{g_2} \frac{4\pi^2 \Gamma \nu_0^2}{c^2} \sigma(\nu_0), \tag{2.30}$$

where Γ is the FWHM of the Lorentzian in units of Hz.

The two-step process in La$^-$ can be treated with Einstein's rate equations. The rate equations can be applied either if the bandwidth of the incident light exceeds the atomic transition linewidth or if the broadened linewidth greatly exceeds the natural linewidth of the transition. The latter condition is fulfilled for the ions used in this work. La$^-$ is detached in a two-step process, as shown in Fig. 2.5. It is first excited from the ground state with population N_g to an excited state with population N_e. The excitation is resonant with the excitation laser with photon flux Φ_e. The successive detachment of La$^-$ to the detached "state" with population N_d is non-resonant and requires a higher photon

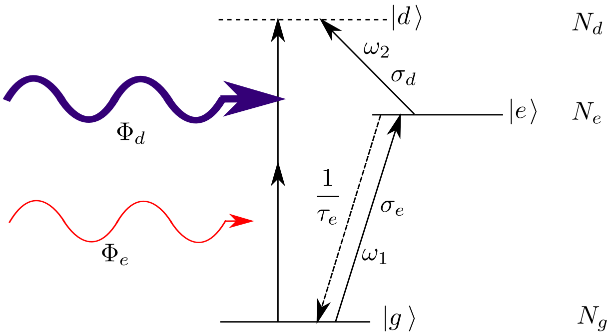

Figure 2.5: Two-photon detachment of La$^-$ with two lasers. The first laser with photon flux Φ_e is in resonance with the first transition. The second laser has a different wavelength and photon flux Φ_d. The ions are first resonantly excited to an intermediate state $|e\rangle$ and successively detached by absorption of a second photon. The lifetime of the excited state is τ_e. The populations of the states are N_g, N_e, and N_d.

flux Φ_d at a different frequency. The rate equations for the two-step absorption process are given by

$$\begin{aligned}
\frac{dN_g}{dt} &= -\sigma_e\Phi_e N_g(t) + (\sigma_e\Phi_e + \tau_e^{-1})N_e(t) && (2.31)\\
\frac{dN_e}{dt} &= \sigma_e\Phi_e N_g(t) - (\sigma_e\Phi_e + \sigma_d\Phi_e + \sigma_d\Phi_d + \tau_e^{-1} + \tau_{loss}^{-1})N_e(t) && (2.32)\\
\frac{dN_d}{dt} &= \sigma_d(\Phi_e + \Phi_d)N_e(t). && (2.33)
\end{aligned}$$

In order to derive an analytical solution to the rate equations, the following approximation is made. The interaction time of the ions with the laser at 10 keV beam energy is $t_{\text{interact}} =$ 6.4 µs, whereas the lifetime of the excited state is expected to be τ_e= 34.5 µs. In order to obtain analytically solvable equations spontaneous emission is neglected, as well as losses of ions to different states outside of this three-level system. The detachment by the excitation laser ($\sigma_d\Phi_e$) is measured separately and subtracted, thus it is not taken into account here. With this simplification the solution for the rate equations can be calculated. The analytical solutions calculated with MATHEMATICA are

$$N_g(t) = \exp\left[-(1/2)t(2\sigma_e\Phi_e + \sigma_d\Phi_d)\right]n\left[\cosh\left(\frac{1}{2}t\sqrt{4\sigma_e^2\Phi_e^2 + \sigma_d^2\Phi_d^2}\right) + \frac{\sigma_d\Phi_d\sinh\left(\frac{1}{2}t\sqrt{4\sigma_e^2\Phi_e^2 + \sigma_d^2\Phi_d^2}\right)}{\sqrt{4\sigma_e^2\Phi_e^2 + \sigma_d^2\Phi_d^2}}\right], \tag{2.34}$$

$$N_e(t) = \frac{2\exp\left(-\frac{1}{2}t(2\sigma_e\Phi_e + \sigma_d\Phi_d)\right)n\sigma_e\Phi_e\sinh\left[\frac{1}{2}t\sqrt{4\sigma_e^2\Phi_e^2 + \sigma_d^2\Phi_d^2}\right]}{\sqrt{4\sigma_e^2\Phi_e^2 + \sigma_d^2\Phi_d^2}}, \tag{2.35}$$

$$\begin{aligned}
N_d(t) = {} & \frac{1}{2\sqrt{4\sigma_e^2\Phi_e^2+\sigma_d^2\Phi_d^2}} \exp\left(-\frac{1}{2}t\left[2\sigma_e\Phi_e+\sigma_d\Phi_d+\sqrt{4\sigma_e^2\Phi_e^2+\sigma_d^2\Phi_d^2}\right]\right) n \qquad (2.36)\\
& \times \Bigg[(2\sigma_e\Phi_e+\sigma_d\Phi_d)\left[1-\exp\left(t\sqrt{4\sigma_e^2\Phi_e^2+\sigma_d^2\Phi_d^2}\right]\right) \\
& - \left[1+\exp\left(t\sqrt{4\sigma_e^2\Phi_e^2+\sigma_d^2\Phi_d^2}\right)-2\exp\left(\frac{1}{2}t\left[2\sigma_e\Phi_e+\sigma_d\Phi_d+\sqrt{4\sigma_e^2\Phi_e^2+\sigma_d^2\Phi_d^2}\right]\right)\right] \\
& \times \sqrt{4\sigma_e^2\Phi_e^2+\sigma_d^2\Phi_d^2}\,\Bigg].
\end{aligned}$$

2.4 Line broadening and narrowing effects

For spectroscopic measurements it is important to understand the origin of the observed peak width and shape. Usually the natural line width $\gamma = 1/\tau$ cannot be observed directly, because various effects broaden the observed transition width. In the following the most important broadening effects relevant for this work are described.

2.4.1 Doppler broadening

In thermal equilibrium, the ions in a gas have a velocity spread that follows a Maxwellian distribution. This leads to an associated distribution in the absorption frequencies via the Doppler effect. The laser frequency ω in the rest frame of the ions moving with velocity $\vec{v}$ appears shifted as [Demt1981b]

$$\omega' = \omega - \vec{k}\vec{v} + \omega_0\frac{v^2}{2c^2} + \dots\ . \qquad (2.37)$$

Here only the first-order Doppler effect is taken into account. The third term, the second-order Doppler effect, is neglected. If the laser propagates in z-direction the resonance frequency for absorption $\omega = \omega_a$ becomes

$$\omega_a \approx \omega_0(1+v/c). \qquad (2.38)$$

The relative probability that an ion has a velocity component between v_z and $v_z + dv_z$ corresponds to the probability that it absorbs a photon in the frequency range between ω and $\omega + \delta\omega$. The relative probability is given by [Loud1973]

$$\exp\left(\frac{-mv_z^2}{2k_BT}\right)dv_z = \frac{c}{\omega_0}\exp\left(\frac{-mc^2(\omega_0-\omega)^2)}{2\omega_0^2k_BT}\right)d\omega, \qquad (2.39)$$

where T is the temperature of the ion gas. This leads to a Gaussian distribution of the absorbed frequencies with a maximum of absorption at $\omega = \omega_0$. The full width at half maximum (FWHM) is the so-called Doppler width

$$\Delta\omega_D = \omega_0 \sqrt{\frac{8k_B T \ln 2}{mc^2}}. \tag{2.40}$$

The normalized Gaussian lineshape function is given by

$$f_G(\omega) = \frac{1}{\sqrt{2\pi\Delta^2}} \exp\left(-\frac{(\omega_0 - \omega)^2}{2\Delta^2}\right), \tag{2.41}$$

where $\Delta = \omega_0\sqrt{k_B T/mc^2} = \Delta\omega_D/(2\sqrt{2\ln 2})$ and Δ^2 is the variance of the Gaussian frequency distribution.

Doppler broadening is an inhomogeneous broadening mechanism because different ions absorb different frequencies, depending on their velocity. It is often combined with some homogeneous broadening mechanism, such as power broadening, where each absorbing or emitting particle is effected in the same way. Homogeneous broadening effects generally lead to a Lorentzian lineshape, given by

$$f_L(\omega) = \frac{\gamma/2\pi}{(\omega_0 - \omega)^2 + (\gamma/2)^2}, \tag{2.42}$$

where γ is the FWHM of the Lorentzian distribution. In this case the convolution of the two line shapes, a Voigt profile, is observed and the spectral intensity distribution becomes [Loud1973]

$$f(\omega) = \int_{-\infty}^{\infty} d\nu F_L(\nu) F_G(\omega + \omega_0 - \nu) = \frac{\gamma}{(2\pi)^{3/2}\Delta} \int_{-\infty}^{\infty} d\nu \frac{\exp\left[-(\nu-\omega)^2/(2\Delta)^2\right]}{(\omega_0 - \nu)^2 + (\gamma/2)^2}, \tag{2.43}$$

where ω_0 is the common central frequency of the two distributions. F_L and F_G can be interchanged. There is no simple analytic expression for the linewidth in this case [Loud1973]. For $\Delta \to 0$ it reduces to the Lorentzian lineshape [Eq. (2.42)], for $\gamma \to 0$ it reduces to the Gaussian lineshape [Eq. (2.41)].

2.4.2 Power broadening

In a broadband laser field the absorption profile for a homogeneously broadened transition $|1\rangle \to |2\rangle$ of a closed two-level system $\alpha(\omega) = \sigma_{12}(N_1 - N_2) = \sigma_{12}\Delta N$, with population densities N_1 and N_2 of the ground and of the excited state, respectively, and the population difference ΔN. If the line is homogeneously broadened it has a Lorentzian shape and the absorption profile at low intensity is given by [Demt1981a]

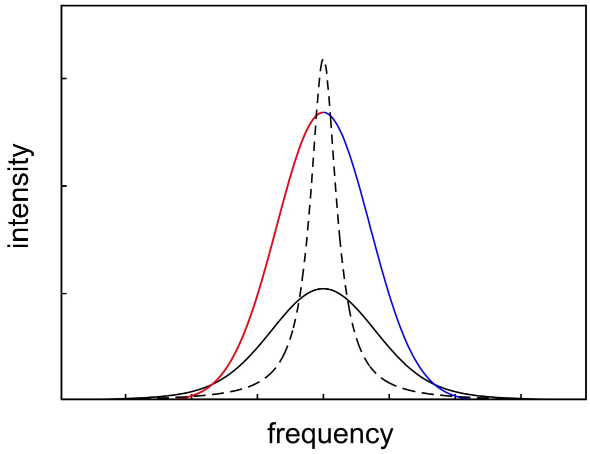

Figure 2.6: The convolution of a Gaussian and a Lorentzain lineshape results in a Voigt profile, as indicated by the solid black line. The Gaussian profile is indicated by the red and blue line, corresponding to the red- and blueshifted absorption frequencies of the Doppler broadened line. The Lorentzian is indicated by the dashed black curve.

$$\alpha(\omega) = \frac{2\hbar\omega B_{12}\Delta N_0}{c\pi\gamma}\frac{(\gamma/2)^2}{(\omega-\omega_0)+(\gamma/2)^2} = \frac{\alpha_0(\omega_0)(\gamma/2)^2}{(\omega-\omega_0)+(\gamma/2)^2}, \tag{2.44}$$

where $\alpha_0(\omega_0)$ is the linear resonant absorption coefficient and ΔN_0 is the population difference in thermal equilibrium without a radiation field. As the laser intensity is increased, the excitation rate so does and, at sufficiently strong laser intensity, it exceeds the relaxation rate R, the spontaneous emission for a closed two-level system. As a result, the population of the absorbing level decreases. The population difference in saturation is given by

$$\Delta N = \frac{\Delta N_0}{1+S}, \tag{2.45}$$

where S is called saturation parameter. It is the ratio between absorption and spontaneous emission:

$$S = \frac{2P}{R_1+R_2} = \frac{\rho(\omega)B_{12}}{A_{21}} = \frac{2\sigma_{12}I(\omega)}{\hbar\omega A_{21}} = \frac{I(\omega)}{I_{\text{sat}}}, \tag{2.46}$$

where $\rho(\omega)$ is the radiation density and $P = \rho(\omega)B_{12} = \sigma_{12}I(\omega/\hbar\omega)$ is the absorption probability for a monochromatic wave with intensity $I(\omega)$ and $I_{\text{sat}} = \hbar\omega A_{21}/(2\sigma_{12})$ is the saturation intensity. The absorption coefficient $\alpha(\omega)$ of a homogeneously broadened line is Lorentzian, the induced absorption probability follows a Lorentzian line profile. Therefore, a frequency-dependent spectral saturation parameter $S(\omega)$ can be defined as

$$S(\omega) = S_0 \frac{(\gamma/2)^2}{(\omega-\omega_0)^2 + (\gamma/2)^2}, \qquad \text{with} \qquad S_0 = S(\omega_0). \tag{2.47}$$

With these definitions the frequency dependence of the absorbed power W_{abs} is

$$\frac{d}{dt} W_{\text{abs}}(\omega) = \hbar\omega B_{12}\rho(\omega)\Delta N = \frac{\hbar\omega R \Delta N_0 S_0 (\gamma/2)^2}{(\omega-\omega_0)^2 + (\gamma/2)^2(1+S_0)} = \frac{C}{(\omega-\omega_0)^2 + (\gamma_S/2)^2}, \tag{2.48}$$

$$\text{where} \qquad \gamma_S = \gamma\sqrt{1+S_0}. \tag{2.49}$$

This is a Lorentzian absorption profile with increased width γ_S. The saturated absorption coefficient $\alpha_s(\omega)$ is given by

$$\alpha(\omega) = \frac{\alpha_0(\omega)}{1+S(\omega)} = \frac{\alpha_0(\omega_0)(\gamma/2)^2}{(\omega-\omega_0)^2 + (\gamma_S/2)^2}. \tag{2.50}$$

Saturation decreases the absorption coefficient by a factor $1/[1+S(\omega)]$. The maximum decrease is S_0 for $\omega = \omega_0$. Far from resonance the decrease goes to zero.

Saturation of inhomogeneously broadened lines

In this work, a laser with a narrow bandwidth of $\nu_L \approx 1$ MHz was used, which is much narrower than the inhomogeneously broadened transition width of more than 50 MHz. Under these conditions, the laser "burns a hole" into the broad absorption profile of ions. This is because the laser with frequency ω_L is only absorbed by ions moving at a certain velocity $\vec{v}$, for which $\omega = \omega_L - \vec{k}\vec{v}$ (with $\vec{k}\vec{v} = kv_z$) falls into the homogeneous linewidth of the ion at rest $\omega_0 \pm \gamma/2$.

The transition cross section for an ion with velocity v_z parallel to the laser is [Demt1981b]

$$\sigma_{12}(\omega, v_z) = \sigma_0 \frac{(\gamma/2)^2}{(\omega-\omega_0-kv_z)^2 + (\gamma/2)^2}, \tag{2.51}$$

where σ_0 is the maximum absorption cross section at the line center of the transition. In saturation the population of the lower state N_1 is decreased on the velocity interval $dv_z = \gamma/k$, while the population of the upper level is increased. The population densities of the two states are

$$N_1(\omega, v_z) = N_1^0(v_z) - \frac{\Delta N^0}{\gamma_1 \tau}\left[\frac{S_0(\gamma/2)^2}{(\omega-\omega_0-kv_z)^2 + (\gamma_S/2)^2}\right] \tag{2.52}$$

and

$$N_2(\omega, v_z) = N_2^0(v_z) - \frac{\Delta N^0}{\gamma_2 \tau}\left[\frac{S_0(\gamma/2)^2}{(\omega - \omega_0 - kv_z)^2 + (\gamma_S/2)^2}\right], \tag{2.53}$$

where $\gamma = \gamma_1 + \gamma_2$ is the homogeneous width of the transition and $1/\tau = 1/\tau_1 + 1/\tau_2$ is the longitudinal relaxation time. The decrease and increase are only the same if the relaxation times of the lower and upper level are the same. The population difference depends on the velocity and is given by

$$\Delta N(\omega_S, v_z) = \Delta N^0(v_z)\left[1 - \frac{S_0(\gamma/2)^2}{(\omega - \omega_0 - kv_z)^2 + (\gamma_S/2)^2}\right]. \tag{2.54}$$

The so-called Bennet hole is the minimum in the absorption profile and has the homogeneous width given by Eq. (2.49) and a depth at the hole center

$$\Delta N^0(v_z) - \Delta N(v_z) = \Delta N^0(v_z)\frac{S_0}{1 + S_0}. \tag{2.55}$$

In saturation the absorption has a Voigt profile with the power-broadened width γ_S instead of γ. The unsaturated absorption coefficient for a Doppler-broadened line is [Demt1981a]

$$\alpha(\omega) = \Delta N_0 \frac{\sigma\gamma\sqrt{\pi}}{v_p \omega_0}, \tag{2.56}$$

and the saturated absorption coefficient of a Doppler-broadened line is

$$\alpha_S(\omega) = \frac{\alpha^0(\omega_0)}{\sqrt{1 + S_0}} \exp\left[-\left(\frac{\omega - \omega_0}{0.6\Delta\omega_D}\right)^2\right]. \tag{2.57}$$

With one laser a Voigt profile is visible, but the Bennet hole cannot be detected. With two lasers, where one laser is strong and “burns the hole” and the other is weak and probes the absorption profile, the Bennet hole can be detected. The observed absorption coefficient for the probe laser is an unsaturated Doppler profile with a saturation dip at the frequency $\omega' = \omega_0 \pm (\omega_1 - \omega_0)k_1/k_2$:

$$\alpha_S(\omega_1, \omega) = \alpha^0\left[1 - \frac{S_0}{\sqrt{1 + S_0}}\frac{(\gamma/2)^2}{(\omega - \omega')^2 + (\gamma_S/2)^2}\right]. \tag{2.58}$$

2.4.3 Velocity bunching and geometrical cooling

An advantage of collinear spectroscopy compared to a transverse setup is the effect of velocity bunching (also called acceleration cooling). The ions start from the source with a thermal velocity $v_{th} \approx \sqrt{2k_BT/m}$ and a velocity distribution Δv_{th}. After production,

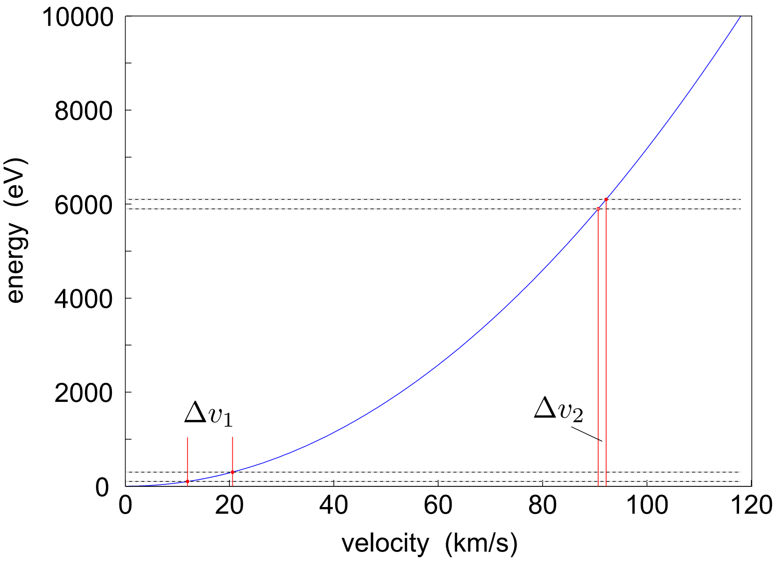

Figure 2.7: The acceleration of ions to high kinetic energy results in velocity bunching. The same energy spread (dashed black lines) leads to a larger velocity spread Δv_1 (red lines) at low kinetic energy than at higher kinetic energy Δv_2. This effect is called velocity bunching or kinematic cooling. Adapted from [Demt1981b].

the ions are accelerated to a much higher velocity $v_a \gg v_{th}$ by the extraction voltage U_{ext}. After acceleration, they have the kinetic energy

$$E_{\text{kin}} = \frac{1}{2}mv_{th}^2 + eU_{\text{ext}} = \frac{1}{2}mv^2, \tag{2.59}$$

where $v = \sqrt{(v_{th}^2 + v_a^2)} \approx v_a + v_{th}^2/(2v_a)$. Thus, the velocity spread is reduced in the direction of acceleration

$$\Delta v = \frac{v_{th}}{v_a}\Delta v_{th}. \tag{2.60}$$

This leads to a reduction in the Doppler width ω_D by a factor [Kauf1976]

$$R = \frac{1}{2}\sqrt{\frac{k_B T}{eU_{\text{ext}}}}. \tag{2.61}$$

In this experiment, the La$^-$ ions have a temperature of about 1600 K after production. The thermal velocity distribution leads to Doppler width of about 235 MHz. After acceleration with a potential of $U_{\text{ext}} = 10$ kV the line width is reduced by a factor $R \approx 540$ to 0.4 MHz.

Another narrowing effect is geometrical cooling; the basic principle is shown in Fig. 2.8. The collimation angle ϵ is defined by the collimation ratio between the velocities v_z in beam direction and v_x transversal to the beam direction

$$\frac{v_x}{v_z} = \tan\epsilon = \frac{b}{2d}. \tag{2.62}$$

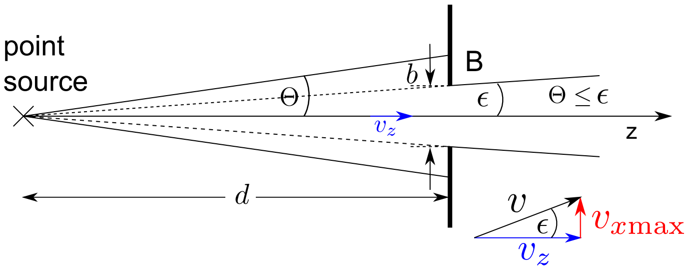

Figure 2.8: Geometrical cooling. If the deflection angle Θ is larger than the collimation angle ϵ, these ions can no longer pass the collimating aperture B. This causes a reduction of the transverse velocity component. Adapted from [Demt1981b].

Here d is the distance and b is the diameter of the aperture. Narrowing is achieved if ions at a larger deflection angle than the collimation angle ϵ can no longer pass an aperture. Ions with a transverse velocity v_x larger than a certain threshold $v_{x\max}$ are sorted out, and the transverse velocity distribution is reduced.

Chapter 3

Experimental setup

The spectroscopy experiments were performed in a collinear laser photodetachment spectroscopy setup at the Max Planck Institute for Nuclear Physics (MPIK). In this setup, shown in Fig. 3.1, anion beams produced with a Middleton-type sputter ion source are accelerated to kinetic energies $E_{\mathrm{beam}} = 4 - 10$ keV. The $^{139}\mathrm{La}^-$ ions are mass-separated from other elements and contaminant molecules, such as O^- or LaO^-, in a dipole magnet with a resolving power of $m/\Delta m = 180$. The negative ions are guided into the spectrometer section by a 90° electrostatic deflector [Krec2010] which has been modified with apertures to let the laser beam pass straight through. The spectroscopy section consists of an entrance diaphragm, a drift tube where laser excitation takes place and a second diaphragm. In resonance, part of the anions are neutralized by the interaction with the laser and neutral atoms are created. A deflector behind the second diaphragm deflects the remaining ions into a Faraday cup, whereas the neutral atoms are detected in forward direction. The components of the experiment are described in more detail in the following.

3.1 Middleton type ion sputtering source

The ion source is a Middleton-type multi-purpose ion sputter source. This is a common source for negative ion beams. The setup and function has been described in detail by Middleton [Midd1989], and the source used in this experiment has been described before in Ref. [Meie2007]. It is well known that lanthanides tend to deposit on the ionizing filament and lower the work function [MH1998]. This effect is known as 'poisoning'. Therefore, an ion beam of lanthanides is more difficult to produce compared to transition metals or non-metals. The improvement and operation of the La^- ion source was a major task of this work. The main parts for the beam generation are the target made of the element for the beam, a Cs reservoir and an ionizing filament, as shown in Fig. 3.2. The Cs (purity 99.5%) is heated until the gas fills the chamber of the source which contains the ionizer and the target. The Cs atoms are thermally ionized on the surface of the hot

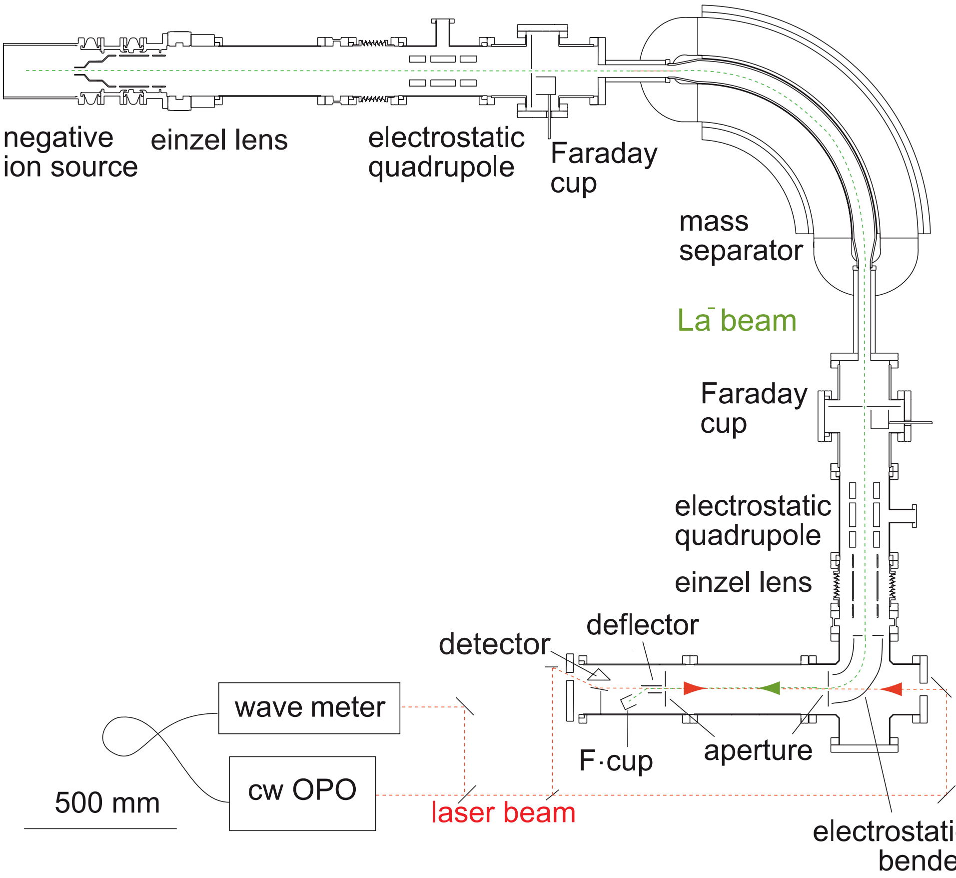

Figure 3.1: Overall sketch of the negative ion beamline in operation at MPIK. The ions (green dotted line) are created in the ion source and transferred to the spectroscopy section. The mass separator filters out contaminants. The einzel and quadrupole lenses refocus the beam.

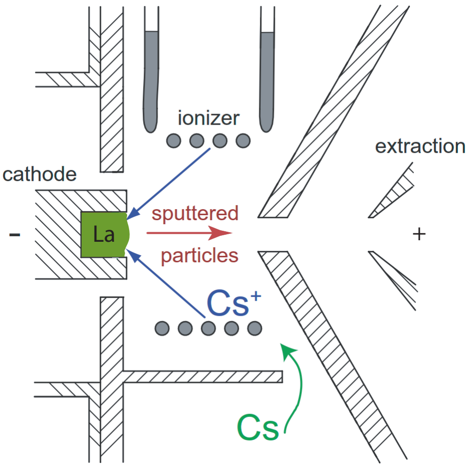

Figure 3.2: Schematic drawing of the Middleton-type multi-purpose sputter ion source. The Cs vapor diffuses into the source and is ionized on the ionizer coil. Cs^+ is sputtered onto the lanthanum target and the La^- ions are extracted from the source. Adapted from Ref. [Meie2007].

ionizer and Cs^+ ions are created. A voltage between the ionizer and the target sputters the Cs^+ ions onto the target. The target is water-cooled, such that a thin Cs layer condenses on the surface. When Cs^+ impinges on the surface with an energy of about 2 keV, La is sputtered out, creating La^- ions by charge exchange with the Cs surface layer or by collisions with excited Cs atoms in front of the target [Voge2013, Ande2013]. The extraction potential V_{ext} between the target and the grounded extraction electrode accelerates La^- ions out of the source. The extraction potential determines the beam energy, which was $E_{\text{beam}} = 4 \ldots 10$ keV in this experiment. Below 4 keV only few La^- ions (< 0.5 pA) reach the spectroscopy region and for voltages > 10 kV discharges occur in the source.

Usually tungsten ionizers are used. For La_2O_3 as target material, poisoning limits the operation time to about 4 h. A tungsten disk on the surface of the target with a small hole in the center protects the ionizer by narrowing the extraction angle for La^- [Heil2012]. However, the tungsten disk strongly reduces the output of La^- ions. A target of metallic lanthanum with an ionizer made of a material with higher work function, e.g. Pt or Ir, can extend the operation time considerably [Alto1996]. A comparison of the work functions of the metals in the source is shown in Tab. 3.1. An overview of work functions for the elements of the periodic table can be found in Ref. [Mich1977]. The platinum ionizer was difficult to handle because the material is very soft. It tends to stick to the support and is easily deformed when it is taken out for cleaning. A filament made of iridium was found to be the best choice. The work function of Ir is similar to that of Pt, but the material is harder and the melting point is higher, so it does not deform as easily and does not stick to the support. With a filament made of Ir, a La^- current of 0.5–10 pA was produced for up to 72 h. The evolution of the current is shown in Fig. 3.3.

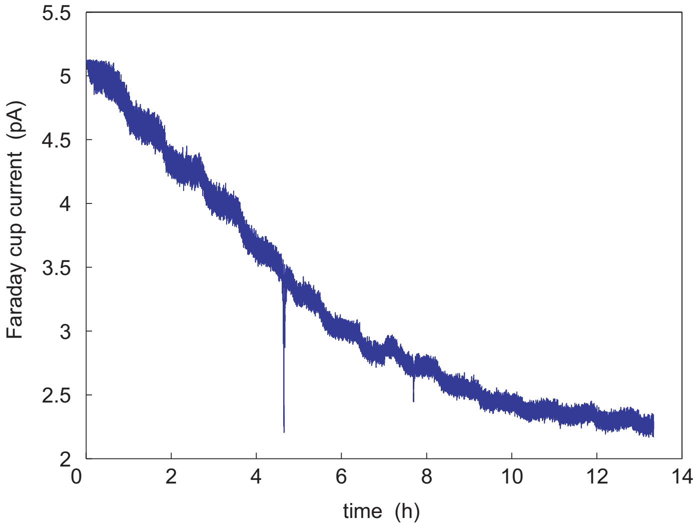

Figure 3.3: Ion beam current of the source. The current decreases with a time constant of $\sim$ 5.4 h due to poisoning of the ionizer. The decay slows down at a low current of about 6 pA. The oscillations of the current originate from temperature oscillations in the source due to non-constant cooling, the spikes are due to discharges inside the source or the second einzel lens.

While the current continues to decrease exponentially because of poisoning, after about 12 h of operation the source delivers a steady current of several pA for about 60 h. The source does not only produce lanthanum anions but also a range of other anions, such as O^-, OH^-, the components of the stainless steel from the target holder and the anions of lanthanum composites LaH^-, $LaH_2{}^-$, $LaH_3{}^-$, LaH_4^-, LaO^- and LaO_2^-. The concentration of the contaminants depends on the residual gas pressure, the position of the target, the oxide layer on the surface of the target and on the temperature of the source [Midd1989]. A mass spectrum recorded at 6 kV acceleration voltage is shown in Fig. 3.4. The content of contaminants in the ion beam typically changed during the measurement. After some time of sputtering the oxide layer on the surface of the target is reduced and the residual gas pressure decreases after the source reaches the final temperature.

When the ionizer is poisoned after the run, the La on the surface has to be removed. This is achieved by cleaning the ionizer in concentrated hydrochloric acid (min. 37% HCl). The container with the acid is placed in an ultrasonic bath for 10 min. After this treatment the ionizer is clean and performance is restored. Ir is inert to reaction with acids, so the ionizer can be cleaned without being damaged.

Table 3.1: Work functions of ionizer materials (polycrystalline) and the elements used in the source [Mich1977].

element	work function (eV)
Pt	5.65
Ir	5.27
W	4.55
La	3.5
Cs	2.14

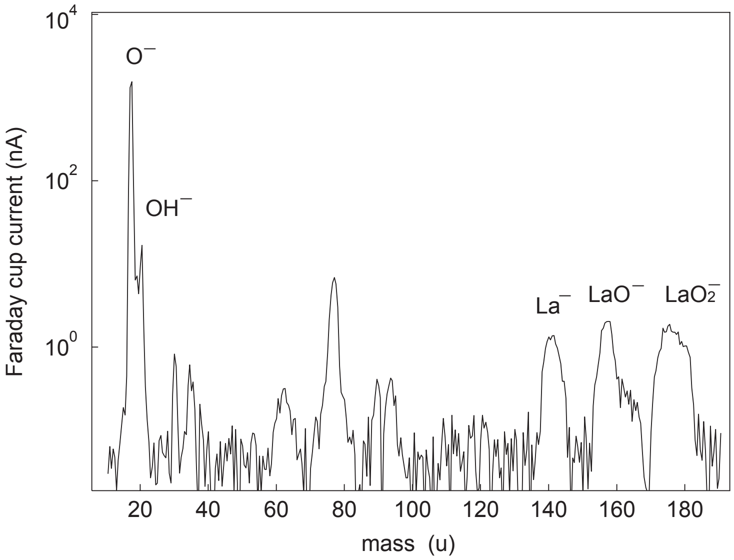

Figure 3.4: Typical mass spectrum of the ion source recorded at 6 keV beam energy. The magnetic field of the mass separator dipole magnet was slowly changed by increasing the current in the coils while the beam current was measured. The masses were determined by a fit to characteristic peaks, such as $^{16}O^-$ and $^{139}La^-$.

3.2 Laser system

The laser light used for the spectroscopy is produced by a continuous-wave optical parametric oscillator (OPO) (Argos Aculight Model 2400 with Module B). The OPO is pumped by a fiber amplifier (IPG), which is in turn seeded by a module fibre laser (Koheras Basik N81-130-21) with 1064 nm wavelength.

In the crystal of the OPO the pump beam is down-converted into two laser beams with lower photon energy. The frequencies for these two beams may be different. For historical reasons the beam with the higher photon energy is called "signal", while the one with lower photon energy is called "idler". Energy conservation dictates that

$$\frac{1}{\lambda_{\mathsf{pump}}} = \frac{1}{\lambda_{\mathsf{idler}}} + \frac{1}{\lambda_{\mathsf{signal}}}. \tag{3.1}$$

The idler output of the OPO was used for the spectroscopy, its tuning range is $2600 \ldots 3200$ nm, its bandwidth < 1 MHz and the power > 1 W over the entire wavelength range. The wavelength of the idler beam is determined by measuring the wavelengths of the signal and the pump beam with a wavemeter. The wavemeter (HighFinesse WS Ultimate 30 IR) is based on the Fizeau interferometer technique. According to the manufacturer, the absolute accuracy is 30 MHz in the range 370–1100 nm and 20 MHz between 1100–2250 nm. The wavemeter was regularly calibrated with a stabilized diode laser with wavelength 1532.83045 nm (HighFinesse SLR-1532). The signal and pump beam were attenuated and fed into a multi-fiber switch. The signal, pump and reference wavelengths were measured alternatingly. (For details about the laser system see Fig. A.1.)

After calibration of the wavemeter, the measured value for the reference drifted slightly away within a range of $\sim \pm 8$ MHz. To correct for this, the frequency difference $\Delta\nu_{\mathrm{ref}}$ between ν_{ref} and the measured value was determined. The change in the measured frequency was found to be linear with the drift of the reference to good approximation. The frequency of the pump beam was corrected with $\nu_{\mathrm{pump}} = \nu_{\mathrm{pump,\ meas}} - (1.440 \times \Delta\nu_{\mathrm{ref}})$ and the frequency of the signal beam with $\nu_{\mathrm{signal}} = \nu_{\mathrm{signal,\ meas}} - (0.949 \times \Delta\nu_{\mathrm{ref}})$. The offsets in the correction curves were compatible with zero and therefore added to the uncertainties in the frequencies.

3.3 Spectroscopy setup

The spectrometer section is shown in Fig. 3.5. It consists of an entrance diaphragm, a drift tube where laser excitation takes place, a second diaphragm, a deflector, a Faraday cup and a detector for neutral atoms. All diaphragms have a diameter of 7.5 mm. The interaction region between the two diaphragms was initially 434 mm, and after elongation 758 mm long.

Due to the low photodetachment cross section of La^{-}, the use of an intense laser beam was necessary to obtain a detectable detachment signal. In order to keep power broadening

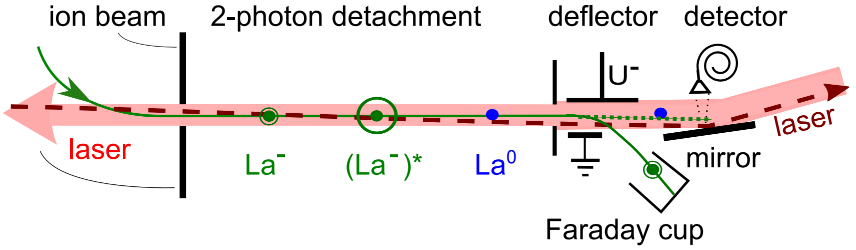

Figure 3.5: (Top) Spectroscopy section with two laser beams. The excitation beam is indicated by the broad pink arrow from the right and the detachment beam with higher power is indicated by the dashed red arrow from the left. The green line is the ion beam and the dotted green line represents the neutrals produced by two-photon detachment going straight onto the detector.

small and to have a better control of the background, separate beams were used for excitation and detachment. As shown in Fig. 3.6, the primary idler beam was split up between the excitation and the detachment beam at a ratio of 30:70. The less intense excitation beam was further attenuated with beam splitters and windows to an intensity between 2...60 mW. In order to ensure a complete illumination of the interaction region, and for a more homogeneous intensity profile in the spectroscopy section, the excitation beam was widened from $\sim$ 6 mm to $\sim$ 12 mm diameter. For the photodetachment of the excited ions the detachment beam with a power of about 1 W was used. Its diameter was kept at 6 mm to ensure that the beam passes through the apertures into the interaction region with its entire power.

In the spectroscopy region, the ion beam and the laser beams are superimposed. The excitation beam was centred in the tube and scanned in the frequency interval where the resonance was expected, according to the prior measurement by Walter *et al.* [Walt2014]. The excitation frequency was scanned bidirectionally by applying a triangular voltage on the piezo input of the seed laser. The scanning range was chosen to roughly 3 GHz with a scanning speed of $\sim$ 0.6–3 MHz/s. Depending on the speed, the time for a single scan was between 20 min and 1 h.

The detachment laser beam was introduced from the opposite direction with a slight angle of at most 1° to the excitation laser. The two laser beams could be reversed in order to switch between collinear and anti-collinear configuration. For the ion beam and the laser beams incident from opposite directions, the Doppler shift leads to a difference in frequencies in the frame of reference of the ions of 50–80 GHz.

In resonance, the excitation laser brings the ions into the $^3\mathrm{D}^o_1$ excited state. If they absorb a second photon, they are neutralized by non-resonant photodetachment. The binding energy of the excited state in La^- is about 100 meV ($\approx$ 24 THz) [Walt2014, O'Ma2009], therefore a detachment of the valence electron by an electric field was not possible as in Os^- (see Sec. 1.3). A deflector guides remaining ions into a Faraday cup, while neutral atoms are detected in forward direction. The detector for neutrals consists of a gold-plated mirror and a channeltron detector.

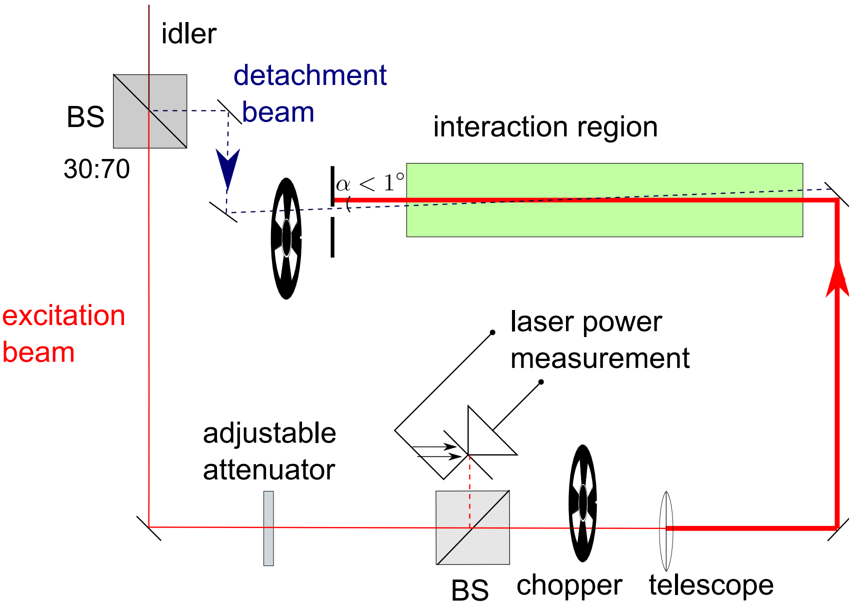

Figure 3.6: The idler beam is split into the detachment and the excitation beam. The excitation beam, indicated with a solid red line, is attenuated by the insertion of windows and beam splitters to a power in the range 0–60 mW. The power is determined by measuring the power of a reflection. The detachment beam (dashed black line) is introduced into the interaction region from the opposite direction.

3.4 Detector

A deflector guides the remaining ions into a Faraday cup while neutral atoms are detected in forward direction. The detector is a single-channel electron multiplier, also called channeltron, in combination with a gold-plated mirror as a secondary-electron emitter. The mirror consists of a solid copper substrate [thickness 12.0(2) mm, diameter 50.8(1) mm] with gold coating. The channeltron is a glass tube with a high-impedance surface layer on the inside. When an ion impinges on the open end (cathode), typically 2–3 secondary electrons are emitted and accelerated by a voltage of −2.500(3) kV toward the grounded anode. In the collision of the secondary electrons with the inner surface, tertiary electrons are produced and so on, such that an avalanche of electrons is created which can be detected as a pulse. For electrons, the detection efficiency of the channeltron has a maximum of about 90% at 500 eV electron energy [Benn1973].

In order to work at the maximum detection efficiency, the mirror was set to a potential of −3.000(3) kV. This has the advantage that negative ions are repelled from the detector and hence the background is reduced. Neutrals are not influenced by the voltage and can impinge on the surface of the mirror to produce secondary electrons.

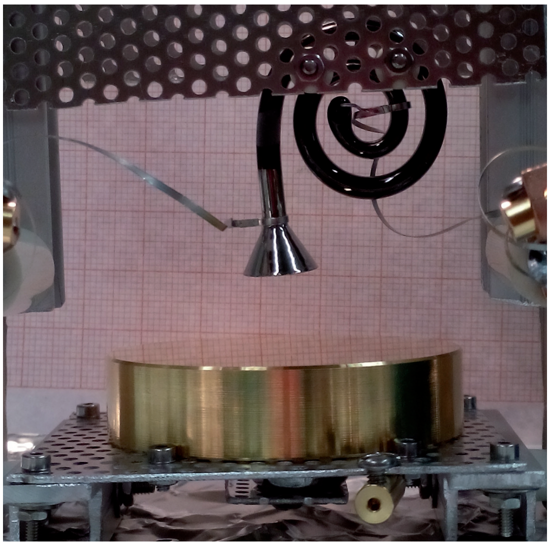

Figure 3.7: Channeltron detector with gold-plated mirror as secondary-electron emitter.

3.5 Data acquisition

To transfer the measured data onto the computer, the pulses from the channeltron are amplified, discriminated (Philips Scientific PS715 constant-fraction discriminator) and digitized (ECL to TTL/NIM). Afterwards the digital pulses are counted on a counter card (National Instruments PCI-6602), which is read out with Labview.

For the measurement, the excitation and the detachment beam are interrupted with two separate optical choppers. The choppers are triggered by a timer card (SpinCore Pulse-Blaster) and carefully phase-locked to each other. The chopping frequency for the detachment laser is 5 Hz, for the excitation laser 50 Hz. There are four possible illumination states, first, with both lasers interacting with the ions; second, the excitation laser shined onto the ions and the detachment laser blocked; third, the detachment laser shined in and the excitation laser blocked; and fourth, both lasers blocked.

The data acquisition scheme is shown in Fig. 3.8. The timing for the data acquisition and the readout is controlled by the timer card. The interval resolution of the timer card is 10 ns. It is used to sort the counts in each illumination state. In order to achieve this, two pulse sequences from the card and the photodiode signals of the chopped laser beams are synchronized. The time during which the light is switched is disregarded. The counting is only active when the laser is completely on or off. Each illumination state is measured for 180 ms, 20 ms are for switching the light. One pulse sequence is programmed for each of the four illumination states. The pulse sequences and the digitized counts are input to the counter card through an AND gate. This way the counts are only forwarded to the counter card during the correct illumination state of the ion beam.

For one measurement point the counts in each of the four illumination states are integrated over 180 ms, plus the time for switching the light. Subsequently to this 800 ms acquisition period, the counting is stopped for 200 ms for the readout. To stop the counting during the readout another sequence from the timer card is input to the gate of the counter card. In total the acquisition of one data point takes 1 s.

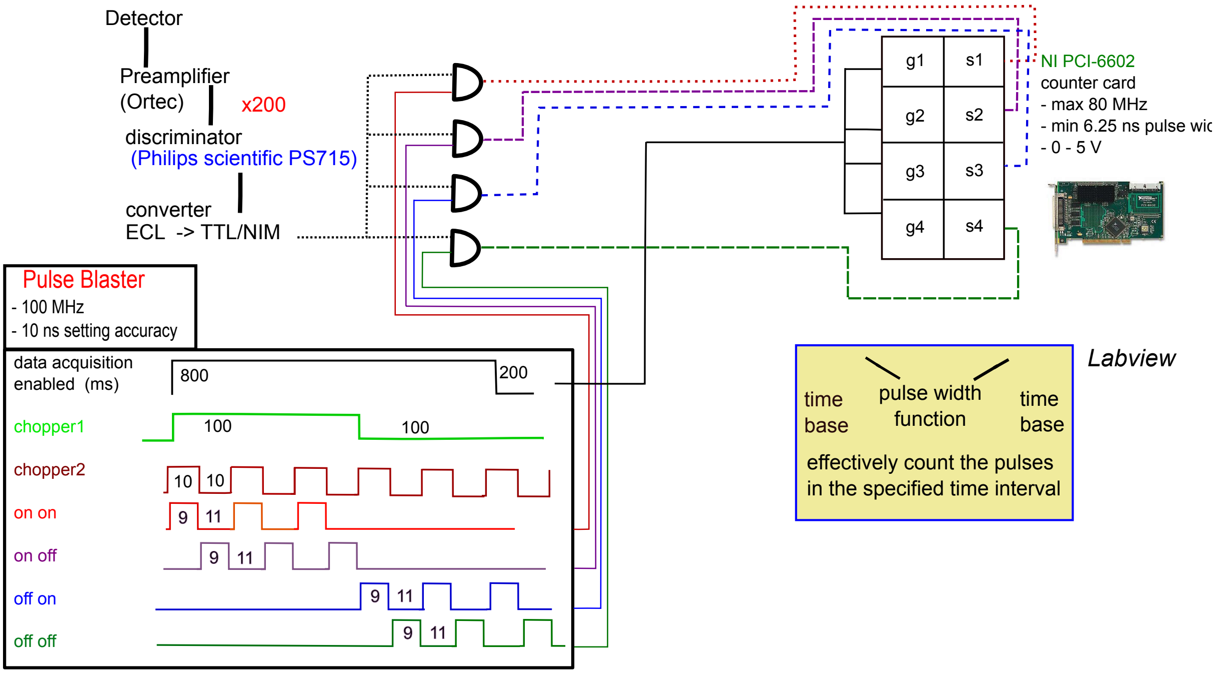

Figure 3.8: The pulses from the detector are digitized and counted with a counter card which is gated by a timer card. The timings are given in ms. The detachment laser is interrupted by chopper 1, whereas the excitation laser is interrupted by chopper 2.

Chapter 4

Experimental results

4.1 Hyperfine spectrum of the proposed laser cooling transition $5d^2\ 6s^2\ ^3F_2^e \rightarrow 5d\ 6s^2\ 6p\ ^3D_1^o$ in negative lanthanum

In order to determine the exact frequencies of the hyperfine transitions between the $5d^26s^2\ ^3F_2^e$ ground state and the $5d6s^26p\ ^3D_1^o$ excited state, we recorded the transition resonance at beam energies of $E_{\mathrm{kin}} = 5$–10 keV. At a given beam energy the frequency of the excitation laser was scanned in the interval in which the resonance was expected, according to the prior measurement by Walter *et al.* [Walt2014] and according to the calculated Doppler shift. The measurement time depended on the signal-to-noise ratio of the individual scans. A good alignment of the ion and the laser beams, a high ion beam current and a pure La^- beam with few contaminants resulted in a high signal-to-noise ratio. The ratio changed from run to run, depending on the residual-gas pressure and the cleanliness of the source. The contaminants in the beam, such as LaO^- and LaH^-, were largely suppressed. The mass separation by the magnet and the diaphragms filtered out elements with a mass more than about two mass units different from ^{139}La, as shown by SimIon simulations in Fig. A.3.1. Still more importantly, when the laser is resonant with the transition in La^-, the detachment probability for La^- is strongly enhanced compared to the detachment of the hydrides LaH_x^-. Thus, even if there is a considerable fraction of hydrides in the beam, the majority of neutral counts originates from La atoms. This effect is shown in Fig. A.5.

4.1.1 Data treatment and background subtraction

The resonance was detected by counting atoms which were neutralized by the laser in the spectroscopy region. In resonance, the laser brings the ions into the excited state. If they absorb a second photon, they are neutralized by photodetachment. A deflector guides the remaining ions into a Faraday cup. The photodetachment cross section of about 10^{-17} cm^2 is orders of magnitude lower than the excitation cross section. Therefore, a strong laser is needed to obtain a detectable signal. However, if the laser is in resonance with the bound–bound transition, a high laser power leads to power broadening of the spectral line. Therefore, two laser beams were used, one with low power for the excitation which was in resonance with the ions, and a second one with higher power of about 1 W for the non-resonant detachment.

Even when no laser is present in the interaction region, there are still background counts from stripping on diaphragms or in collisions with ions of the residual-gas. These counts are always present when the ion beam traverses the spectroscopy region. Furthermore, in the ion beam produced from the sputter ion source, there are always excited ions. The excited states in La$^-$ are expected to have a lifetime of tens of μs. Thus, a fraction of the ions arrive in the spectroscopy section in an excited state. These ions can be detached with only one photon from either the excitation or the detachment laser and therefore lead to another frequency-independent background.

When the excitation laser is tuned into resonance, the ions can be resonantly excited by one photon and non-resonantly detached by a second photon also originating from the excitation laser. This two-photon process is of interest. However, it is only detectable at strong laser power, else it is covered by the background. The signal is strongly enhanced if both the excitation and the detachment laser interact with the ions inside the spectroscopy region. If the laser is resonant, there is excitation by the excitation laser and detachment by the detachment laser. In this case, it is possible to reduce the excitation power to a few milliwatts or less, while the detachment laser power is kept at $\sim$ 1 W. No power broadening is expected because the excitation power is low and the detachment cross section is low as well, such that the fraction of excited ions is small. A depletion of the excited state by detachment would reduce the lifetime of the excited state and broaden the transition line. For the detachment laser powers used in this experiment, the detachment rate increases linearly with the detachment power, as shown in Fig. A.13.

In order to separate the counts of neutral atoms created by different mechanisms, both lasers were chopped with an optical chopper. This made it possible to measure the count rate in four illumination states. First, with both lasers interacting with the ions (R_{11}), second the detachment laser blocked (R_{10}), third the excitation laser blocked (R_{01}), and fourth both lasers blocked (R_{00}). Which background and counts may have to be considered is indicated in Tab. 4.1. Referring to this table, the number of ions which were excited by the excitation laser and detached by the detachment laser R_{res} was obtained by subtracting R_{10} and R_{01} from R_{11} and R_{00}

$$R_{\text{res}} = R_{11} + R_{00} - R_{10} - R_{01}. \tag{4.1}$$

An example of the measured count rates and the resulting signal is shown in Fig. 4.1. Using this procedure, all backgrounds were measured and subtracted. The uncertainty was set to $\sqrt{N}$ for a number of N counts. The background-corrected data were normalized

Table 4.1: Contributions to the count rate as a function of the laser status. "on" laser interacting with the ions; "off" laser blocked. "exc" abbreviation for excitation laser, "det" abbreviation for detachment laser. * a fraction of ions from the source is in an excited state; R_{00} designates ions neutralized by collisions and is contained in all count rates; R_{01} already excited ions are detached by the detachment laser; R_{10} ions are detached and excited by only the excitation laser (excitation from the source included); R_{11} comprises all other contributions and in addition ions excited by the excitation laser and detached by the detachment laser (exc/det), these are the counts we are interested in.

	laser status		excited by/detached by			
counts	exc	det	exc/det	exc/exc	*/det	collisions
R_{11}	on	on	x	x	x	x
R_{10}	on	off		x		x
R_{01}	off	on			x	x
R_{00}	off	off				x

both to the excitation laser power and to the ion beam current:

$$R_{\text{norm}} = \frac{R_{\text{res}}}{I_{\text{beam}} \cdot P_{\text{exc}}}. \tag{4.2}$$

After normalization the data were binned with a bin size of 1 MHz. For better visibility, the bin width in the plots is 10 MHz. An example for background-corrected and normalized data is shown in Fig. 4.1 (top).

4.1.2 Data fitting

In all 16 records of the hyperfine transitions, a total of seven peaks were observed and numbered Peaks 1–7 in order of increasing frequency. The measured resonance curves were fitted with seven Lorentzians using a non-linear least-squares fit by the Trust-Region algorithm in Matlab. A typical hyperfine spectrum, recorded at 5 keV beam energy, is shown in Fig. 4.2. The peak heights as well as the forced identical widths were free fit parameters. Peak positions were free within limits, such that the frequency ordering of peaks could not be exchanged. The width of the peaks for the anticollinear configuration with 5 keV beam energy and 40 mW laser power, shown in Fig. 4.2 (left), was found to be $\Gamma = 84.3(9)$ MHz. The peak width for the collinear configuration at same beam energy and same laser power, but a shorter interaction region, shown in Fig. 4.2 (right) was $\Gamma = 131.9(1.5)$ MHz.

Given the incidence of two beams from opposite directions, the Doppler shift leads to different frequencies in the frame of reference of the ions. The Doppler shifted resonance

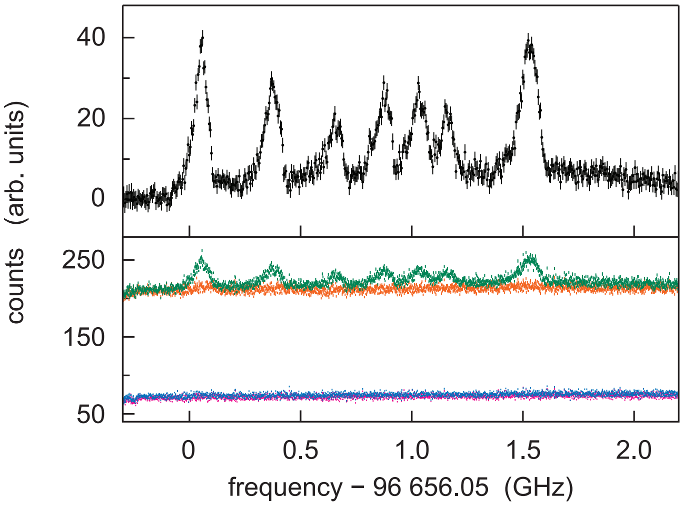

Figure 4.1: (Top) Hyperfine spectrum measured at 5 keV beam energy. The plot is obtained by subtracting the orange and the blue traces from the sum of the green and the magenta traces in the lower pane. (Bottom) Measured counts of neutral La normalized by the ion beam current. The magenta trace represents the counts with both lasers blocked (R_{00}) ; the blue trace with excitation laser only (R_{10}); the orange trace with detachment laser only (R_{01}); the green trace with both lasers on(R_{11}) .

frequencies ν_L in the laboratory frame are given by special relativity as

$$\nu_\mathrm{L} = \nu_0 \frac{1 \pm v/c}{\sqrt{1-(v/c)^2}}, \tag{4.3}$$

where ν_0 is the resonance frequency in the ions' rest frame, (+) is for the laser beam travelling in the same direction (collinear configuration) and (−) for the anticollinear configuration. The expected Doppler shift for beam energies from 0–12 keV is shown in Fig. 4.3.

With a Doppler shift of 50–80 GHz, the detachment laser is off-resonance, but still far from other fine-structure transitions, which are offset by 3 THz [Walt2014]. As a first consistency check, a simple first-order Doppler correction was made. The measured frequencies ν of the anticollinear measurements were divided by the calculated Doppler factor for the respective beam energy. By this operation, the hyperfine spectra with different Doppler shifts were shifted to the same frequency, as shown in Fig. 4.4, confirming that the spectra are Doppler-shifted as expected. It was found that the frequency offsets between the hyperfine peaks are the same in the corrected spectra. Further, a slight decrease in the peak widths with increasing acceleration potential was observed. This is partially due to the stronger velocity bunching effect, partially due to lower laser powers used for the excitation of the ions in the measurements at higher acceleration potentials between the target and the extraction electrode.

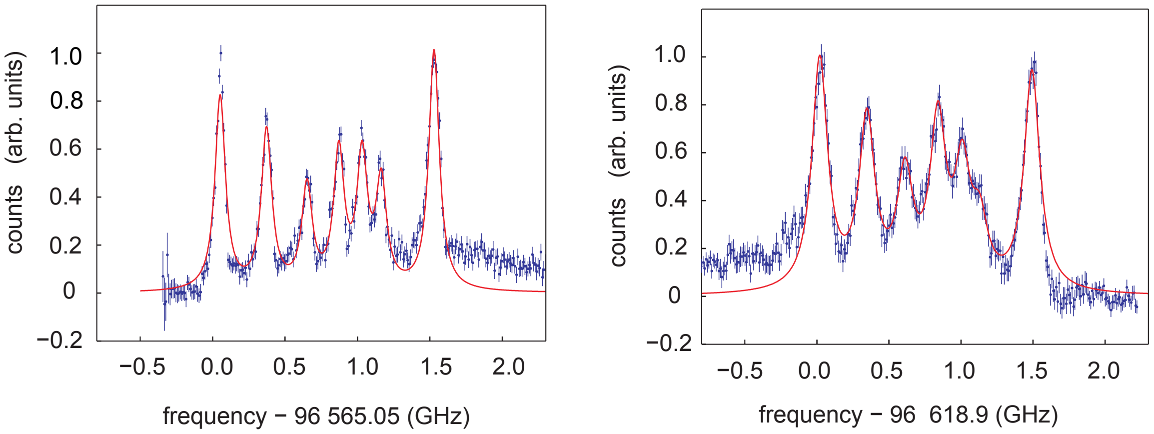

Figure 4.2: Typical resonance in La$^-$ measured at 5 keV beam energy in the anticollinear (left) and collinear (right) configuration. The blue dots are the normalized counts. The fitted curve is the sum of seven Lorentzians. The peak heights, the peak positions and the (forced identical) width are free fit parameters.

For this kind of Doppler correction the beam energy must be known exactly. The reproducibility of the acceleration potential is 10^{-3}, according to the manufacturer of the power supply. This leads to an uncertainty in the frequency of the order of 10^{-7}. In addition, the average beam energy is lower than expected from the acceleration potential since some ions do not traverse the full acceleration potential. Therefore, a more elaborate Doppler correction was necessary for a more precise determination of the rest frame transition frequencies. For this purpose, all 16 recorded spectra were fitted as described above. (For records at different ion beam energies see Sec. A.4.) The uncertainties of the count rate in the ordinate dimension were increased by factors up to 4.2, until $\chi^2 = 1$ for the Lorentzian fits, to account for the asymmetric peak shapes.

The Doppler shifted transition frequencies of the seven hyperfine transitions were determined from the fit, as were the relative peak heights and the fitted width. Uncertainties of the fit parameters were extracted from the traces of the covariance matrices [Bran1999].

The transition frequencies in the rest frame of the ions can be determined from bidirectional measurements [Blon1994, Kaiv1985]. In relativity, the rapidity ϕ can be used instead of the velocity v for Lorentz transformations. It is defined by [Robb1911]

$$\tanh\phi = \frac{v}{c} = \beta. \tag{4.4}$$

Using this definition, the Lorentz transformation takes the form of a multiplication with e^{ϕ}, which is given by

$$e^{+\phi} = \gamma(1+\beta) = \sqrt{\frac{1+\beta}{1-\beta}}, \tag{4.5}$$

where “+” refers to ions moving in opposite direction with respect to the laser. Since $e^{\phi}e^{-\phi} = 1$, the geometric average can be taken to correct for the Doppler effect. For two

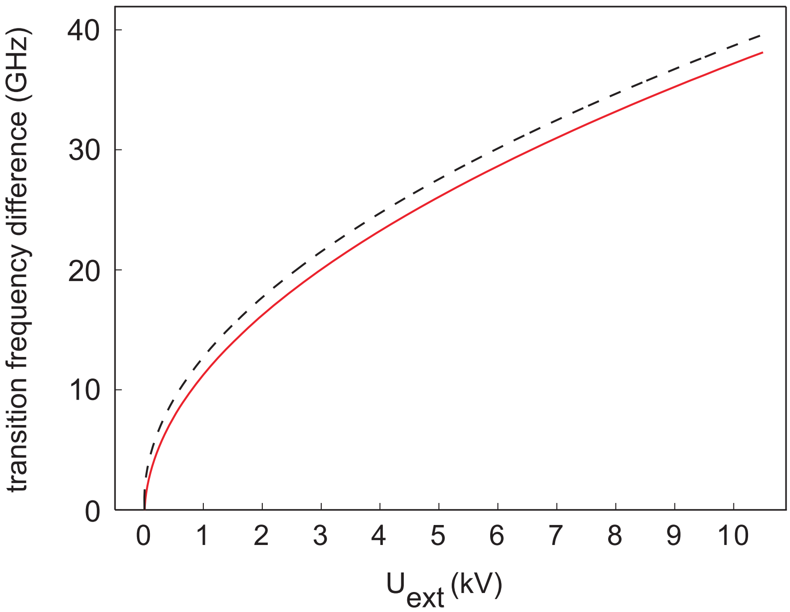

Figure 4.3: Doppler-shifted resonance frequency calculated for Peak 1 at $\nu_L = 96\ 592$ GHz (solid red line) and Peak 7 at $\nu_L = 96\ 593$ GHz (dashed black line) using Eq. (4.3). The shown positive frequency shift is for the collinear configuration, the negative frequency shift for anticollinear configuration is obtained by reflecting the curves across the x-axis.

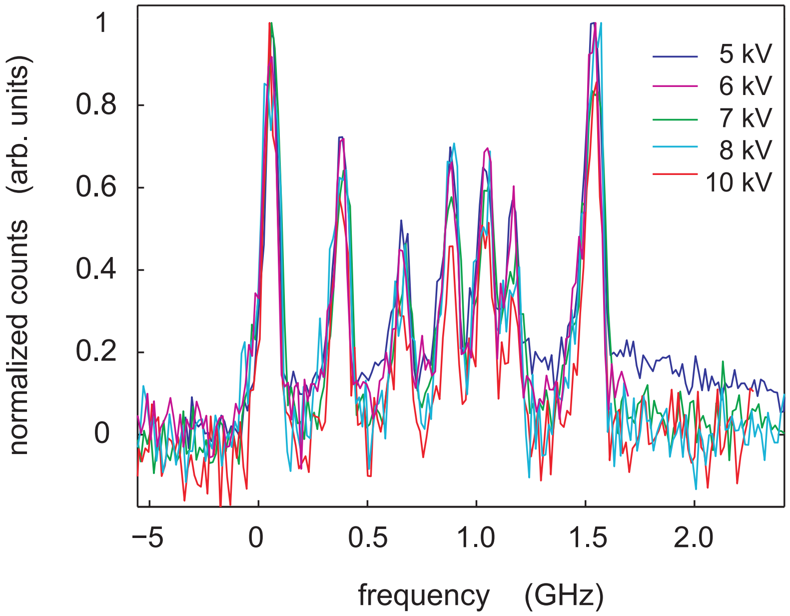

Figure 4.4: Doppler-corrected resonances for the anticollinear configuration at 5, 6, 7, 8 and 10 keV beam energy. For each beam energy the Doppler shift was calculated using Eq. (4.3) and the measured frequencies were divided by the Doppler factor. The velocities of the ions were calculated from the set acceleration voltages.

resonance frequencies determined from collinear and the anticollinear measurements, the resonance frequency in the rest frame of the ions is [Kaiv1985]

$$\nu_0(\mathrm{geom}) = \sqrt{\nu_{\mathrm{coll}} \times \nu_{\mathrm{anticoll}}}. \tag{4.6}$$

Taking the geometric average corrects for the Doppler shift at all orders and there is no need to measure the beam energy as long as it is exactly equal for both measurements.

For the measurements at 5, 6, 7, 8, and 10 keV beam energy, the geometric average of the resonance frequencies was calculated. If there was more than one measurement for the same configuration at the same beam energy, the weighted mean was taken. The frequency in the rest frame of the ions for each of the seven hyperfine transition peaks was obtained by taking the weighted mean of the determined geometric averages at different beam energies. The results can be found in column 2 of Tab. 4.2.

As a cross check, the measured frequencies were plotted as a function of the kinetic energy. In this way, the beam energies can be fitted with a single parabola instead of two branches of a square root function, as shown in Fig. 4.5. The uncertainties of the acceleration potential were expanded to account for the uncertainties in frequency[1]. In order to extract the transition frequencies in the ions' rest frame, the data for each of the seven peaks were fitted with a quadratic fit, according to the first-order Doppler shift formula

$$\nu \approx \nu_0 \left(1 \pm \frac{\sqrt{2eU_{\mathrm{ext}}/m_{\mathrm{La}}}}{c}\right) \quad \Rightarrow \quad U_{\mathrm{ext}} \approx \frac{m_{\mathrm{La}}}{2e}\frac{c^2}{\nu_0^2}\left(\nu - \nu_0\right)^2. \tag{4.7}$$

The function for the acceleration potential is quadratic in ν; the rest frequencies are the abscissa values at the minima of the parabolas. The results are summarized in column 3 of Tab. 4.2. The parabola fit has the advantage that it averages all data points in a single step, whereas for the determination of the geometrical average three averages need to be taken. For both methods it is essential that the beam energy is exactly equal for the collinear and anti-collinear measurements, because a difference in the two beam energies leads to a systematic shift. For comparison the rest frame frequencies resulting from both methods are plotted in Fig. 4.6. The results coincide well within one standard deviation, although the parabola fit only corrects for the first-order Doppler shift. At the beam energies used in this experiment $\beta = v/c \approx 10^{-4}$, the second-order Doppler shift of the order of $\beta^2 \approx 10^{-7}$ was within the experimental uncertainty of the frequencies.

---

[1] In general, if a function $f'(y)$ is fitted rather than $y = f(x)$, the uncertainties σ_i in the measured quantities must be modified by $\sigma_i' = df'(y)/dy_i \times \sigma_i$ [Bevi1992].

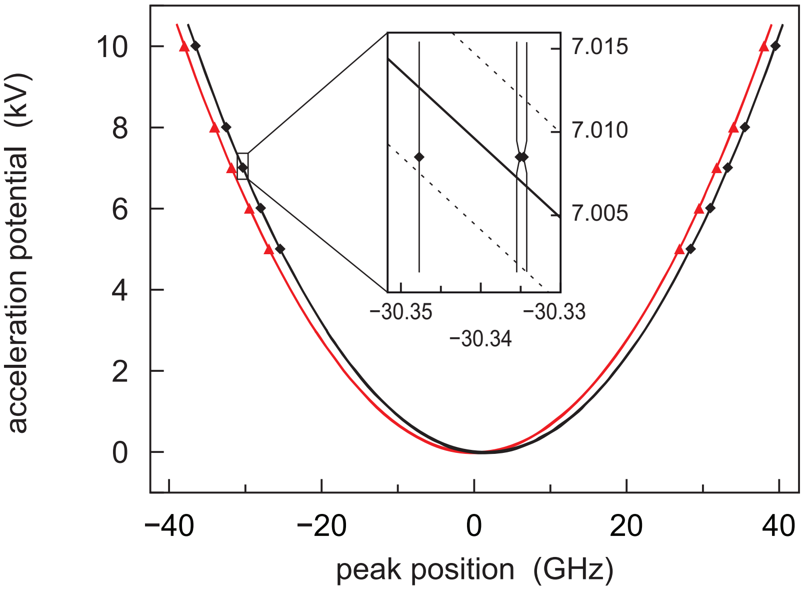

Figure 4.5: Beam energies (acceleration potentials) as a function of the measured resonance frequencies of Peak 1 (red triangles) and Peak 7 (black diamonds). The other parabolas for Peaks 2–6 are not shown for clarity. Collinear and anticollinear measurements lead to blue- and redshifted frequencies, respectively. The data were fitted with a quadratic fit. The minimum of the parabola corresponds to the rest frequency. The inset shows the 1σ confidence bounds of the data at 7 kV acceleration potential in the anticollinear configuration.

Table 4.2: Relative transition frequencies of the hyperfine transitions in the rest frame of the ions, with statistical uncertainties. The second column is the frequency in the rest frame of the ions calculated using the geometrical average of the collinear and anticollinear measurement, the third column is the rest frame frequency determined from the parabola fit (Fig. 4.5). The uncertainty of the geometrical average is given by the standard deviation of the five values determined at different beam energies. The forth column is the rest frame frequency determined from the parabola fit relative to the geometrical average for the frequencies of the Peak 1 with the combined uncertainty.

Peak	ν_0(geo) (MHz) −96 591 995.4 MHz	ν_0(parabola) (MHz) −96 592 004.3 MHz	ν_0(parabola) (MHz) −96 591 995.4 MHz
1	0.0(9.3)	0.0(5.8)	9.0(5.8)
2	326(10)	324.3(5.8)	333.2(5.8)
3	605(11)	603.4(5.9)	612.1(5.9)
4	825(13)	824.4(5.8)	833.3(5.8)
5	988(13)	989.3(5.9)	998.4(5.9)
6	1117(10)	1115.1(6.1)	1123.7(6.1)
7	1479(13)	1481.1(5.8)	1490.1(5.8)

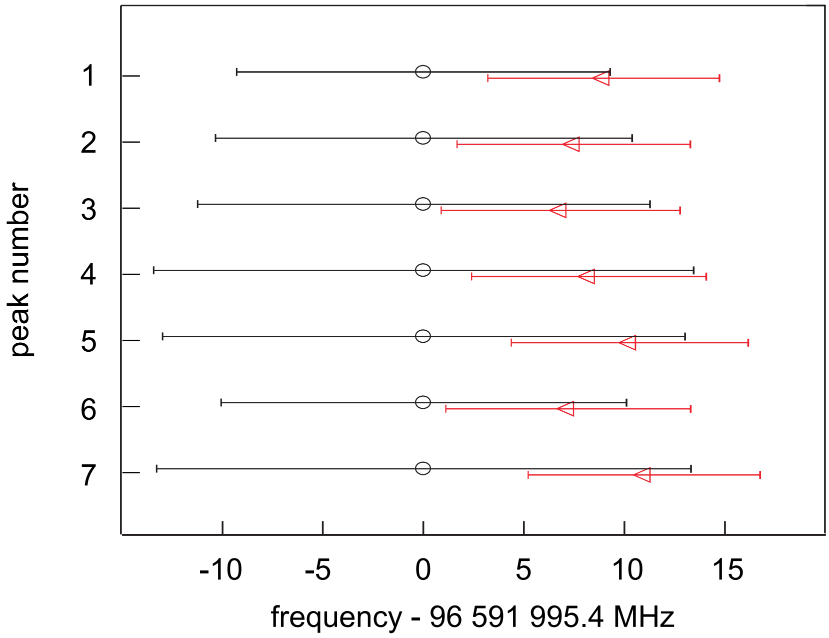

Figure 4.6: Comparison of the rest frame frequencies resulting from the geometric average (black circles) and the parabola fit (red triangles). The results are in good agreement within their uncertainties. The indicated frequencies are relative to the result from geometric averages.

4.1.3 Line shape and broadening

The observed width of the transition peaks is a complex function of velocity bunching, as well as Doppler and power broadening. Most spectra were recorded at about 40 mW excitation power. At this laser power, power broadening was observed. The Doppler broadening has two contributions, one due to the temperature of the target, $\approx$ 1600 K, which leads to a Doppler width of $\nu_D = 235$ MHz. The second contribution originates from a variation of the acceleration potential perceived by the ions. The ions can be produced on the surface of the target or by collisions with excited Cs a few µm above the surface. The acceleration potential is applied between the target and the extraction electrode on a distance of about 20 mm. A difference in position of a few µm corresponds to a voltage difference of 1 V. On this length scale the oxide layer and the roughness of the surface of the target may have an impact. For those ions with a shorter path inside the acceleration region, the kinetic energy is reduced. This explains a small voltage offset of about 20 V for the parabolas in Fig. 4.5. Since the rest frame frequency is determined only by the frequency at which the minimum occurs, not by the minimum value of the kinetic energy, this offset has no influence on the result.

The velocity bunching effect reduces the Doppler width, as explained in Sec. 2.4. For the applied acceleration voltages of $U_{\mathrm{ext}} = 5$–10 kV this leads to a reduction of the Doppler width by a factor $1/R = 340$–540.

The systematic uncertainties of the frequencies in the rest frame of the ions comprise the uncertainty of the wave meter of 50 MHz (see Sec. 3.2), as well as the uncertainties of the ion-optical potentials and the mass separator current. These latter two effects were estimated from SimIon simulations. The beam line and the trajectories of ions for various potentials and magnet currents were simulated. The velocity distribution of the ions parallel to the laser direction was extracted and the corresponding absorption spectrum was calculated. The contribution to the systematic uncertainty of the resonance frequencies was found to be less than 1 MHz.

Furthermore, the simulation showed that the geometrical cooling effect of the diaphragms led to a narrowing of the velocity distribution by about one order of magnitude. Ions at large angles and with strongly deviating velocities for which the electrostatic deflector is not optimized are blocked by the diaphragms. The distribution of the kinetic energy before and after the first diaphragm of the spectroscopy section is shown in Fig. 4.7. Another broadening effect is the Zeeman splitting in the earth's magnetic field. A magnetic field of $\approx 60\,\mu$T leads to a Zeeman splitting of about 1 MHz, as derived in Sec. 2.2. In ion beams, collisional broadening can generally be neglected [Demt1981b].

The convolution of these broadening and narrowing effects leads to the observed Lorentzian or Voigt line shape. The fit with Lorentzian curves resulted in lower χ^2 values than a fit with Gaussian curves. The FWHM of the Lorentzians in the 16 records at various beam energies ranged from 54 to 211 MHz.

All peaks were slightly asymmetric, with a tail towards higher frequency for red-shifted

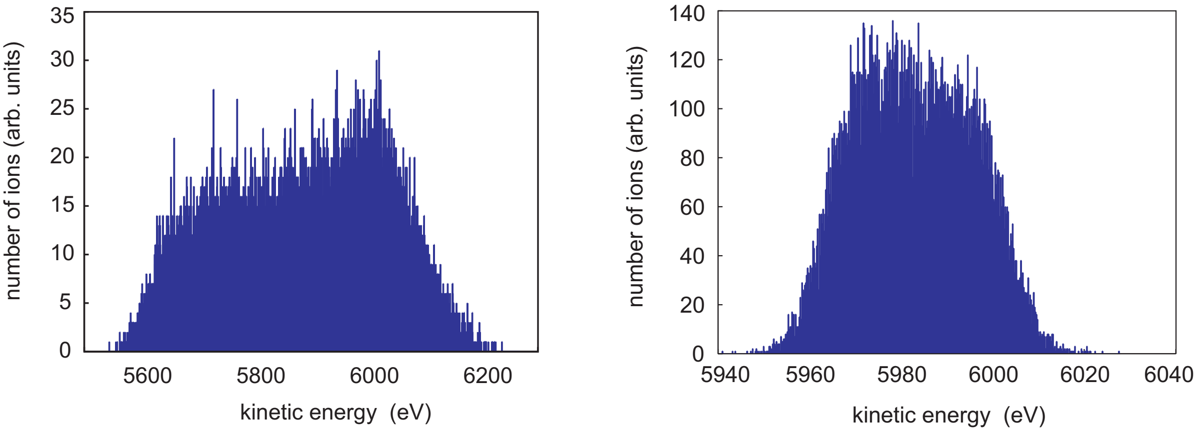

Figure 4.7: Kinetic energy distribution before and after the first diaphragm of the spectroscopy section. After the diaphragm the width of the distribution is strongly reduced (geometric cooling). The energy distribution before the diaphragm corresponds to a Doppler width of $\Delta\nu \approx 600$ MHz, after $\Delta\nu \approx 50$ MHz.

resonances and towards lower frequency for blue-shifted resonances. The tail is caused by the excitation of ions inside the electrostatic deflector. Inside the deflector, the ions still have a radial velocity component, as shown in Fig. 4.8 (left). Thus, their velocity in the direction of the laser, and the Doppler shift, is reduced. This leads to a position-dependent absorption frequency that is responsible for the observed tail or background in the spectra. The tail's direction depends on the laser direction, as observed in Fig. 4.2. An analytic calculation for a monochromatic ion beam without divergence resulted in a 500–900 MHz long tail, depending on the acceleration voltage, as discussed fully in Sec. A.3.3.

However, the electrostatic potential inside the deflector was not taken into account in the calculation. When the ions enter the deflector, their kinetic energy is reduced due to the electro-static potential and increased again to the original value towards the exit of the deflector. To compensate for this, the parameter for the distance over which the ions interact with the laser inside the deflector was increased until the observed tail in the spectrum was reproduced. This effect enlarges the velocity spread of the ions, because deeper inside the deflector the velocity component parallel to the laser is smaller, so the tail in the spectrum is elongated.

In order to reproduce the shape of the peaks taking into account the electrostatic potentials a SIMION simulation was performed. The entire beamline was simulated with a number of 500 000 La$^-$ ions. The beam energy had a Gaussian distribution with a standard deviation of 6 eV and the ions had an angular spread of 2°. The acceleration potential was set to 6 kV. The simulation showed a reduction of the kinetic energy of up to $\sim$0.55 keV in the interaction region, as shown in Fig. 4.8 (right). Over the short path inside the deflector on which the ions interact with the laser, this leads to an additional

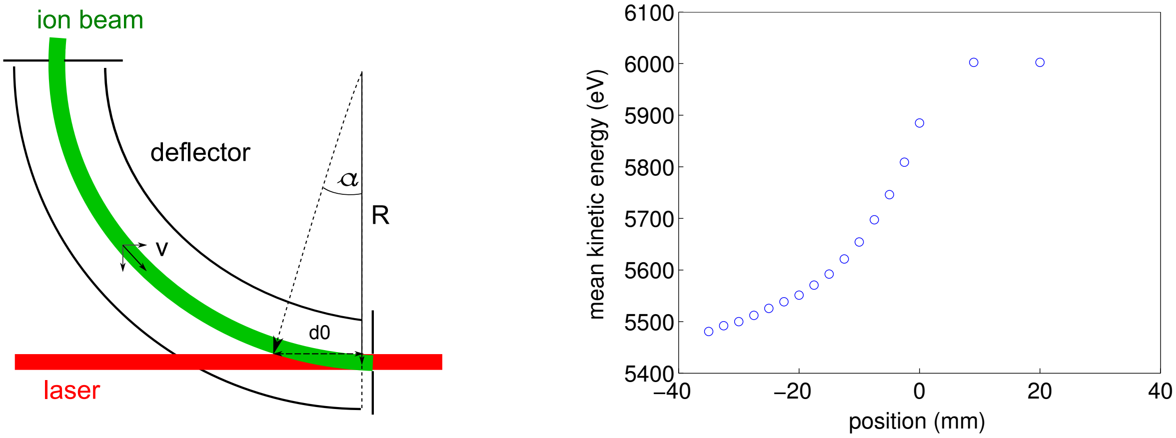

Figure 4.8: (Left) Schematic drawing of the deflector. Inside the deflector the ions have a velocity component perpendicular to the laser, the velocity in the direction of the laser is reduced. The ions interact with the laser over the distance d_0. In addition, the electrostatic potential of the deflector slows the ions down and accelerates them towards the exit. This leads to a reduced Doppler shift, which is observed as a tail of the peaks in the spectrum. (Right) Increase of the mean kinetic energy over the path inside the deflector where ions and laser beams are super imposed. The kinetic energy of the ions decreases due to the electrostatic potential and increases again to the original value towards the exit at zero position.

reduction of the Doppler shift. The result for the shape of the absorption spectrum is shown in Fig. 4.9. The simulated shape of the tail drops off more slowly and extends to much lower frequencies than the analytically calculated shape does if the ion optical potential and the energy reduction are not taken into account. Details about the simulations of the tail are given in Sec. A.3.3.

The contribution to the systematic uncertainty due to the asymmetric shape of the resonance and the overlap between the peaks because of power broadening were estimated by repeating the measurement at various excitation powers between 2–60 mW, as shown in Fig. 4.10. These effects lead to a systematic uncertainty of 30 MHz.

At higher excitation intensities, a significant growth of the tail could lead to a corresponding change in the relative peak heights. The individual peaks were fitted with the analytic expression for the tail with a Lorentzian peak added. This allowed to determine the height of the tails and the Lorentzian peaks separately. As the laser power increased, the relative heights of Peaks 1–6 stayed constant. Only the height of Peak 7 changed, as shown in the lower right pane of Fig. 4.10. This indicates that Peak 7 is a superposition of multiple peaks, which overlap increasingly as the width of the peaks increases. In contrast to the relative peak heights, the relative heights of the tails increased significantly, as shown in Fig. 4.11.

In summary, the systematic uncertainty was estimated as $\Delta\nu_{\mathrm{syst}} = 80$ MHz. Effects which contributed $\lesssim 1$ MHz were neglected. Absolutely, the frequency of Peak 1 was found to be 96.592 004(86) THz. In order to compare the result with the prior measurement without

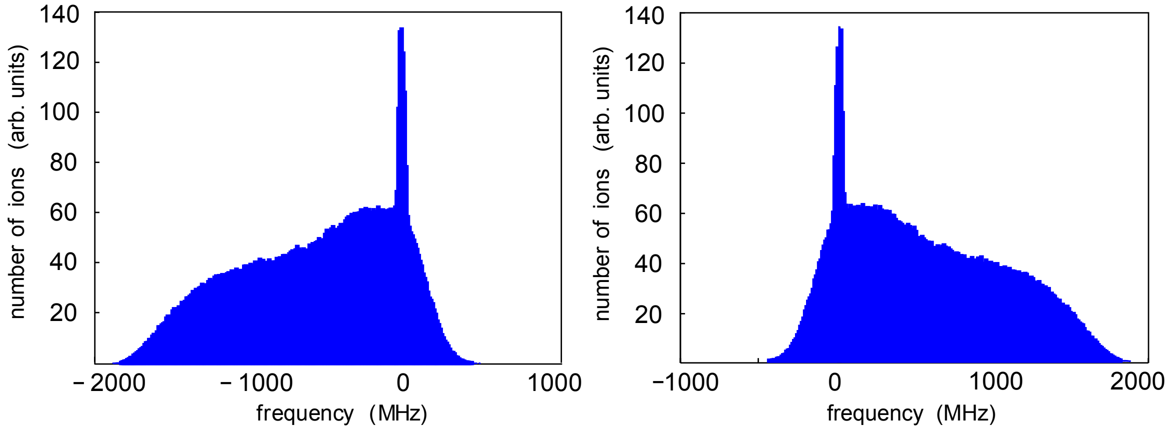

Figure 4.9: SimIon simulation of the absorption spectrum of Peak 1. The broad peak originates from excitation of the ions inside the deflector (black histogram). The absorption spectrum inside the drift tube after geometrical cooling is the sharp peak. The trajectories of the ions in the ion optical potentials at 6 keV beam energy were simulated. The velocity distribution inside the deflector was extracted and the absorption spectrum was calculated. The spectrum for collinear configuration is shown on the left, for the anti-collinear configuration on the right. The simulation included a Gaussian distribution of the kinetic energy with a standard deviation of 6 V and divergence of the ions in the beam of 2°.

a resolved hyperfine structure, the center of gravity (COG) of the hyperfine peaks was determined. Since Peak 7 is the superposition of three peaks, an additional fit parameter for its width was introduced and the records of the spectra were fitted once more. The results are given in Column 8 of Tab. 4.5 and agree well with the results from the previous fit with equal widths for all peaks (see Tab. 4.2).

The fitted widths range from 54 to 211 MHz for Peaks 1–6 and from 57 to 157 MHz for Peak 7. The larger range of the widths for Peaks 1–6 is due to the tails. For the collinear measurements, in which the largest peak widths were observed, the tails extend towards lower frequencies and cause broader fitted widths for Peaks 1–6. To minimize the influence of the tail on the width, only records at low laser power, where the tail does not have a strong impact, were used to determine the average width. On average, Peak 7 was a factor 1.25(2) broader than Peaks 1–6.

Weighting the individual frequencies in Tab. 4.2 with the average peak widths and the fitted peak heights determined at low laser power (Column 5, Tab. 4.5), the COG of the spectrum was found to be $\nu_{\mathrm{COG}} = 96.592\,80(10)$ THz. This result agrees with the prior measurement of Walter *et al.*, which was $\nu = 96.5786(73)$ THz, within 2σ and improves its precision by a factor 73. The precision of the COG may be further improved by measuring the hyperfine spectrum in a strong magnetic field. In the Paschen–Back regime the spectral lines are expected to split up symmetrically around the COG of the hyperfine spectrum. Therefore, the COG can be determined from the peak positions. The relative peak heights and widths, which contribute the largest statistical uncertainty in this measurement, do not need to be considered.

4.1.4 Cross section estimate

Excitation inside the deflector results in a completely different peak shape compared with the sharp Lorentzian peak shape from the excitation in the straight drift tube. This is observed as a non-flat background or a tail of the peaks. The intensity of the tail starts to increase significantly relative to the Lorentzian transition peak at $\approx$ 20 mW laser power. Evidently, a large fraction of the ions are excited inside the deflector, although the interaction region in the straight section is 22 times as long as that inside the deflector. Therefore, this is a strong indication that saturation has already been reached in the drift tube. That observation can be used to estimate a lower limit for the excitation cross section. In order to estimate the excitation cross section with the rate equations Eq. (2.32), the photon flux of the excitation laser Φ_e and the detachment laser Φ_d as well as the detachment cross section and the interaction time need to be known.

- An excitation intensity of 22.3 mW corresponds to a photon flux of $\Phi_e = 7.9 \times 10^{17}\ \mathrm{s}^{-1} \cdot \mathrm{cm}^{-2}$;
- The photon flux of the detachment laser with 1 mW power is about $\Phi_d = 3.5 \times 10^{19}\ \mathrm{s}^{-1} \cdot \mathrm{cm}^{-2}$;
- The path length inside the deflector over which the ion beam and laser beam overlap is 34 mm. At 10 keV beam energy, this corresponds to a time of flight of roughly 0.3 µs;
- An estimate for the detachment cross section has been calculated to be $\sigma_{\mathrm{det}} = 10^{-17}\ \mathrm{cm}^2$ by Pan and Beck [Pan2010].

Inserting these values into the solution to the rate equation for the population of the excited states results in the function plotted in Fig. 4.12. (The detachment cross section can be one order of magnitude larger or smaller without any significant influence on the number of excited ions.)

The tail in the detachment spectrum is very sensitive to the laser power, because the Doppler shift of the ions changes continuously inside the deflector. Once an ion is resonantly excited by a photon which is not in resonance with the ions in the drift tube, its resonance frequency quickly changes and it does not resonantly interact with the laser in the drift tube. Thus, those ions excited in the deflector stay in the excited state until they are detached or decay back to the ground state. That effect increases with the laser power and leads to a large fraction of detached ions which were excited inside the deflector.

In order to estimate the excitation cross section the ratio between the ions excited in the deflector and inside the drift tube was approximately determined. The fitted curve was split into a peak and a tail. Since the peak shapes are only approximately known, it was

Table 4.3: Area of the fitted peak A_p and its tail A_t obtained from the integral of the fit function divided into a peak area and a tail area. The area of the tail was multiplied by 1.2 to account for the part of the tail below the peak. The minimal ratio A_t/A_p is given in Column 2 and the maximal ratio in Column 3. For the minimum ratio the area of the peak is overestimated, while for the maximum ratio A_p is underestimated. The ratio of the areas corresponds to the ratio of detached ions which were excited inside the deflector and inside the drift tube.

laser power (mW)	minimum ratio A_t/A_p	maximum ratio A_t/A_p
22	1.3	2.3
28	2.3	4.2
38	2.7	5.7
56	3.1	7.0
64	2.8	6.0

once divided so that the peak area A_p is overestimated and once so that the area of the tail A_t is overestimated, as shown in Fig. 4.13 (left). The integral of the entire fit function and of the tail only were determined. The area of the peak was obtained by subtracting the tail (indicated in Fig. 4.13) from the integral of the fit function. As shown in SIMION simulations, about 20% of the ions excited inside the deflector contribute to the total area below the peak. This was taken into account by multiplying the area of the tail by a factor 1.2. The resulting ratios between the area of the tail and the total area below the peak are given in Tab. 4.3.

As expected, the area of the tail increases with increasing excitation laser power, while the area of the peak slightly decreases. The increase of the ratio of the area below the tail is compared to the fraction of excited ions inside the deflector calculated with the rate equations. The fraction of ions in the excited state after 0.3 μs is calculated for the laser powers used in the experiment with the excitation cross section as a variable parameter. By varying the excitation cross section the theoretical fraction of excited ions is fitted to the slope of the area ratios, as shown in Fig. 4.14. The comparison leads to a range of possible values for the excitation cross section, so that the calculated and observed fraction of ions excited inside the deflector are commensurate. The ratio of the areas of Peak 1 to the area of its tail suggests that the cross section lies within 1.7×10^{-12} cm$^2 \leq \sigma_{\text{exc}}$ and $\sigma_{\text{exc}} \leq 2.9 \times 10^{-12}$ cm^2. For an excitation cross section below 10^{-13} cm^2 less than 6% of the ions are excited within 0.3 μs. This cannot explain the observed height of the tail.

However, there are some effects which might lead to an over- or underestimation of the area of the peak and its tail. On the one hand, one has to keep in mind that the estimate was based on a model fit. It cannot be determined from the data how well this fit function describes the actual shape of the tails, because only the sum of the tails is observed. It is assumed that the tails are not yet in saturation. Saturation could lead to different relative transition strengths and hence to different relative heights of the tail shoulders. In this case the tail of Peak 1 would be overestimated.

On the other hand, there are effects which may lead to an underestimation of the cross section. The volume of overlap of the ion beam and the laser beam inside the deflector approximately has a wedged shape. Therefore, for more than half of ions the interaction time inside the deflector is even shorter than 0.3 µs. The decrease of kinetic energy due to the electric field in the interaction region is about 10% of the kinetic energy and does not compensate for this. Thus, the cross section might be about 50% higher than estimated. For simplicity, spontaneous decay and decay to states outside this system was neglected in the solutions for the rate equations. This introduced another source of uncertainty. The extend of this uncertainty depends on the lifetime of the excited states.

In conclusion, the excitation cross section of Peak 1 is estimated to be of the order of $\sigma_{\mathrm{exc}} = 10^{-12\pm1}$ cm^2. In combination with the observed peak widths this corresponds to an Einstein A_{21} coefficient for the transition underlying Peak 1 [see Eq. (2.30)] of $A_{21} = \mathcal{O}(10^4)$ s^{-1} and a lifetime τ between 5 µs and 500 µs. The A_{21} coefficients for the other transitions are expected to scale with the coefficient for Peak 1 like the theoretical transition strengths given in Tab. 2.1. The saturation intensity I_{sat} is about 6.6 Wm^{-2}. The intensities used for excitation in this measurement of 45–1360 Wm^{-2} exceed this value by a factor 7–207. The estimated spontaneous transition rate is of the order of magnitude which was predicted by O'Malley and Beck [O'Ma2010]. Their prediction for the transition rate was $A_{21} = 2.9 \times 10^4$ s^{-1} (summed over all hyperfine transitions).

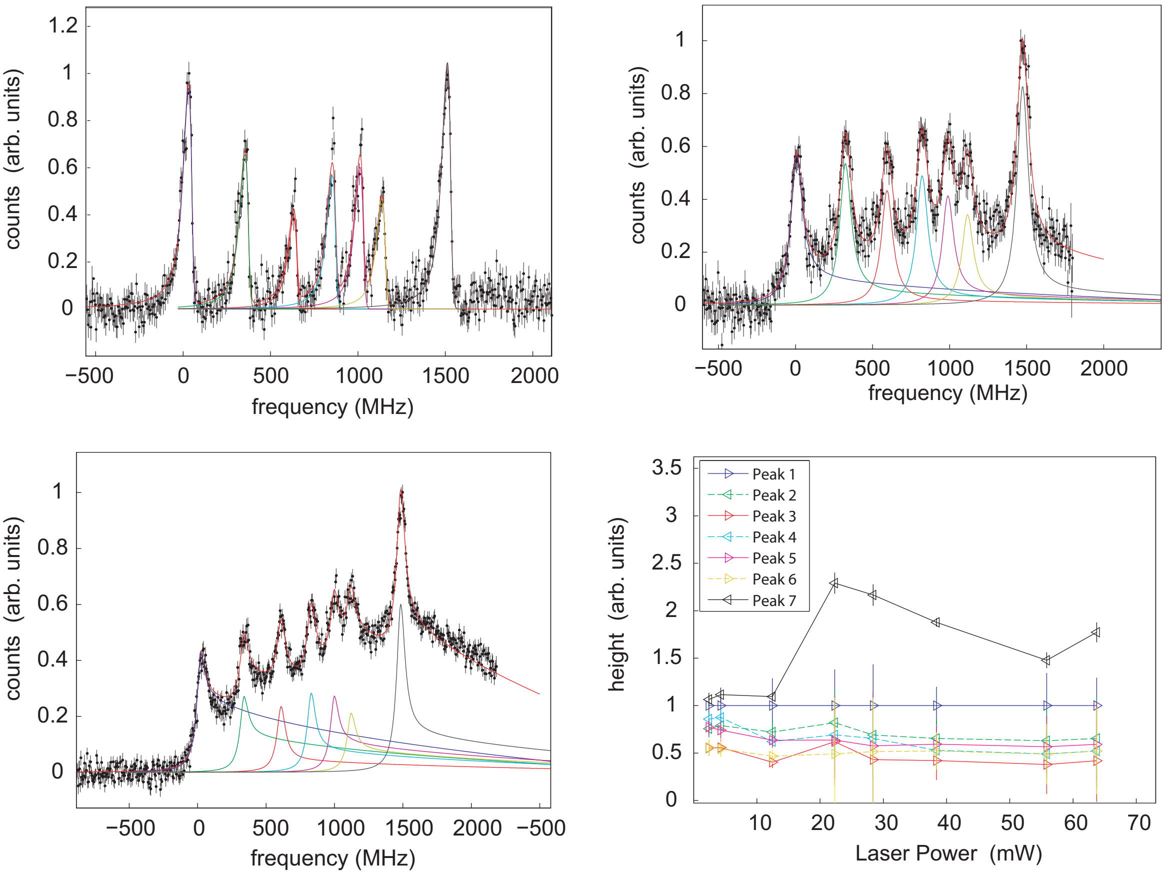

Figure 4.10: Measured spectra at 10 kV acceleration potential and excitation laser powers 2.4 mW (upper left), 22 mW(upper right), 56 mW (lower left) and fitted peak heights relative to Peak 1 (lower right). The data were fitted with seven Lorentzians with tails, indicated by the solid colored lines. The tail is fitted with an analytical expression for the velocity distribution inside the deflector. The red line indicates the sum of the individual peaks. At low power the Lorentzian is cut, most probably due to an improper alignment of the ion beam; for the higher laser powers the tail grows. The relative peak heights stay constant, except for Peak 7, for which the height increases, indicating a superposition of more than one hyperfine transition.

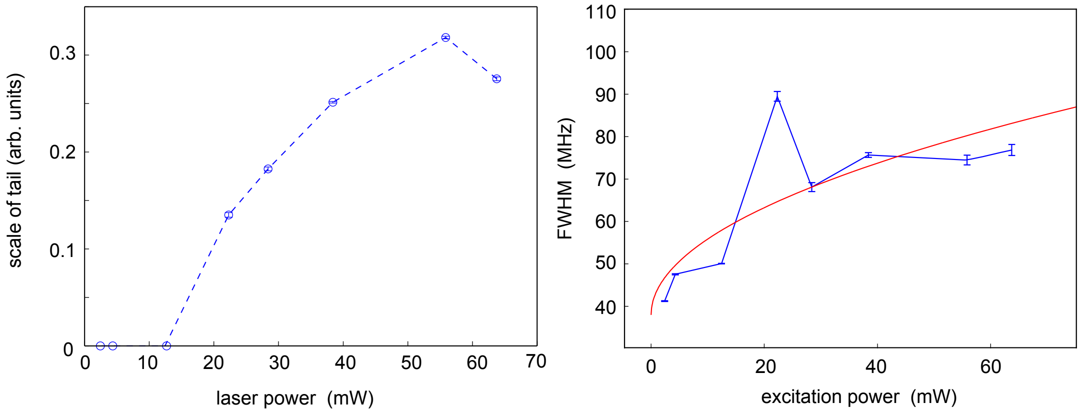

Figure 4.11: (Left) Height of the tail shoulder as a function of laser power. The heights are obtained from the fit with the analytical function describing the tail shape. (Right) The peak widths of the fitted Lorentzians approximately show a square root behavior (as expected for power broadening), as indicated by the square root fit (solid red line). The blue lines are meant to guide the eye.

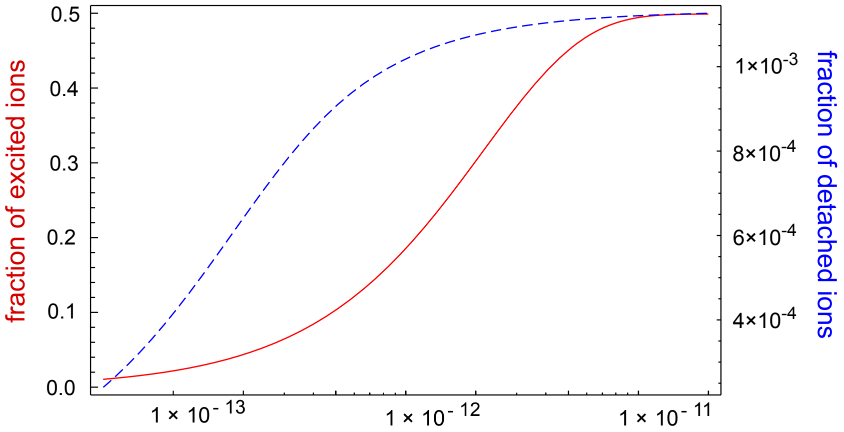

Figure 4.12: Solutions for the rate equations at 22 mW excitation power and 10 keV beam energy are plotted. The population of the excited state inside the deflector as a function of the excitation cross section σ_{exc} is shown (solid red line), as well as the fraction of detached ions inside the drift tube (dashed blue line). To reach a considerable population of the excited state $> 20\%$ the cross section must be of the order of 10^{-12} cm^2. For this estimated excitation cross section a fraction of about 6×10^{-4} of the La$^-$ ions in the ground state are detached.

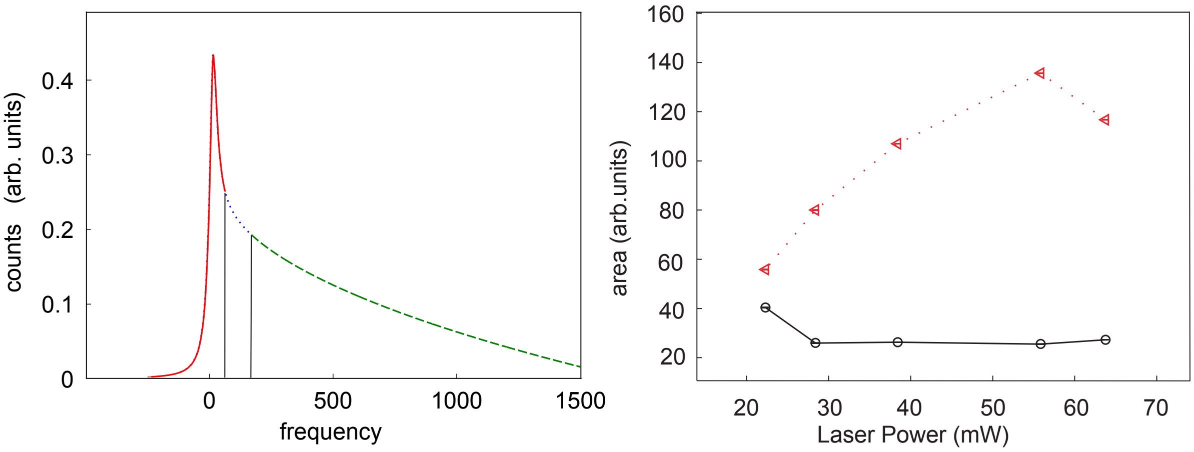

Figure 4.13: (Left) The area below the fit function for Peak 1 was divided into the area of the peak (solid red) and the area of the tail (dashed green). The vertical black lines indicate the two different divisions for the maximal peak area and the minimal peak area to be expected. The area below the peak corresponds to the number of detached ions excited inside the drift tube, while the area below the tail corresponds to detached ions excited inside the deflector. To account for the contribution to the peak area from ions excited inside the deflector, the area of the tail was multiplied by 1.2. (Right) Area of the peak (black circles) and the tail (red triangles) for a separation halfway in between the limits. The peak decreases with the excitation laser power, while the tail increases. The lines are meant to guide the eye.

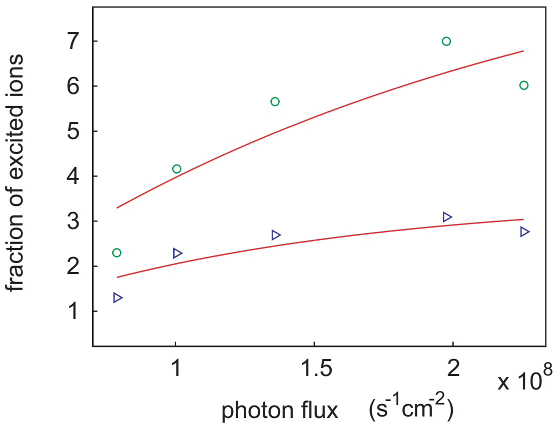

Figure 4.14: Minimum and maximum ratio of the tail to the peak area (blue triangles and green circles) fitted with the solution of the rate equation for the population of the excited state (red lines). The excitation cross section is a free fit parameter. The cross sections which are commensurate with the data are determined by the best fit.

4.2 Hyperfine structure fit

The observed transition peaks for the $^3\mathrm{F}_2^e \rightarrow {}^3\mathrm{D}_1^o$ hyperfine structure transition in La$^-$ were assigned to the transitions between specific hyperfine structure levels by a model fit. With the total angular-momentum quantum numbers $F_{\mathrm{gnd}} = 3/2, \ldots, 11/2$ for the ground state and $F_{\mathrm{exc}} = 5/2,\ 7/2,\ 9/2$ for the excited state, the ground state splits into five, whereas the excited state splits into three hyperfine sub-levels. Therefore, nine allowed hyperfine transitions are expected. The hyperfine splitting is due to the magnetic-dipole and the electric-quadrupole interactions with interaction energies ΔW_{mag} and ΔW_Q which add to the fine-structure energy W_J. The hyperfine structure constants of the ground and the excited state are A_{gnd}, A_{exc}, B_{gnd}, B_{exc} and are defined in Sec. 2.1. In terms of the constants, the energy ΔW of a transition between hyperfine states is given by

$$\begin{aligned}\Delta W &= W_{\mathrm{J,\ exc}} + \Delta W_{\mathrm{mag,\ exc}} + \Delta W_{\mathrm{Q,\ exc}} - (W_{\mathrm{J,\ gnd}} + \Delta W_{\mathrm{mag,\ gnd}} + \Delta W_{\mathrm{Q,\ gnd}}) && (4.8)\\ &= \Delta W_J + h \cdot \left[A_{\mathrm{exc}} \frac{C_i}{2} + B_{\mathrm{exc}} \frac{D_i}{2} - \left(A_{\mathrm{gnd}} \frac{C_j}{2} + B_{\mathrm{gnd}} \frac{D_j}{2} \right) \right], && (4.9)\end{aligned}$$

where h is Planck's constant, and the coefficients C and D depend on the quantum numbers of the respective hyperfine level. They are defined by Eqs. 2.11 and 2.12, respectively. The A and B constants have units of frequency. A schematic level diagram is shown in Fig. 4.15.

The hyperfine structure constants A and B determine the scale of the hyperfine splitting and thus also the scale of the frequency differences between the transition lines in the spectrum. The constants A and B were determined by fitting nine Lorentzians to each of the nine spectra featuring the highest resolution. The position of each of the nine Lorentzian curves was given by Eq. (4.9) with the calculated C and D coefficients. The A and B, as well as the offset $\Delta W_J/h$, were free fit parameters. The peak width was left as a free parameter, but forced to be the same for all peaks.

The aim of the fit was to scale the distances between the peaks such that the positions of the Lorentzians coincide with the transition frequencies in the spectrum. For example, when A_{gnd} is set to zero, there are three Lorentzians visible which are the sum of multiple transition peaks representing transitions to the same excited state, see Fig. 4.16 (left). The relative positions of the energy levels are given by the coefficients C and D, the distance scales with A_{exc} and B_{exc}. In prior studies on neutral La, it was found that ^{139}La has a small quadrupole moment [Basa2009, Nigh2010, Ting1957]. It is expected that B_{exc} and B_{gnd} are within a range from 0–50 MHz, and A in a range from about $-500\ldots500$ MHz [Basa2009]. Since B is expected to be smaller than A, and since B is multiplied by D, which is about an order of magnitude smaller than C, the positions are mainly determined by A. A smaller correction is added by B. When A_{exc} is set to zero, one obtains five transition peaks containing multiple transition peaks from the same ground state. Their distances scale with A_{gnd} and B_{gnd}, see Fig. 4.16 (right). When the fit parameters A and B are modified, the Lorentzians are shifted.

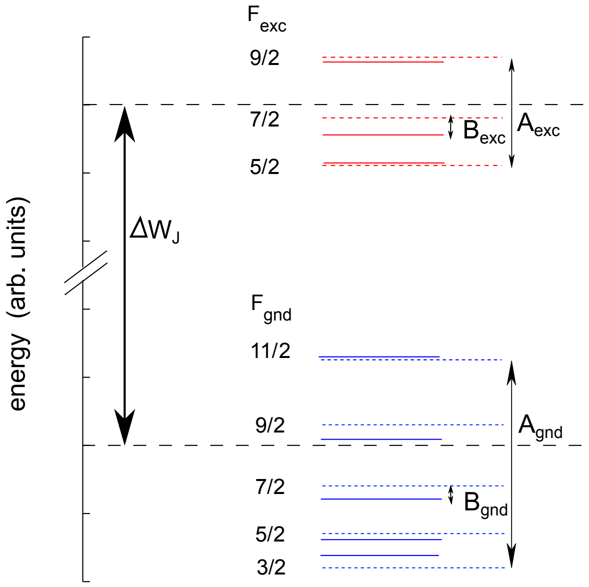

Figure 4.15: Schematic hyperfine level diagram for the $^3\mathrm{F}^e_2 \rightarrow {}^3\mathrm{D}^o_1$ transition in La$^-$. The red levels belong to the excited state, the blue levels to the ground state. The relative distances between the levels (solid lines) is given by the C and D parameters. The distances are not to scale. The hyperfine structure constants A determine the scale of the distances between the levels with B set to zero (dashed lines), the hyperfine structure constants B determine the scale of the distances of the levels from the dashed levels.

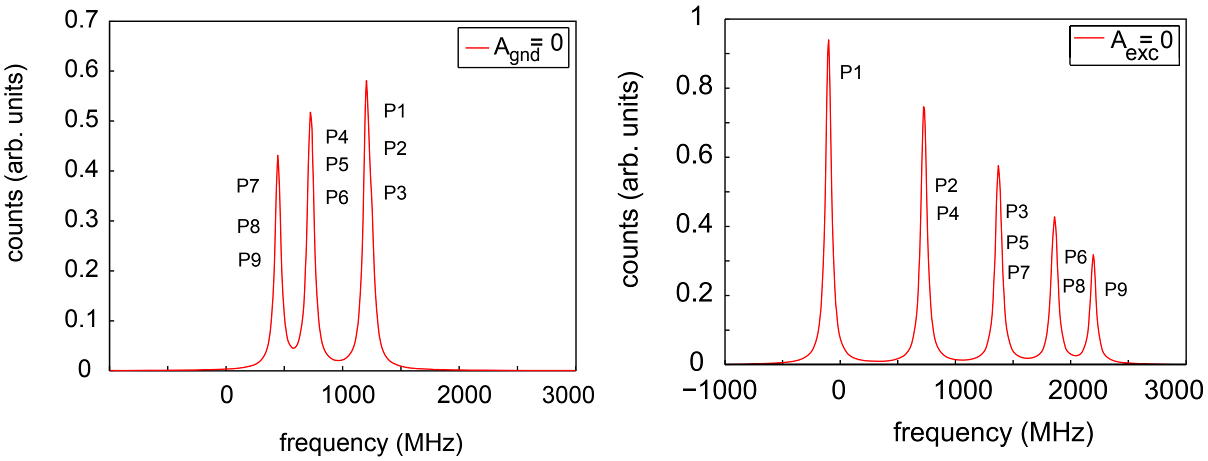

Figure 4.16: Fit function for the hyperfine structure consisting of 9 Lorentzians P1–P9. The hyperfine structure constant A_{exc} scales the distance between three groups of peaks representing transitions to the same excited state (left), the hyperfine interaction constant A_{exc} scales the distance of five groups of peaks originating from the same ground level (right).

There is only one set of values for A and B which reproduce the observed spectrum shown in Fig. 4.18. The best match between the data and the fit was obtained for positive values and $A_{\mathrm{gnd}} > A_{\mathrm{exc}}$. The values of the resulting A and B hyperfine interaction constants are given in Tab. 4.4, the uncertainties are the standard deviations of the results of the eight fits. For these coefficients three transitions are closely clustered in Peak 7. This is compatible with the observation in Fig. 4.10 where only Peak 7 grows to a larger height, while the relative heights of the other peaks stay in good approximation constant. Because the C and D coefficients contain the quantum numbers of the hyperfine states, the fitted Lorentzians are directly connected to transitions between the hyperfine states in Fig. 4.15. By fitting the Lorentzians to the hyperfine transition peaks in the spectra, the observed resonance peaks are assigned to the transitions between the hyperfine levels.

The hyperfine structure fit reveals important characteristics of the hyperfine spectrum of La^-. The peaks are clustered into groups of three peaks, corresponding to transitions with the same ΔF. The first three peaks (at lower frequencies) originate from transitions with $\Delta F = -1$, the second three from transitions with $\Delta F = 0$, and the last three, which are not resolved, from $\Delta F = +1$. The distances between the group of peaks with $\Delta F = -1$ are larger than the distances between the peaks at higher frequencies.

For some atoms a second possible solution can be obtained by exchanging the A and B constants for the upper and lower states and simultaneously inverting the sign. For La^- the quantum numbers of the lower and upper states are different, leading to different C and D coefficients. Therefore, different positions are obtained when the coefficients are exchanged and inverted, as shown in Fig. 4.17 (right). Negative values for the A interaction constants do not lead to a satisfactory fit, as the distances between the peaks of the fit function are too large at higher energy and too small for the peaks at lower frequencies. It was also tried to use large values for the B coefficients, but this led to similar incompatibilities between the data and the fit.

In principle, the relative peak heights of the Lorentzians are free fit parameters. However, if the peak heights are left free, one peak within Peak 7 is always fitted to zero, as shown in Fig. 4.18. So, one of the nine transition peaks is missing. To avoid this the relative heights of the peaks can be fixed. The theoretical relative peak heights for the hyperfine transitions are given in Tab. 2.1. Using these values results in the fit in Fig. 4.19. These peak heights do not fit the data well.

As indicated in Sec. 4.1, the excitation intensities used for the measurements were always close to saturation. It was found that relative heights for saturated transitions scaling with the multiplicities of the levels (see Tab. 2.2) fit the data much better, as shown in Fig. 4.20. This indicates that the transitions are close to saturation, even at the lowest excitation laser power of 2.4 mW. Regardless of the choice of peak heights in the fit, the hyperfine interaction constants A_{gnd}, B_{gnd}, A_{exc}, and B_{exc} in Tab. 4.4 are the same within their uncertainties because they mainly depend on the positions of the peaks. However, the order of the closely clustered Lorentzians P7 a)–c) varies for the different peak heights because the relative heights of the Lorentzians are different. For example,

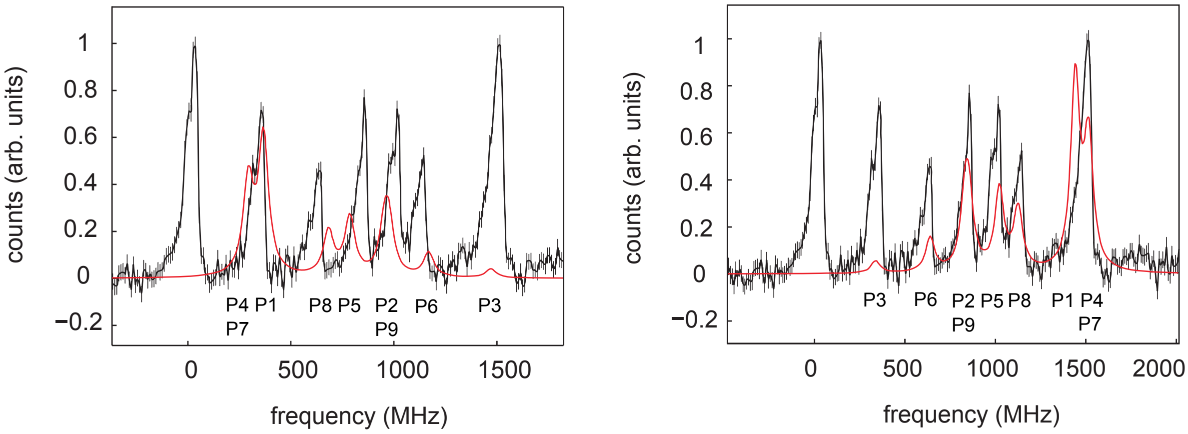

Figure 4.17: Fit function for the hyperfine structure consisting of 9 Lorentzians (red line). The black curve is the data for comparison. (Left) the optimal values for the A and B parameters were exchanged such that $A_{\text{exc}} > A_{\text{gnd}} > 0$. The positions of the Lorentzians towards low frequencies are too close to fit the data. (Right) the values for the A and B parameters were exchanged and inverted. With negative values for the A parameters the distances between the Lorentzians on the left are too small to fit the data. If the parameters are chosen to be larger, the Lorentzians on the right are not merged and do not fit Peak 7.

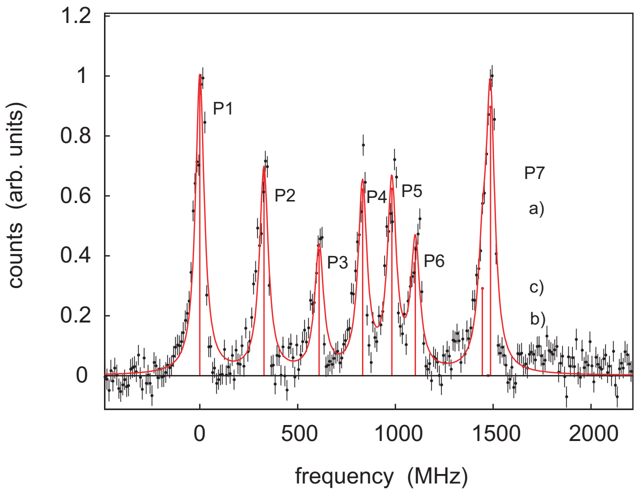

Figure 4.18: Hyperfine spectrum of the transition recorded at 10 kV acceleration potential and 2.4 mW excitation laser power. Fit with 9 Lorentzians of 58.1(8) MHz width (solid red line). The peak heights are free fit parameters. Peak 7 b) is fitted to zero height.

using the relative peak heights in saturation, P7 c) is the highest peak within Peak 7, but the unsaturated theoretical height for P7 c) is the lowest. This leads to an optimal χ^2 for different peak positions, and thus a slightly different value of the hyperfine interaction constants. In addition, the slightly asymmetric shape of the peaks also has an impact on

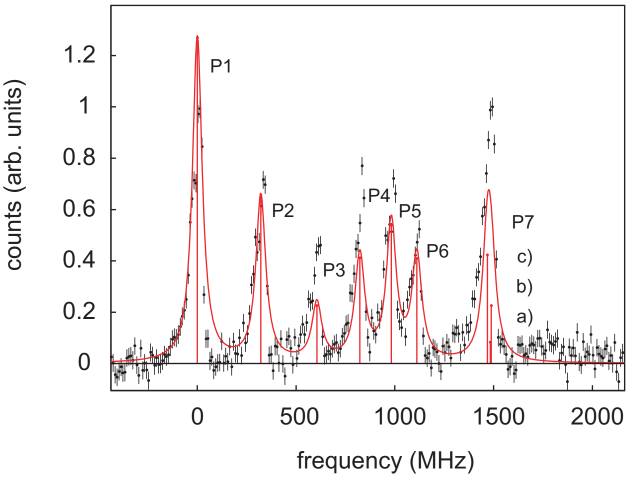

Figure 4.19: Hyperfine spectrum of the transition, fitted with 9 Lorentzians. The fit is indicated by the solid red line. The peak heights are the theoretical heights from Ref. [Whit1933] scaled by a factor which was a free fit parameter. The peak width is 60.0(1.4) MHz.

Table 4.4: Hyperfine interaction constants for different relative peak heights. (Column 2) heights as free fit parameters; (Column 3) theoretical heights according to Ref. [Whit1933]; (Column 4) fit with the saturated relative transition strengths, given in Tab. 2.2. The values agree within their uncertainties.

	free heights	theoretical heights	saturated heights
A_{gnd}	147.22(47)	147.06(44)	146.76(26)
A_{exc}	110.68(80)	109.73(68)	110.55(72)
B_{gnd}	29.5(9.2)	24.0(1.4)	36.3(8.8)
B_{exc}	3.9(2.4)	6.7(2.1)	5.4(1.3)

the optimal positions of the Lorentzians within Peak 7. As a consequence, the positions within Peak 7 cannot be determined reliably.

The positions of all nine hyperfine transitions can be calculated by inserting the fitted hyperfine interaction constants in Tab. 4.4 into Eq. (4.9). The positions were calculated using the fit results from the fit with the saturated relative intensities, see Column 7 Tab. 4.5. For comparison the peak heights and transition frequencies from the hyperfine structure fit with seven Lorentzians, as shown in Fig. 4.2, are included in Columns 6 and 8 of Tab. 4.5. The relative heights determined from the fits at low excitation laser power between 2–13 mW are in good agreement with saturated relative intensities. The positions agree within 2σ for both fitting methods.

The assignment of the resonance peaks to the hyperfine energy levels leads to the level diagram for the hyperfine structure of the ${}^3\mathrm{F}^e_2 \rightarrow {}^3\mathrm{D}^o_1$ transition in La$^-$ shown in Fig. 4.21.

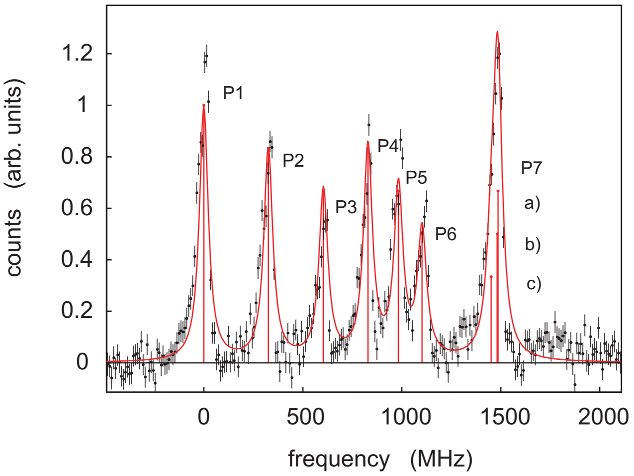

Figure 4.20: Hyperfine spectrum of the transition. The solid red line is a fit with 9 Lorentzians with a width of 54.4(8) MHz. The peak heights are the theoretical relative transition strengths in saturation scaled by a factor which was a free fit parameter.

The knowledge of the hyperfine structure of La$^-$ is an important prerequisite for the development of a laser cooling scheme. All hyperfine ground levels that can be populated during the cooling cycle need to be re-pumped to prevent losses. For efficient cooling a high spontaneous decay rate is necessary. The relative heights of the peaks indicate that Peak 1 has the largest cross section and is therefore the fastest transition.

Cooling can thus be achieved by exciting ions from the 11/2 hyperfine levels of the ground state to the $F = 9/2$ hyperfine level of the excited state. From this excited state, the ions can decay back either to the $F = 11/2$, $F = 9/2$ level or to the $F = 7/2$ level. The $F = 9/2$ and $F = 7/2$ levels have to be re-pumped. Furthermore, all hyperfine levels of the ground state are initially populated. To bring the ions from the $F = 3/2$ and $F = 5/2$ states into the cooling cycle, the transitions with $\Delta F = 1$ from the $F = 3/2$ and $F = 5/2$ ground levels have to be driven. All three transitions with $\Delta F = 1$ are within Peak 7 and could not be resolved in the measurements. This shows that their frequencies differ by less than 50 MHz. As long as the resonance width is larger than 50 MHz, all three transitions may be driven with only one laser, as indicated in Fig. 4.21. When the temperature of the ions is cooled below ~ 72 K, the Doppler width of the transitions becomes smaller than 50 MHz. Depending on the exact frequency differences, it is probably not possible to re-pump all three transitions with a narrow bandwidth of 1 MHz. In order for further cooling to be achieved, a laser with a bandwidth of about 50 MHz will be needed to re-pump the three states simultaneously. Alternatively, the re-pumping laser may be tuned to the $F = 7/2 \rightarrow 9/2$ transition after a brief initial phase, since the $F = 5/2$ and $F = 3/2$ hyperfine sub-levels of the ground state should then no longer be populated. Chirping the laser from time to time should be sufficient to pump back the ions which re-populate the levels by forbidden transitions. These considerations show that it should

Table 4.5: Relative transition amplitudes (Column 6) and relative transition frequencies (Column 8) of the measured peaks for all hyperfine transitions, with respect to Peak 1 at 96.592 004(80) THz. The peak positions result from the hyperfine structure fit, shown in Fig. 4.20. The total angular momentum quantum numbers F of the ground state and the excited state are given in Columns 2 and 3; theoretical heights at low laser power in Column 4; calculated heights in saturation in Column 5; The relative transition frequencies calculated from the fitted A and B parameters of the fit with the saturated relative heights are indicated in Column 7.

Peak no.	F_{gnd}	F_{exc}	a_{theo}	a_{sat}	a_{exp}	ν_{fit} (MHz)	ν_{exp} (MHz)
1	11/2	9/2	1.00	1.00	1.00(11)	0.0(4.4)	0.0(5.8)
2	9/2	7/2	0.51	0.83	0.77(8)	325.9(2.4)	324.8(5.8)
3	7/2	5/2	0.18	0.67	0.51(6)	604.2(3.8)	604.1(5.9)
4	9/2	9/2	0.32	0.83	0.81(8)	828.6(3.4)	825.1(5.8)
5	7/2	7/2	0.42	0.67	0.74(8)	984.3(2.1)	990.1(5.9)
6	5/2	5/2	0.32	0.50	0.53(7)	1104.2(4.1)	1116.2(6.1)
7a	3/2	5/2	0.33	0.33	1.08(10)	1454.9(6.9)	1480.2(5.8)
7b	5/2	7/2	0.18	0.50		1484.4(2.6)	
7c	7/2	9/2	0.06	0.67		1487.0(3.2)	

be possible to laser-cool La$^-$ with only three laser frequencies. These can be derived from a single laser by side-band generation.

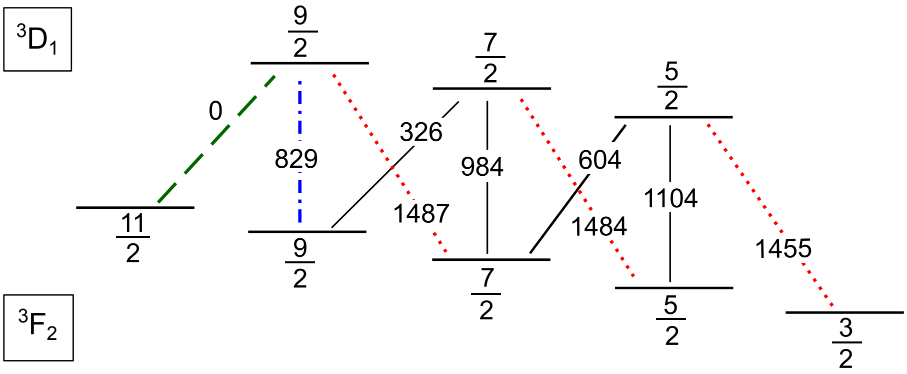

Figure 4.21: Schematic level diagram resulting from the hyperfine structure fit for the $^3F_2^e \rightarrow {}^3D_1^o$ transition. The first transition at 96.592 004(86) THz is the reference. The numbers are the relative transition frequencies in MHz. The red, green and blue colors indicate the three frequencies which are needed to re-pump all hyperfine sub-levels of the ground state.

Chapter 5

Discussion

5.1 Comparison to theoretical calculations

The experimental results for the hyperfine splitting were compared to detailed ab-initio calculations in the framework of the multiconfiguration Dirac-Fock (MCDF) method performed by S. Fritzsche. His group has developed the RATIP program to calculate the electronic structure and properties of atoms and ions [Frit2012]. The program offers tools to calculate atomic processes of open-shell atoms or ions at storage rings, in ion traps, plasmas and intense radiation fields, including photo excitation, ionization and Auger processes.

The energies of the $5d^26s^2$ $^3F_2^e$ and $5d6s^26p$ $^3D_1^o$ hyperfine structure levels in La^- were calculated by S. Fritzsche, and the energies of the hyperfine transitions between the levels were determined. This calculations showed that electronic correlations play a very significant role in La^-. As a first step, calculations in the $5d^26s^2$ and $5d6s^26p$ single-configuration were performed, but neither the splitting nor the relative intensities of the hyperfine components agreed with the experimental data. It was found that the spectroscopic observations can only be reproduced with systematically enlarged wavefunction expansions. At least single and double excitations into two further layers of correlation orbitals were needed to include a proper amount of valence–valence and core–valence correlations. For example, to identify the correct level order of the hyperfine structure of the $5d^26s^2$ $^3F_2^e \rightarrow 5d6s^26p$ $^3D_1^o$ transition, MCDF computations had to be carried out.

Due to the negative charge and the open-shell structure of La^-, convergence of all numerical results as the size of the expansions was enlarged could not be achieved in the performed calculations. In fact, from similar computations for neutral Ba and Ra [Bier2004] it is known that large-scale calculations are required already for systems with two electrons outside of closed shells. The size of the wave function expansions increases very rapidly with additional open shells. The aim of the calculations was to understand the observed hyperfine spectrum. The approximated wave functions of the low-lying $^3F_2$ and $^3D_1$ levels resulted in an excitation energy of 385.6 meV. Although the calculated excita-

Table 5.1: Calculated transition frequencies (Column 5) and for comparison the peak positions from the hyperfine structure fit (shown in Fig. 4.20); the relative transition frequencies calculated from the fitted A and B parameters are indicated in Column 6; the calculated relative transition amplitudes in saturation in Column 4. The total angular momentum quantum numbers F of the ground state (gnd) and the excited state (exc) are given in Columns 2 and 3.

Peak no.	F_{gnd}	F_{exc}	a_{theo}	ν_{theo} (MHz)	ν_{fit} (MHz)
1	11/2	9/2	12/12	0	0.0(4.4)
2	9/2	7/2	10/12	336	325.9(2.4)
3	7/2	5/2	8/12	633	604.2(3.8)
4	9/2	9/2	10/12	817	828.6(3.4)
5	7/2	7/2	8/12	1006	984.3(2.1)
6	5/2	5/2	6/12	1153	1104.2(4.1)
7a	3/2	5/2	4/12	1525	1454.9(6.9)
7b	5/2	7/2	6/12	1527	1484.4(2.6)
7c	7/2	9/2	8/12	1487	1487.0(3.2)

tion energy remained too low by about 0.2 eV compared to the experimental values, the relative splitting of the lines was reproduced, as well as the fact that three out of the nine possible hyperfine transitions lie close in frequency. Since the nuclear magnetic and electric moments are free parameters in MCDF computations, the calculated HFS splitting was scaled to the measured positions of Peaks 1 and 7c. The resulting frequencies and the values determined from the model fit in Sec. 4.2 are given in Tab. 5.1 for comparison. The calculated splitting is in good agreement with the results from the measurement, and only differs within the uncertainties for the closely clustered Peaks 7a–7c. Fig. 5.1 shows a comparison between a spectrum at 10 kV beam energy with the peak positions from the model fit in the upper pane and the frequencies of the calculation in the lower pane. The peak order from low to high frequency is very well reproduced by the calculation, confirming the peak structure found with the hyperfine fit.

5.2 Implications for laser cooling prospects

The main goal of this work is to investigate whether La$^-$ is suitable for laser cooling. For laser cooling of La$^-$, the following parameters needed to be known.

1. Exact transition frequencies for the tuning of the cooling lasers;

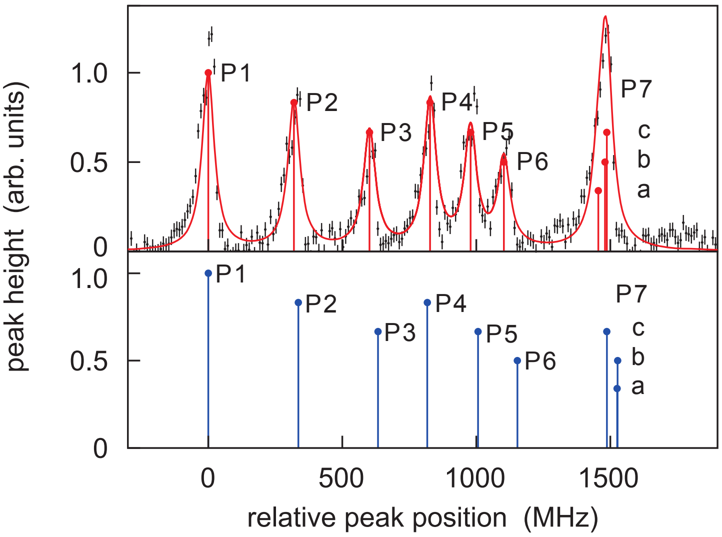

Figure 5.1: Comparison between the hyperfine spectrum determined from the data (top) and from calculations (bottom). The dots mark the peak heights, the labels the peak numbers. The data in the upper graph were recorded at 10 kV acceleration potential and 2.4 mW laser power. The solid red line is a fit with 9 Lorentzians with a width of 53.8(6) MHz.

2. Quantum numbers of the hyperfine levels to develop a cooling scheme without dark states;
3. Excitation cross sections of all hyperfine transitions for the adjustment of the power of the cooling laser;
4. Detachment cross section and electron affinity to determine losses by two-photon detachment and losses due to neutralization in collisions.

The transition frequencies and the quantum numbers have been determined, as well as the relative intensities of the transitions. However, only a rough estimate of the transition cross section is known. Knowledge of the excitation cross sections of all hyperfine transitions also allows to estimate the cooling time and the minimum temperature that can be reached. With the estimated excitation cross section of $\sigma_e \approx 10^{-12\pm1}$ cm^2 derived in Sec. 4.1, the Doppler temperature is between 8 nK and 800 nK.

The transition from the $5d^26s^2\ {}^3F_2^e$ ground state to the $5d6s^26p\ {}^3D_1^o$ excited state in La$^-$ is a dipole-allowed transition and the natural line width of the transitions is about 10 kHz. This is narrow compared to the line widths of atoms usually used for laser cooling, such as Rb and Cs, with natural line widths of about 30 MHz. This leads to longer cooling times, but also to a lower Doppler temperature for La$^-$.

In order to reach the Doppler temperature for La$^-$ starting from room temperature (295 K), on average about 2×10^5 counter propagating photons have to be scattered by a La$^-$ ion. Neglecting heating by black-body radiation, collisions with residual-gas atoms, heating by fluctuations in the trapping force and by the re-pump lasers, it would take about 10 s to cool La$^-$ to the Doppler temperature. If the excitation cross section is at the higher limit, the cooling time could be as low as 2 s. If the cross section is at the lower limit of the estimation, the cooling could take up to 3.3 min from room temperature, or 24 s if the ions are pre-cooled to the temperature of liquid helium (4.2 K). In any case, the cooling time is long compared to Mg$^+$ that can be cooled within 10 µs. But the cooling is faster than for Os$^-$, for which a cooling time of 5 min was estimated starting from 4.2 K [Warr2009]. The cooling of La$^-$ is most probably faster than the cooling of Ce$^-$, the third known laser cooling candidate among the atomic anions. Here, the low transition rate for spin-forbidden transitions would probably slow down the cooling process. Therefore, La$^-$ is a more promising candidate.

The branching ratios to different fine structure states in La$^-$ was estimated by O'Malley and Beck [O'Ma2010] to be of the order of 10^{-4}. If the cooling starts at 295 K, this would lead to a loss of all ions before the Doppler temperature is reached. To reach the Doppler temperature with a reduced number of scattering processes, pre-cooling is necessary. After pre-cooling to 4.2 K, about 2.4×10^4 photons have to be scattered.

In addition, there are losses due to two-photon detachment. However, with a detachment cross section of the order of 10^{-17} cm^2 those are expected to be small compared to losses due to dark states.

Generally, for laser cooling of anions a low background pressure is essential for the survival of the ions since the cross sections for destruction of anions in collisions with the residual-gas are large [Pegg2004, Chri1984]. Even at relatively low kinetic energies collisions can lead to excitation of anions [Pene1988]. This can not only lead to heating due to energy transfer, but also to detachment or to an additional cooling effect, if the energy is released in form of radiation.

For laser cooling inside a Penning trap a magnetic field of a fraction of a tesla is necessary to confine the ions. In strong magnetic fields the levels split according to the Paschen–Back effect, resulting in a 65-fold splitting of the transition. The level splitting for the laser cooling transition in La$^-$ in a magnetic field of 1 T is shown in Fig. 5.2. It seems convenient to use the $m_{J,\mathrm{gnd}} = 0 \rightarrow m_{J,\mathrm{exc}} = 0$ transition, which does not split, as a cooling transition. Here the intensities of eight lines add up. Unfortunately, the ions can decay to 16 levels apart from the $m_{J,\mathrm{gnd}} = 0$ state, which must be re-pumped in order to keep the ions in the cooling cycle. The splitting of the $m_{J,\mathrm{gnd}} = -1$ and $m_{J,\mathrm{gnd}} = 1$ states is given by the hyperfine structure constant A_{gnd} which is about 147 MHz. Thus the transitions lie within a frequency range of about 1200 MHz.

Two lasers with a bandwidth covering the hyperfine splitting would be needed. Alternatively, 16 frequencies need to be used for the re-pumping. Furthermore, 40% of the ions are in $m_{J,\mathrm{gnd}} = \pm 2$ sub-levels of the ground state, which are not pumped and therefore have to be removed or cooled sympathetically. These circumstances complicate laser cooling in the presence of a magnetic field. The cooling scheme in the absence of a magnetic field presented in Sec. 4.1 seems more feasible. All ions can be cooled and re-pumped with

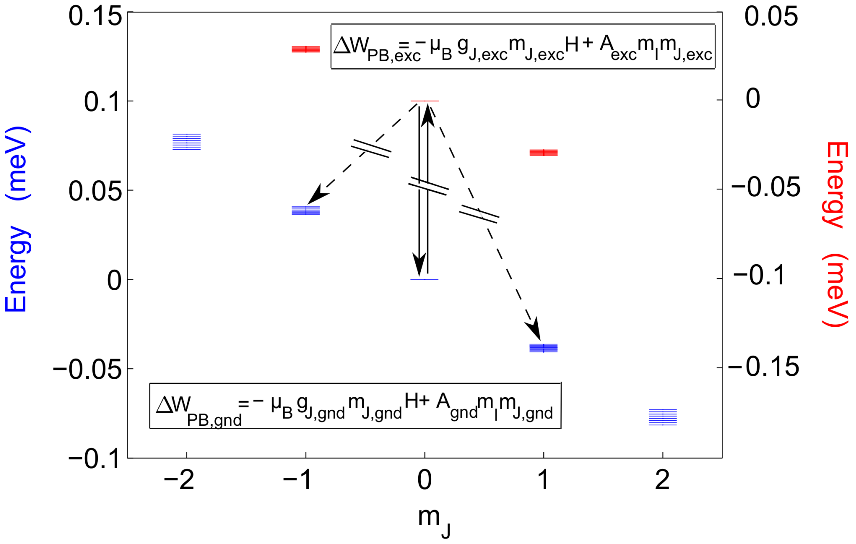

Figure 5.2: Calculated energy level diagram in the Paschen–Back regime of the $^3F_2 \rightarrow {}^3D_1$ transition in La$^-$ for a magnetic field of 1 T. The energy of the fine structure is not to scale. The solid arrows indicate the cooling cycle, the dashed arrows indicate unwanted transitions. The energy levels of the ground states are indicated in blue, the energy levels of the excited states are indicated in red with the corresponding axis on the left.

only three lasers (one with a bandwidth > 50 MHz). Trapping the ions in a electrostatic storage ring or in a Paul trap offers the possibility to trap the ions for cooling in the absence of an external magnetic field.

Alternative laser cooling candidates can be found among the molecular anions. Molecules are in general not suitable for laser cooling, because no closed cooling cycles are present. There is a rich spectrum of lower-lying rotational and vibrational states to which the excited electrons can decay. However, there are some exceptions, such as C_2^-, which have large binding energies, reducing the probability for photo-detachment, and a smaller mass than La$^-$, reducing the momentum to be cooled. Suitable cooling cycles have been identified in molecular anions [Yzom2015], which makes them interesting competitors to La$^-$.

Chapter 6

Summary

Negative ions are of interest in many different fields of physics, including plasma physics, biophysics, atmospheric science and astrophysics. Until today, there is no method to cool negative ions much below temperatures of the surrounding environment. Laser cooling of negative ions could overcome that restriction and clear the way for precision measurements to test theoretical predictions. There are only three known anion species, namely Os^-, Ce^-, and La^-, in which bound–bound electric-dipole transitions have been observed. In this work the suitability of La^- for laser cooling applications has been investigated.

For this purpose, high-resolution laser spectroscopy on a beam of La^- ions was performed in a collinear laser photodetachment spectroscopy setup at the Max Planck Institute for Nuclear Physics (MPIK). The hyperfine structure of the potential laser cooling transition from the $5\mathrm{d}^2 6\mathrm{s}^2\ {}^3\mathrm{F}^e_2$ ground state to the $5\mathrm{d}6\mathrm{s}^2 6\mathrm{p}\ {}^3\mathrm{D}^o_1$ excited state was elucidated. Seven out of the nine expected transition peaks in the hyperfine spectrum were resolved and the transition frequencies in the rest frame of the ions were determined with a relative resolution better than 6 MHz and an absolute precision of 86 MHz.

The observed transition resonances were unambiguously assigned to allowed transitions between the hyperfine structure levels of the ground and excited states by a model fit. The hyperfine structure constants A and B were determined for the ${}^3\mathrm{F}^e_2$ and ${}^3\mathrm{D}^o_1$ states. Furthermore, the fit reveals that the hyperfine transition resonances with $\Delta F = +1$ are closely clustered and could not be resolved. The relative peak heights in the observed spectra indicate that the transitions are saturated even at 45 Wm^{-2}, the lowest laser intensity used in this experiment.

Furthermore, the experimental results lead to an energy level diagram which suggests that laser cooling of La^- should be possible with only three lasers. A rough estimate of the transition cross section was made by evaluating the fraction of ions excited inside the electrostatic deflector. The cross section of the strongest transition was found to be of the order of $10^{-12\pm1}$ cm^{-2}. This corresponds to an Einstein coefficient A_{21} between 2×10^3 and 2×10^5 s^{-1}. The estimated cross section gives a rough impression on the performance of La^- in laser cooling applications. The Doppler limit is expected to be between $T_{\mathrm{D}} = 8$ nK and 800 nK and can be reached within a cooling time of 0.2 to 24 s depending on the scattering rate, when starting from 4.2 K. However, large losses due to the decay to different fine structure states are expected. The results confirm that La$^-$ a promising candidate for Doppler laser cooling among the atomic anions.

In order to judge whether La$^-$ is as excellent for laser cooling as predicted, the absolute transition rates need to be determined precisely. Other important parameters, such as the branching ratios to other fine structure states and the detachment cross section are only known from theoretical calculations and need to be measured to estimate potential losses. These open questions can be addressed in future experiments.

Appendix A

Appendix

A.1 Laser system tuning characteristics

The laser system consists of a seed laser, a fiber amplifier, the OPO system and the reference laser. A schematic drawing of the laser system is shown in Fig. A.1.

The following tuning mechanisms are available for the idler wavelength of the Argos OPO laser system

- Changing the poling period of the non-linear crystal via translation of the crystal (with several poling regions)
- Adjustment of the intra-cavity etalon angle
- Piezo tuning of the cavity for the signal
- Temperature tuning of the OPO crystal
- Piezo strain of the fiber of the seed laser

The crystal translation is used to tune the wavelength coarsely in steps of 10–20 nm. The etalon angle can be used to tune the laser with an intermediate step size of about 1 nm over the free spectral range of about 400 GHz. Temperature tuning is generally restricted to relatively small wavelength ranges. The temperature can be used for tuning, but it is recommended to keep it constant and use the other tuning mechanisms for better wavelength stability. The seed source tuning is used for the fine tuning. In this experiment, the scanning was done by applying a triangular voltage to the piezo of the seed source. A section of a typical scan of the idler frequency with the normalized count rate is shown in Fig. A.2.

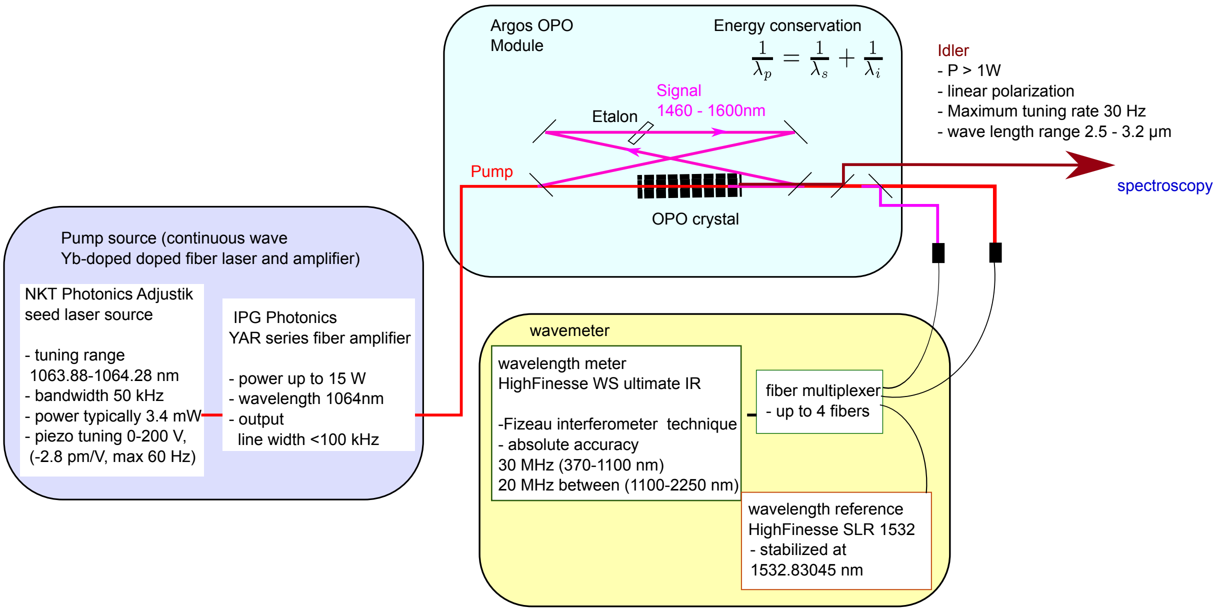

Figure A.1: The laser beam is generated in the seed source and amplified in a fiber amplifier. In the OPO crystal the photons from the pump beam are down-converted into two photons with lower energies. Only the signal wavelength is resonant in the cavity, while idler exits on a single pass without internal reflection. The wavelengths of the signal and the pump beams are measured with a wavemeter. For the calibration of the wavemeter a stabilized laser is used.

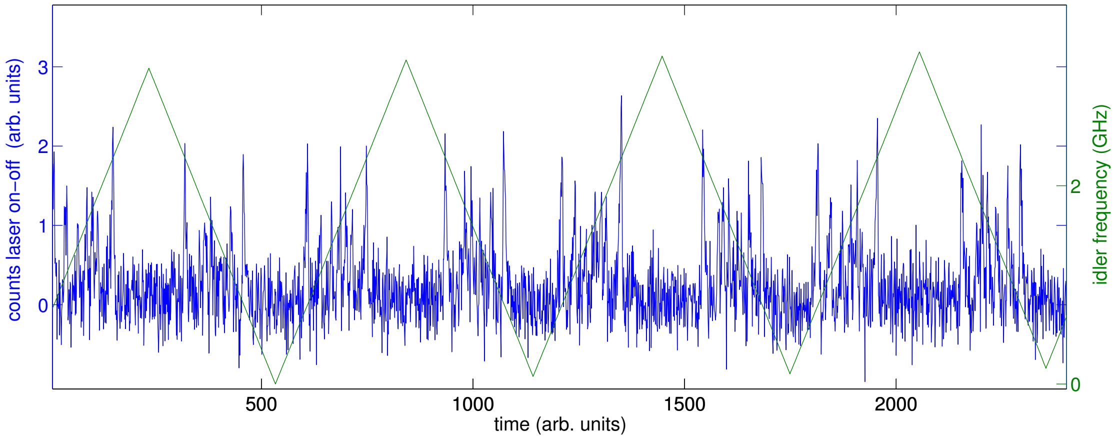

Figure A.2: Scanning of the idler frequency (green line) and normalized count rate of the neutrals with subtracted backgrounds and 10 MHz bin size and 5 mW excitation power. The resonance peaks were recorded in both scanning directions.

A.2 Ion source characteristics

The performance of the beam line and the ion source had a strong impact on the quality of the results. In order to obtain a stable ion beam, all parts must be carefully grounded. The same ground must be used for the extraction electrode, the power supplies of the source and the beamline. Further, it was found that a cooling circuit between the target, the extraction electrode and the chamber of the source helped to stabilize the current, as shown in Fig. A.3. The water acts as a connection to ground with a high resistance. Due to the high voltages, the copper connectors of the water pipes are slowly dissolved by electrolysis and have to be checked regularly.

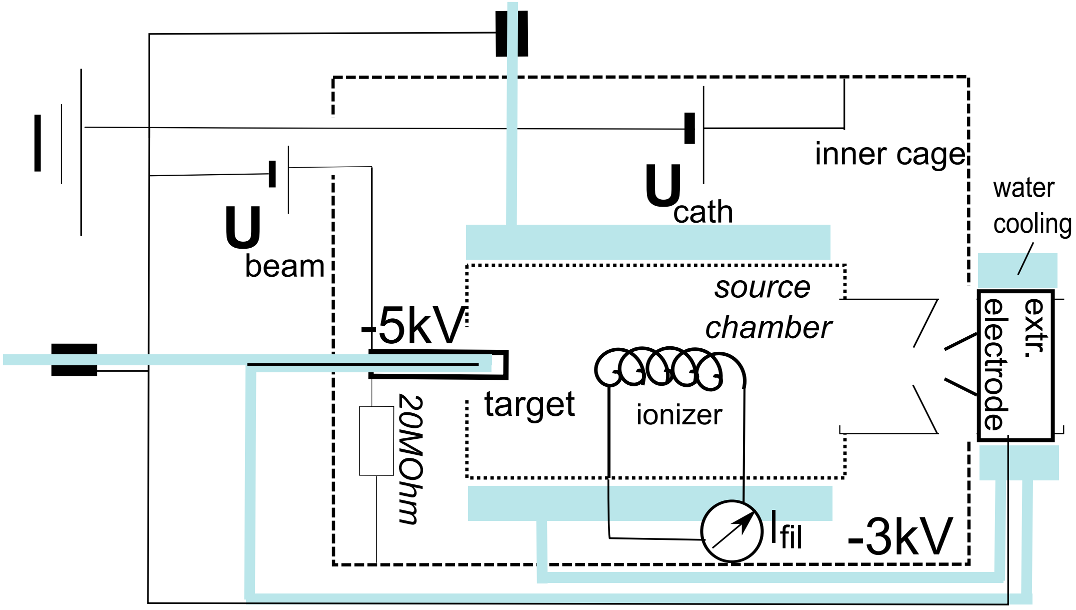

Figure A.3: Circuits of the source. The light blue color marks the water cooling circuit for the target, around the source chamber and the extraction electrode. The cooling water is grounded in three positions, before the target, on the extraction electrode and after the source chamber. Cs is thermally ionized on the hot ionizer and sputtered on the target. The negative ions are accelerated by the acceleration potential which is applied between the target and the extraction electrode. The inner cage, including the case of the source and the ionizer are at 3 kV. Thus the sputtering potential between the ionizer and the target is 2 kV for an extraction potential of 5 kV.

Mass spectra

The source produces not only ^{139}La$^-$ but also negative ions of other elements which are present in the source, such as oxygen from the residual-gas, Cs, the components of the container for the target, lanthanum composites like LaH, LaH_2, LaH_3, LaH_4 and oxides LaO and LaO_2. The produced anions were mass separated in a dipole magnet. A mass spectrum is shown in Fig. A.4. The spectrum originates from a lanthanum metal target in a container made of copper. In contrast, for the mass spectrum shown in Fig. 3.4 a stainless steel container was used with the target material extruding out approximately 1 mm. This strongly reduced the content of contaminants in the La$^-$ beam. However, the hydrates of lanthanum are hard to separate, because their masses are close to the mass of La. A detailed scan of the La peak is shown in Fig. A.5 (top).

For the spectroscopy a pure beam of La$^-$ without hydrates would be ideal. This is not possible to obtain with the current mass separation. In the spectroscopy experiment the neutralized particles are counted. If the laser is resonant with a transition the photo detachment is strongly enhanced for La$^-$, but not for the hydrates as shown in Fig. A.5 (bottom). The resonant laser is selecting La$^-$. Even if there is a large fraction of hydrates in the beam the detected neutrals are mainly La atoms.

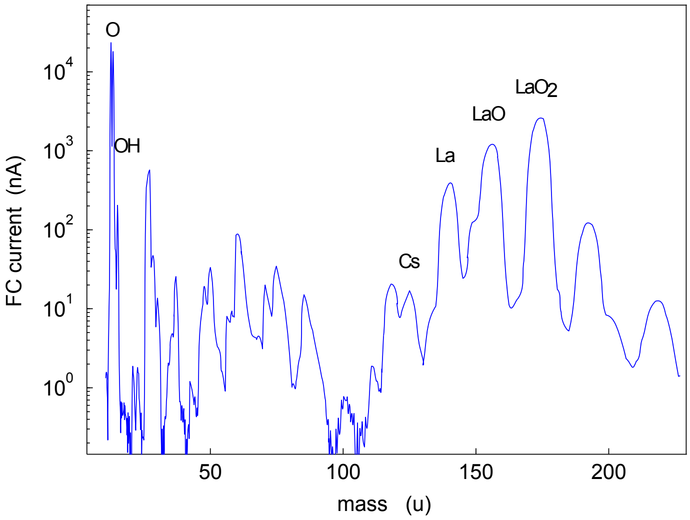

Figure A.4: Mass spectrum from the source with a La target in a Cu container showing a spectrum of contaminants. The largest fraction of the ion beam is typically O$^-$. There is also a large amount of LaO and LaO_2. These are separated from La by the mass separator.

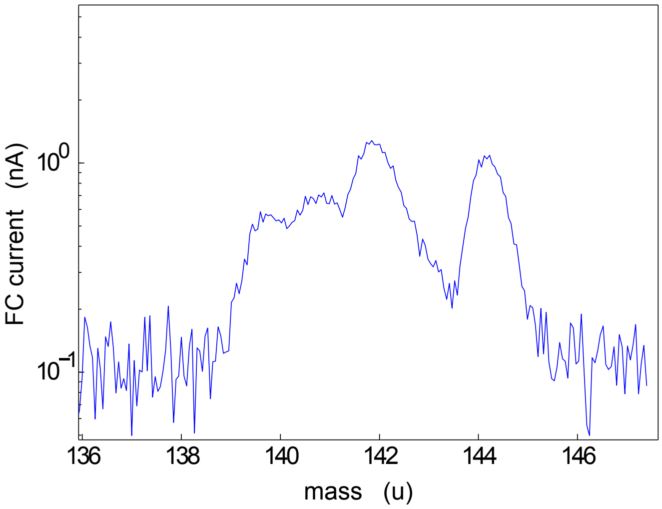

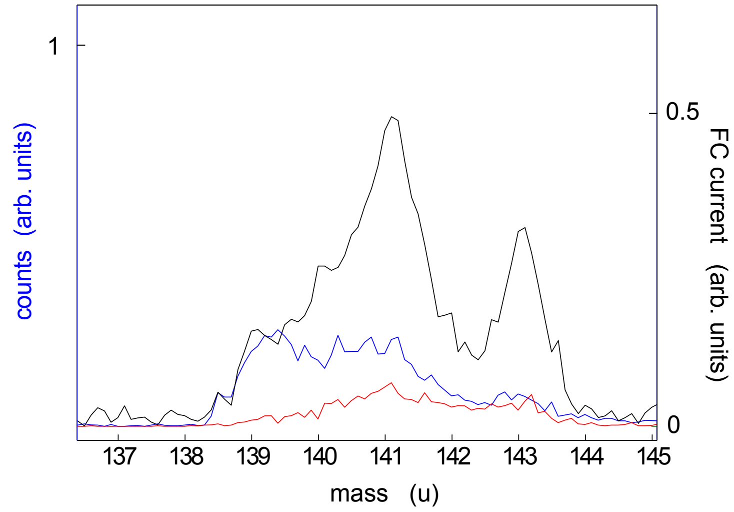

Figure A.5: (Top) Lanthanum is the leftmost peak, the partially resolved peaks to the right originate from the hydrides (LaH, LaH_2, LaH_3, LaH_4). The hydrides are not completely resolved by the dipole magnet. (Bottom) Detachment signal for La and the hydrates. Laser interacting with the ions (blue line) and laser blocked (red line). The Faraday cup current (black line) indicates the amount of ions in the beam. With the laser a strong enhancement of the detachment of La^- is observed, but not for the hydrates.

A.3 Ion beam line simulations

A.3.1 Transmission for different masses

To test the efficiency of the mass separation a simulation with particles that have different masses was launched. The same number of ions with masses 136, 137, 138, 139, 140, 141, 142 u were simulated for one set of voltages and counted in the end of the spectroscopy region. A histogram of the transmitted ions is shown in Fig. A.3.1. The histogram shows that the transmission is the highest for La^- with mass 139 u. This is expected, because the settings were optimized on La^-. Ions with masses 140 u (LaH) and 141 u (LaH_2) are also transmitted, whereas LaH_3 is filtered out efficiently. The simulation suggests that there is some background due to LaH and LaH_2.

A.3.2 Angular spread and ion optics

In the simulation the collimation angle of the ions from the source was changed in the range from 0°–3°. The divergence of the ions does not change the resonance frequency and has only a small influence on the line width, as shown in Fig. A.3.2 (left). Ions with large divergence are blocked by the diaphragms and cannot reach the detector, as shown in Fig. A.3.2 (right). The changes in the width of the absorbed line seem to be of statistical nature, since for 1.0 ° divergence more ions reach the detector and the absorption is more narrow than for 1.5 °.

In the simulation, changes of the voltages of the einzel lenses and quadrupole lenses from the optimal values lead to a stronger divergence of the beam and hence more ions are stopped on the diaphragms, but the frequency is not shifted.

In order to test the influence of voltage fluctuations in the source, the initial kinetic energy of the ions was set to a Gaussian distribution with varying standard deviation. As the standard deviation gets larger the frequency spread of the ions due to the Doppler effect gets larger, but no systematic shift is observed, as shown in Fig. A.9 on the left.

To test the influence of the magnet current simulations with various magnet currents were performed. The variable for the magnetic field strength in the simulations, does not directly correspond to a current in the magnet. The value for the variable describing the magnetic field strength was about 288. A variation of 0.7% around optimal value did not lead to a systematic shift of the frequency. For even larger changes of the magnet current the ions are stopped in the magnet or on the apertures behind.

A.3.3 Electrostatic deflector

The negative ions are guided into the spectrometer section by an electrostatic deflector, which was developed by Kreckel et al. [Krec2010]. The deflector has been modified with apertures to allow the laser passing through straight. The shape of the apertures is the

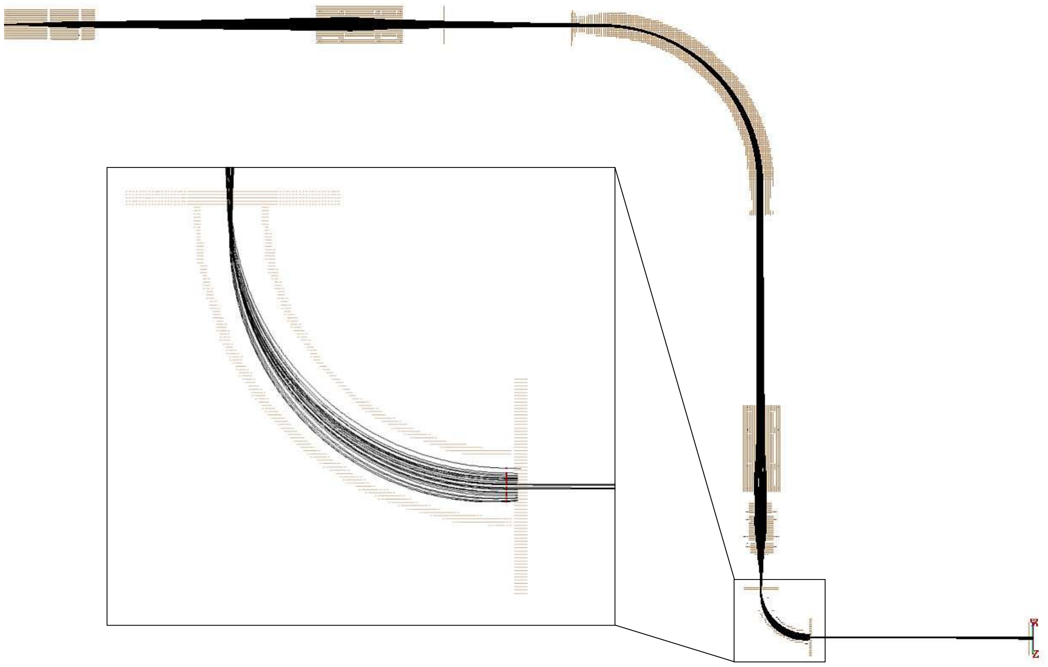

Figure A.6: Beamline simulated with SIMION. The brown color indicates the electrodes. The black lines are the trajectories of the ions. 500 000 ions were simulated with a kinetic energy of 6000 eV, with 6 V standard deviation. The inset shows the trajectories of the ions inside the deflector.

projection of a 7.5 mm hole on the circular electrode. One aperture is for the spectroscopy laser, another one is at 90° with respect to the first aperture. The second aperture was used for the beam diagnostics and the alignment of the deflector in the cross. The apertures in the electrode make it necessary to apply higher voltages than for a deflector without apertures, where one quarter of the beam energy is applied on the outer electrode and one eighth on the inner electrode. If well adjusted voltages are applied, the trajectories of the ions are not affected by the apertures, as shown with SIMION simulations, see inset of Fig. A.3.

A SimIon simulation with 500 000 La^- was launched. The complete beamline was simulated with an acceleration potential of 6000 V with 6 V standard deviation and an angular spread of the ions of 2°. The velocity distribution of the ions inside the deflector was recorded at 13 positions in 2.5 mm distances. Those ions were selected which were in the laser beam and which pass through the aperture in the end plate of the deflector. The frequency distribution was calculated using the Doppler shift for the velocities obtained from the fit. The result was a 3 GHz long frequency distribution towards lower frequencies for a collinear setup, as shown in Fig. 4.9.

Behind the deflector a symmetric velocity distribution is expected, because the ions travel through the drift tube in the direction of the laser beam. This was confirmed in a SimIon

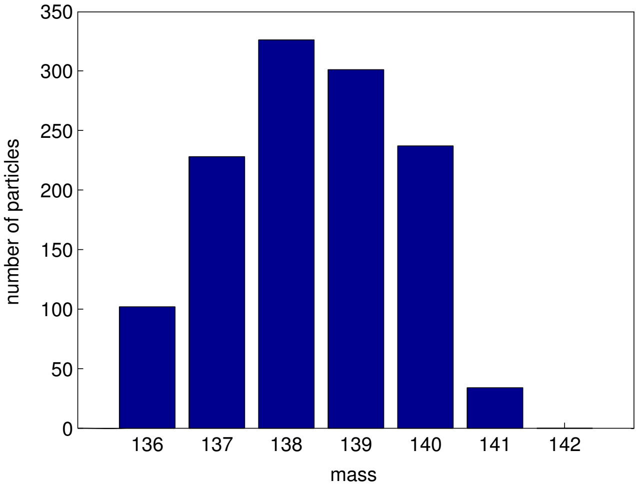

Figure A.7: Simulated mass spectrum on the detector. The same number of ions with masses 136, 137, 138, 139, 140, 141, 142 u were simulated and counted after they had passed through the beamline and impinged on the detector. The transmission is the highest for ions with mass La$^-$ (139 u). Ions with 142 u were filtered out completely.

simulation with 500 000 ions with the same settings as described above. The result is a approximately Gaussian frequency distribution with $\sim$ 50 MHz FWHM. However, if the beam is miss aligned or the voltages on the deflector electrodes are asymmetric the mean velocity is smaller than the original 6 keV and the distribution is be asymmetric, as shown in Fig. A.3.3. Such an asymmetric absorption spectrum towards larger Doppler shifts was observed in the spectra in Fig. 4.10 (upper pane on the left).

The analytic calculation is based on the Fig. 4.8 (left). The angle $\alpha_{\max}$ at which the ions start to interact with the laser beam was calculated using the geometry of the deflector (radius of the trajectory R=158 mm, diameter of the aperture R_a=7.5 mm).

$$\alpha_{\max} = \arccos\left(1 - \frac{R_a}{2R}\right)\frac{180}{\pi}. \tag{A.1}$$

The distance d_0 from the aperture at the exit of the deflector is

$$d_0 = R\sin\left(\frac{\alpha_{\max}}{180}\pi\right). \tag{A.2}$$

In order to determine the absorption spectrum, the velocity of the particles in laser direction is needed. It is given by

$$v = v_0\cos\left(\frac{\alpha}{180}\pi\right), \tag{A.3}$$

where v_0 is the absolute velocity of the ions and α is the angle inside the deflector.

At $\alpha_{\max}$ not the ion beam is only partially overlapping with the laser beam. Since $\alpha_{\max} \approx$ 12.5°, the part of the ions which is inside the interaction region is approximated with a

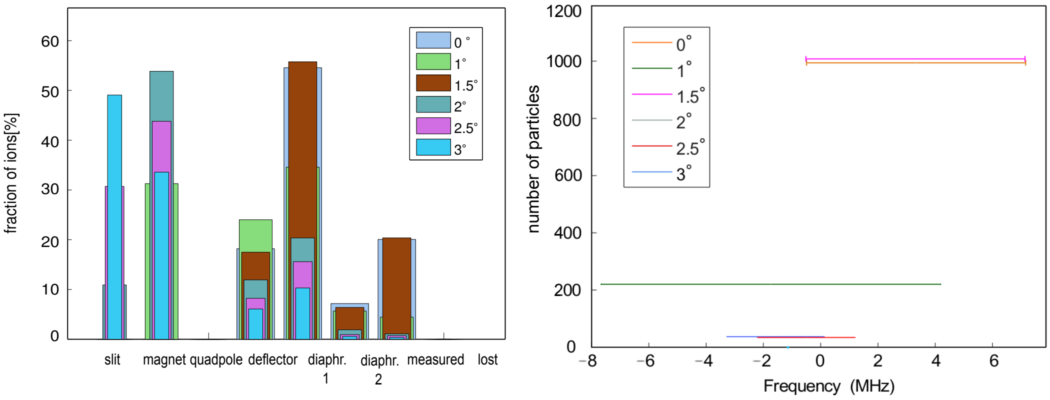

Figure A.8: Fraction of ions stopped on the aperture of the indicated device (left). The order of the apertures corresponds to the sequence in which the ions pass through. Ions with large divergence are mainly stopped in the first parts of the beamline. (Right) The height of the lines indicate the number of ions that reached the detector. The lines indicate the standard deviation of the mean frequency absorbed by the ions. The frequency shift caused by the divergence of the ions is compatible with zero within the uncertainty.

triangle, as seen from the top. With this approximation the fraction of interacting ions I becomes

$$I = I_0 \left[1 - \frac{R \sin\left(\frac{\alpha}{180}\pi\right)}{d0} \right], \tag{A.4}$$

where I_0 is the total number of ions.

These considerations leads to an analytical fit function for the tail.

$$\begin{aligned} F(f) = {} & k\Theta_1 \mathrm{Re}\left(1 - \frac{R \sin\left\{ \arccos\left[\left(1 - \frac{f}{b_1 + f_{\mathrm{bias}}} \right) \frac{c}{v_0} + 1 \right] \right\}}{d_0} \right) \Theta_2 \\ & + \left[\Theta_3 \left(\frac{a_1 + k}{a_1} - 1 \right) + 1 \right] \times \frac{a_1 c_0^2}{(f - (b_1 + f_{\mathrm{bias}}))^2 + c_0^2} \\ & + \frac{o_1 c_0^2}{(f - (b_1 + f_{\mathrm{bias}}))^2 + c_0^2}, \end{aligned} \tag{A.5}$$

where f is the frequency, b_1 is the fit parameter for the transition frequency, k is the scaling parameter for the tail, a_1 is the scaling parameter for the Lorentzian merged to the tail, c_0 is the half width at full maximum of the Lorentzians, o_1 is the scaling parameter of the additional Lorentzian for the peak; Θ_1 is the Heavyside function that ensures that the tail only extends in one direction up to the center of the peak; Θ_2 prevents negative count rates and Θ_3 is for merging the second half of the Lorentzian peak with the part under which the tail is. The fit function is plotted in Fig. A.11.

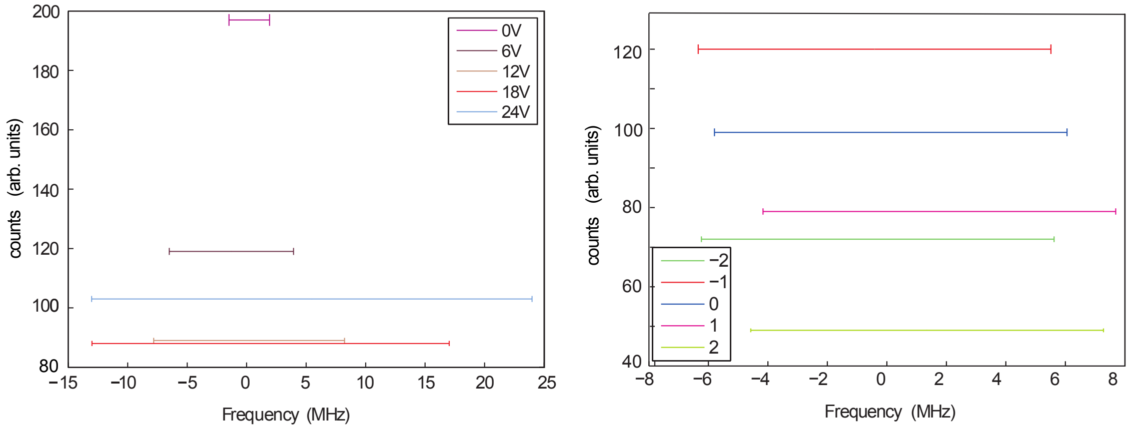

Figure A.9: (Left) The lines indicate the standard deviation of the mean frequency absorbed by the ions, the heights of the ions indicate the numbers of ions that reached the detector. Fluctuations in the acceleration voltages of the source were simulated by a Gaussian distribution of the kinetic energy of the ions. The velocities in beam direction at the position of the detector was used to calculate the absorption spectrum. The frequency distribution becomes broader, but the mean value is not systematically shifted. (Right) The influence of fluctuations in the current of the mass separating magnet were simulated by performing several simulations with different currents in the magnet around a value of 288, the numbers -2–2 indicate the deviation from that value. The mean frequency stays constant to good approximation.

Linear behaviour of the detachment rate with increasing laser power

The detachment cross rate increased linearly with the power of the detachment laser. For the measurement shown in Fig. A.13 the excitation laser power was kept constant at 8.8 mW. The slope of the linear fit is $a = 0.0414(47)$ mW^{-1}. The linear behaviour shows, that the excited state is not depleted. In the case of depletion of the excited state, a non-linear saturating behavior would be expected.

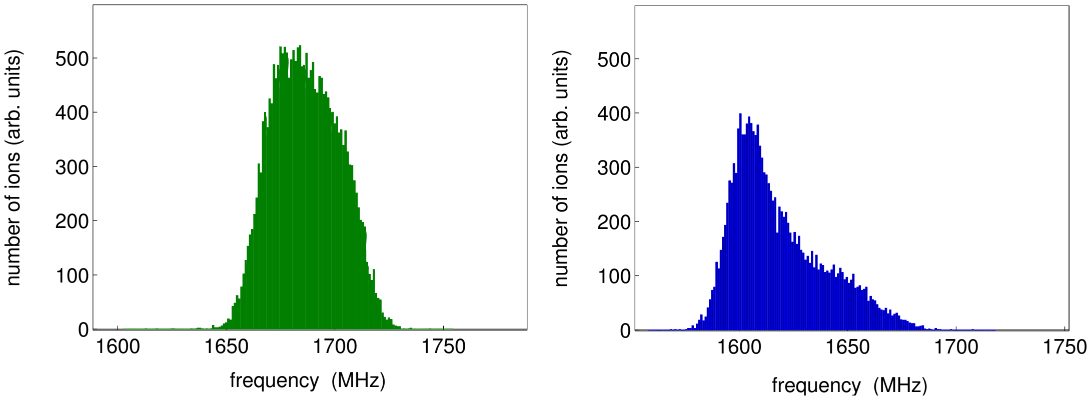

Figure A.10: Absorbed frequency distribution behind the deflector. The velocity distribution at a position behind the deflector was simulated with SimIon and the absorption spectrum was calculated. (Left) absorption spectrum of ion beam with optimized deflector settings; (right) absorption spectrum with too low voltages applied on the deflector plates resulting in an absorption spectrum with a peak at smaller Doppler shift (due to the lower beam energy) and an asymmetric peak shape with a positive skew towards larger Doppler shift.

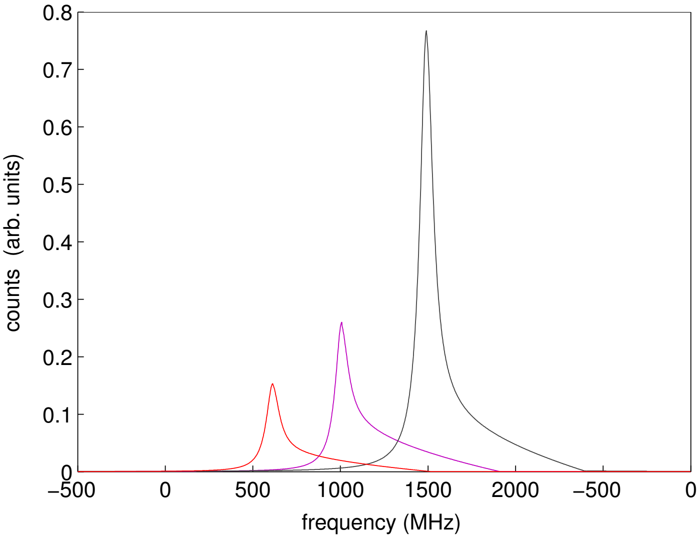

Figure A.11: Lorentzian shaped resonance with calculated tail according to Eq. (A.5). The curves have different scales for the tail and the peak. The curve is composed of a Lorentzian peak and a tail. To combine the two parts smoothly the height of the first part of the Lorentzian, where no tail is added, was scaled up to fit the height of the sum of the tail and the peak.

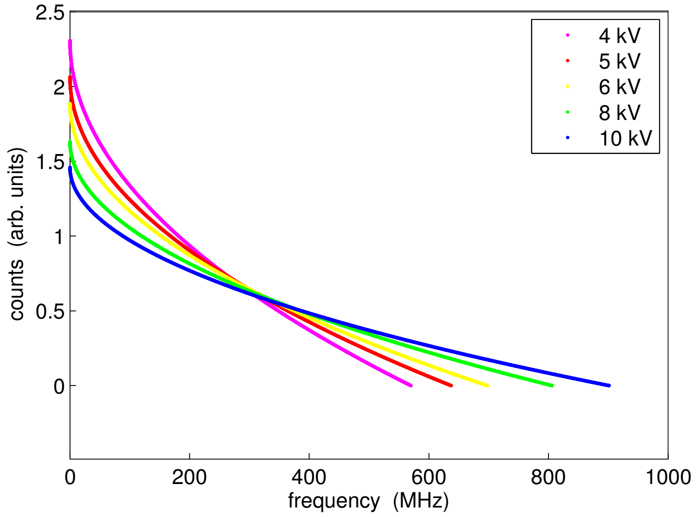

Figure A.12: Calculated length of the tail for various beam energies. In the calculation only the geometrical effect of the radial velocity component was taken into account. For higher beam energy the tail is longer.

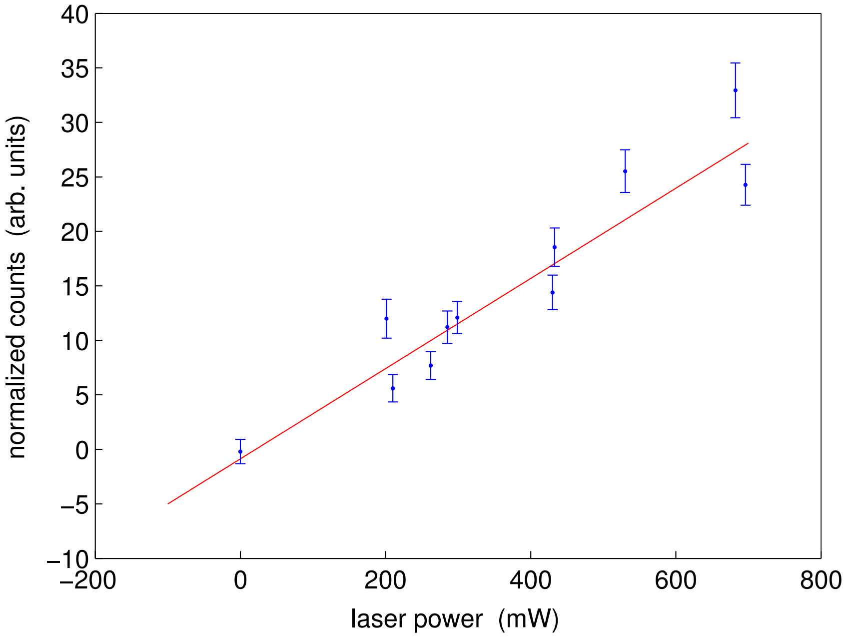

Figure A.13: The detachment power was varied in a range from 100 mW to 600 mW. The count rate is to good approximation linearly increasing with the detachment laser power. The slope is $a = 0.0414(47)\ \mathrm{mW}^{-1}$; the slightly negative offset $c_0 = -0.9(1.6)$ is compatible to zero.

A.4 Spectrum recorded at 5–10 keV beam energy

The spectrum was recorded only in one direction at 4 and 9 keV beam energy and therefore these measurements were not taken into account.

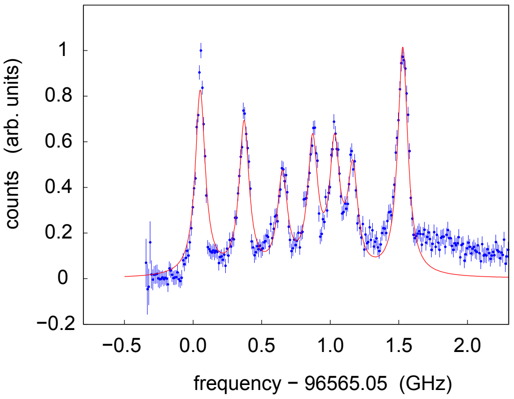

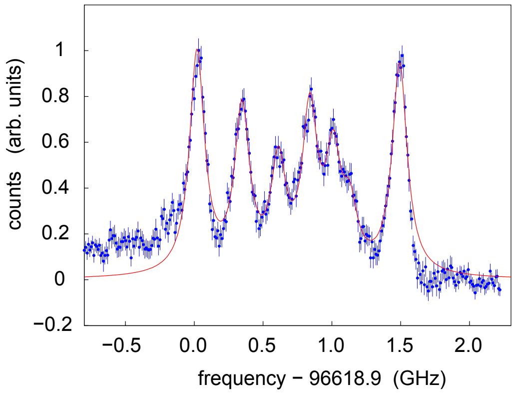

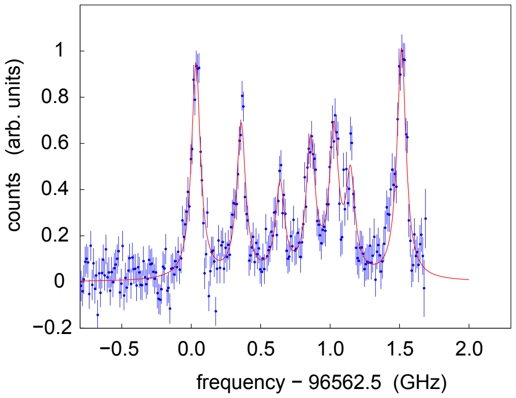

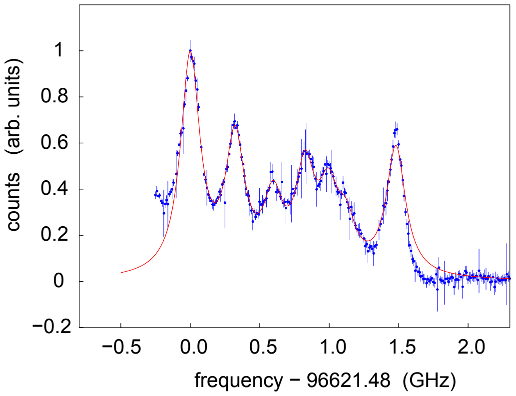

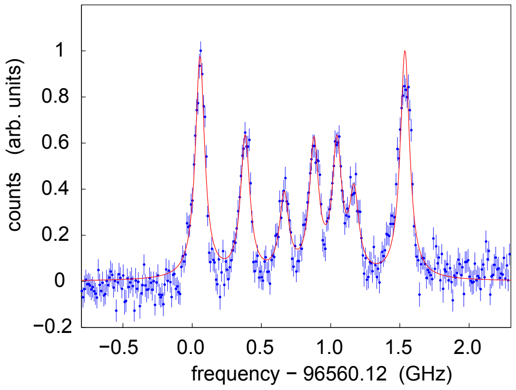

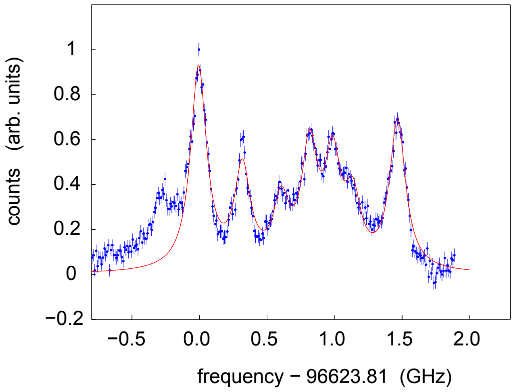

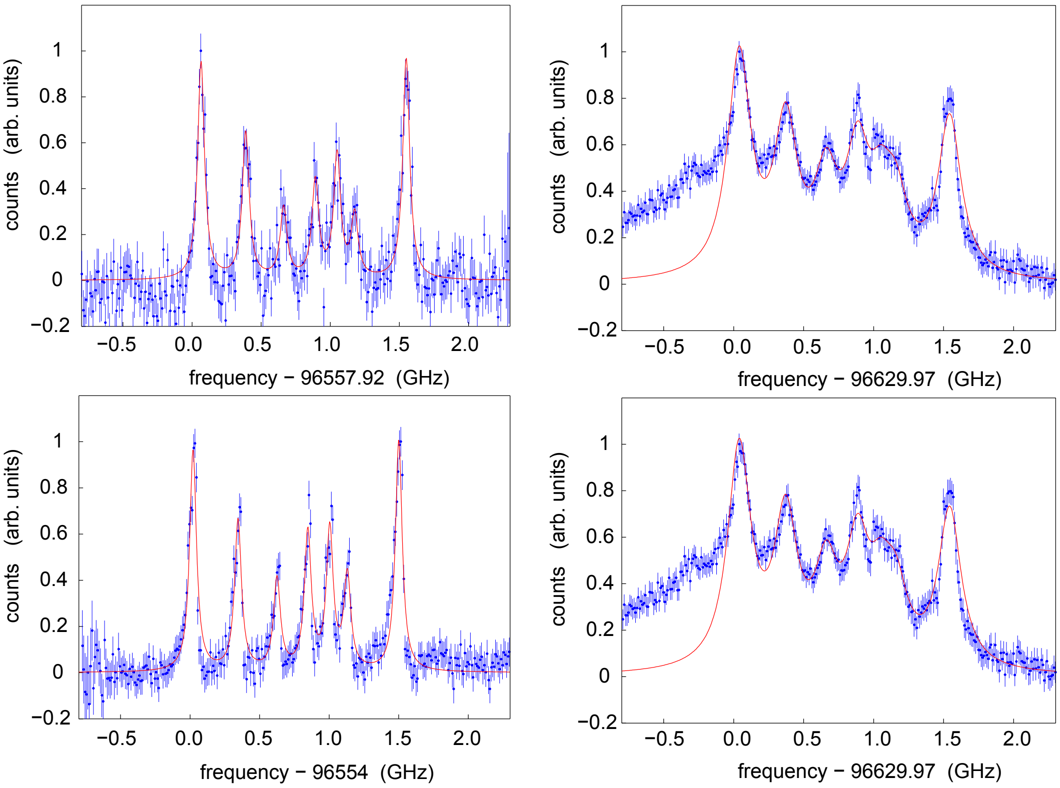

Figure A.14: Resonance in La$^-$ measured in a anti-collinear setup (left) and collinear setup (right). The beam energy is from top to the bottom row 5 keV, 6 keV, 7 keV, 8 keV and 10 keV. The laser power was 2.4 mW to 60 mW. The blue dots are the normalized counts. The fitted curve is the sum of seven Lorentzians. The peak heights, the peak positions and the (forced identical) width are free fit parameters.

A.4.1 Comparison of the rest frame frequencies

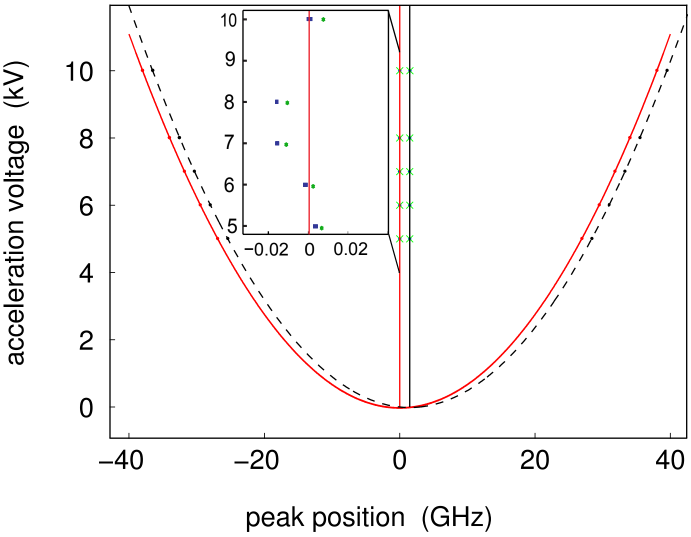

Figure A.15: The red and black line indicate the parabola fit to the measured Doppler shifted frequencies of Peak 1 and Peak 7, respectively. The center frequencies of the parabolas are indicated by the vertical lines in the same color. The green crosses are the arithmetic averages of the collinear and anticollinear measurements, the blue dots are the geometric means with errorbars. The inset shows that the geometric means are systematically at lower frequencies than the arithmetic means. The values scatter strongly. The statistical uncertainties are about a factor 10 smaller than the standard deviation. This is most probably due to systematic errors, such as slightly different beam energies for the two measurements in the collinear and anticollinear configuration. The average value of the geometric averages is about 10 MHz away from the center of the parabolas.

The fitted frequency offsets of the individual peaks were plotted as a function of the acceleration potential, as shown in Fig. A.15. The rest frame frequencies were determined by taking the geometrical mean of the collinear and anticollinear measurements. If there was more than one measurement at the same beam energy for one configuration, the weighted mean of the frequencies was determined. The geometric averages differ from the arithmetic averages. Both averages scatter strongly most probably due to systematic effects, such as slightly different beam energies for the collinear and anticollinear measurement.

A.4.2 Additional records of the hyperfine spectrum

For the last power broadened spectrum the tail was not in the scanning range and therefore not measured. The missing tail behind Peak 7 leads to an underestimation of the tail in the fit, as observed in the plot of the heights of the tails, shown in Fig. 4.11 and the plot of the ratios between the area below the peak and the tail shown in Tab. 4.3, Fig. 4.13

and Fig. 4.14.

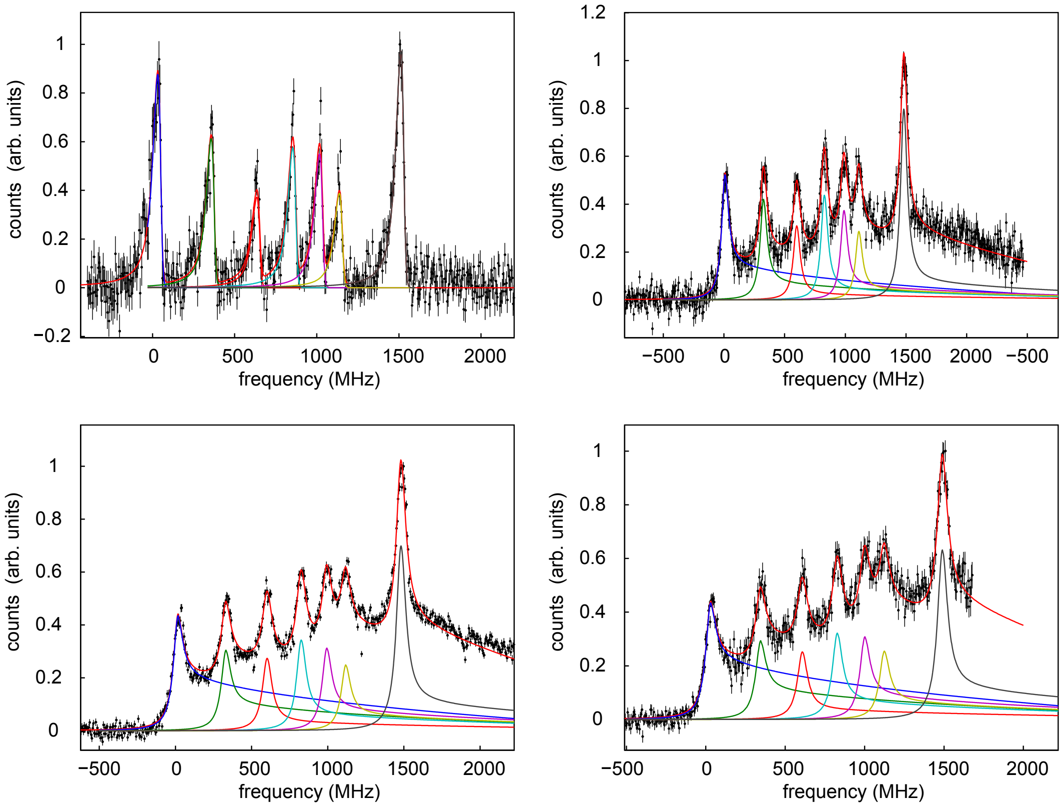

Figure A.16: Additional records of the power broadening measurement at a beam energy of 10 keV and excitation laser power of 5.3 mW (upper pane on the left), 28 mW (upper pane on the right), 44 mW (lower pane on the left) and 64 mW (lower pane on the right). Unfortunately, for the measurement at 64 mW the tail was not inside the scanning range.

List of Figures

List of Tables

Bibliography

[Agún2008] M. Agúndez, J. Cernicharo, M. Guélin, M. Gerin, M. C. McCarthy, and P. Thaddeus. *Search for anions in molecular sources: C_4H^- detection in L1527.* Astron. Astrophys. **478**, L19 (2008).

[Alto1996] G. D. Alton and G. D. Mills. *A high efficiency positive (negative) surface ionization source for radioactive ion beam.* Rev. Sci. Instrum. **67**, 1630 (1996).

[Ande1999] T. Andersen, H. K. Haugen, and H. Hotop. *Binding Energies in Atomic Negative Ions: III.* J. Phys. Chem. Ref. Data **28**, 1511 (1999).

[Ande2004] T. Andersen. *Atomic negative ions: structure, dynamics and collisions.* Phys. Rep. **394**, 157 (2004).

[Ande2013] P. Andersson, M. Martschini, A. Priller, P. Steier, R. Golser, and O. Forstner. *Spectroscopic analysis of the blue light emitted from Middleton type cesium sputter negative ion sources.* Nuclear Instruments and Methods in Physics Research B **295**, 55 (2013).

[Ange1976] B. M. Angelov. *Electron affinities of the lanthanides.* Chem. Phys. Lett. **43**, 368 (1976).

[Basa2009] G. Basar, G. Basar, and S. Kröger. *High resolution measurements of the hyperfine structure of atomic Lanthanum for energetically low lying levels of odd parity.* Opt. Commun. **282**, 562 (2009).

[Bass1977] F. Bassani, J. J. Forney, and A. Quattropani. *Choice of Gauge in Two-Photon Transitions: $1s-2s$ Transition in Atomic Hydrogen.* Phys. Rev. Lett. **39**, 1070 (1977).

[Benn1973] A. L. Bennani, J. Pebay, and B. Nguyen. *Measurement of the absolute electron detection efficiency of a channel multiplier (channeltron).* J. Phys. E **6**(11), 1077 (1973).

[Bevi1992] P. R. Bevington and D. Robinson. *Data reduction and error analysis for the physical sciences.* McGrawn-Hill, Inc., 2nd edition (1992).

[Bier2004] J. Bieroń, C. F. Fischer, S. Fritzsche, and K. Pachucki. *Lifetime and hyperfine structure of the $^3D_2$ state of radium.* J. Phys. B **37**, L305 (2004).

[Bilo2000] R. C. Bilodeau and H. K. Haugen. *Experimental Studies of Os$^-$: Observation of a Bound-Bound Electric Dipole Transition in an Atomic Negative Ion.* Phys. Rev. Lett. **85**, 534 (2000).

[Blon1994] C. Blondel. *Recionsexperimental achievements with negative ions.* Phys. Scr. **T58**, 31 (1994).

[Boll1988] J. J. Bollinger, L. R. Brewer, J. C. Bergquist, W. M. Itano, D. J. Larsont, S. L. Gilbert, and D. J. Wineland. *Ion Trapping Techniques: Laser Cooling and Sympathetic Cooling in Intense Position Beams.* World Scientific, Singapore (1988).

[Bran1999] S. Brandt. *Datenanalyse.* Spektrum Akademischer Verlag, 4th edition (1999).

[Chri1984] L. G. Christophorou. *Electron-molecule Interactions and Their Applications: v. 1.* Academic Press Inc (1984).

[Covi1998] A. M. Covington, D. Calabrese, J. S. Tompson, and T. J. Kvale. *Measurement of the electron affinity of lanthanum.* J. Phys. B **31**, L855 (1998).

[Dali1985] J. Dalibard and C. Cohen-Tannoudji. *Dressed-atom approach to atomic motion in laser light: the dipole force revisited.* J. Opt. Soc. Am. B **2**, 1707 (1985).

[Davi2002] V. T. Davis and J. S. Thompson. *Measurement of the Electron Affinity of Cerium.* Phys. Rev. Lett. **88**, 073003 (2002).

[Degl2009] E. L. Degl'Innocenti. *Atomic Spectroscopy and Radiative Processes.* Springer-Verlag Italia (2009).

[Demt1981a] W. Demtröder. *Laser Spectroscopy: Basic Principles*, volume **1**. Springer Verlag Berlin Heidelberg, 3rd edition (1981).

[Demt1981b] W. Demtröder. *Laser Spectroscopy: Experimental techniques*, volume **2**. Springer Verlag Berlin Heidelberg, 4th edition (1981).

[D'Ur2003] B. D'Urso, B. Odom, and G. Gabrielse. *Feedback Cooling of a One-Electron Oscillator.* Phys. Rev. Lett. **90**, 043001 (2003).

[Feig1981] C. S. Feigerle, R. R. Corderman, S. V. Bobashev, and W. C. Lineberger. *Binding energies and structure of transition metal negative ions.* J. Chem. Phys. **74**, 1580 (1981).

[Fisc2010] A. Fischer, C. Canali, U. Warring, A. Kellerbauer, and S. Fritzsche. *First Optical Hyperfine Structure Measurement in an Atomic Anion.* Phys. Rev. Lett. **104**, 073004 (2010).

[Foot2005] C. J. Foot. *Atomic Physics.* Oxford University Press (2005).

[Frit2012] S. Fritzsche. *The Ratip program for relativistic calculations of atomic transition, ionization and recombination properties.* Comput. Phys. Commun. **183**, 1525 (2012).

[Gupt2007] H. Gupta, S. Brünken, F. Tamassia, C. A. Gottlieb, M. C. McCarthy, and P. Thaddeus. *Rotational Spectra of the Carbon Chain Negative Ions* C_4H^- *and* C_8H^-. Astrophys. J. Lett. **655**, L57 (2007).

[Hä1975] T. W. Hänsch and A. L. Schawlow. *Cooling of gases by laser radiation.* Opt. Commun. **13**, 68 (1975).

[Heil2012] A. Heilmann. *Production and characterisation of a mass separated lanthanum anion beam.* B. S. thesis, University of Heidelberg (2012).

[Hoto1975] H. Hotop and W. C. Lineberger. *Binding energies in atomic negative ions.* J. Phys. Chem. Ref. Data **4**, 539 (1975).

[Hoto1985] H. Hotop and W. C. Lineberger. *Binding Energies in Atomic Negative Ions II.* J. Phys. Chem. Ref. Data **14**, 731 (1985).

[Hu2007] S. X. Hu. *Producing ultracold and trappable antihydrogen atoms.* Phys. Rev. A **75**, 010501 (2007).

[Inge1973] S. Ingelman, C. Ekström, M. Olsmats, and B. Wannberg. *Nuclear Spins of Neutron-deficient Lanthanum and Cerium Isotopes.* Physica Scripta **7**, 24 (1973).

[Kaiv1985] M. Kaivola, O. Poulsen, E. Riis, and S. A. Lee. *Measurement of the Relativistic Doppler Shift in Neon.* Phys. Rev. Lett. **54**, 255 (1985).

[Kauf1976] S. L. Kaufman. *High-resolution laser spectroscopy in fast beams.* Opt. Commun. **17**, 309 (1976).

[Kell2006] A. Kellerbauer and J. Walz. *A novel cooling scheme for antiprotons.* New J. Phys. **8**, 45 (2006).

[Kell2008] A. Kellerbauer and *et al. Proposed antimatter gravity measurement with an antihydrogen beam.* Nucl. Instr. Meth. Phys. Res. Sec. B **266**, 351 (2008).

[Kell2011] A. Kellerbauer, C. Canali, A. Fischer, U. Warring, and S. Fritzsche. *Isotope shift of the electric-dipole transition in Os^{-}*. Phys. Rev. A **84**, 062510 (2011).

[Kell2014] A. Kellerbauer, A. Fischer, and U. Warring. *Measurement of the Zeeman effect in an atomic anion: Prospects for laser cooling of Os^{-}*. Phys. Rev. Lett. **89**, 043430 (2014).

[Kett2006] W. Ketterle. *Atomic and optical Physics Chapter 9 Two-Photon Excitation.* Massachusetts Institute of Technology (2006).

[Kopf1965] H. Kopfermann. *Kernmomente.* Akademische Verlagsgesellschaft M.B.H. Frankfurt a.M., 2nd edition (1965).

[Krec2010] H. Kreckel, H. Bruhns, K. A. Miller, E. Wåhlin, A. Davis, S. Höckh, and D. W. Savin. *A simple double-focusing electrostatic ion beam deflector.* Rev. Sci. Instrum. **81**, 063304 (2010).

[Li1997] G.-Z. Li, S. Guan, and A. G. Marshall. *Sympathetic cooling of trapped negative ions by self-cooled electrons in a fourier transform ion cyclotron resonance mass spectrometer.* J. Am. Soc. Mass Spectrom. **8**, 793 (1997).

[Loud1973] R. Loudon. *The quantum theory of light.* Oxford University Press Inc., New York, 3rd edition (1973).

[Magi2006] J. Magill, G. Pfennig, and J. Galy. *Karlsruher Nuklidkarte.* European Communities (2006).

[Meie2007] J. Meier. *Matching the beam form a negative-ion source for capture in a Penning trap.* Master's thesis, University of Heidelberg (2007).

[MH1998] H. R. McK. Hyder, J. Ashenfelter, and R. McGrath. *Production techniques for rare earth and other heavy negative ions.* Rev. Sci. Instrum. **69**, 1082 (1998).

[Mich1977] H. B. Michaelson. *The work function of the elements and its periodicity.* J. Appl. Phys. **48**, 4729 (1977).

[Midd1989] R. Middleton. *A negative-ion cookbook.* Electronic version prepared by Michael Wiplich, Brookhaven National Laboratory (1989).

[Monr1995] C. Monroe, D. M. Meekhof, B. E. King, S. R. Jefferts, W. M. Itano, D. J. Wineland, and P. Gould. *Resolved-Sideband Raman Cooling of a Bound Atom to the 3D Zero-Point Energy.* Phys. Rev. Lett. **75**, 4011 (1995).

[Neuh1978] W. Neuhauser, M. Hohenstatt, P. Toschek, and H. Dehmelt. *Optical-Sideband Cooling of Visible Atom Cloud Confined in Parabolic Well.* Phys. Rev. Lett. **41**, 233 (1978).

[Nigh2010] Y. Nighat, M. Raith, M. Hussain, and L. Windholz. *Investigation of the hyperfine structure of lanthanum lines by a laser-induced fluorescence technique.* J. Phys. B **43**, 125001 (2010).

[Norq1999] P. L. Norquist and D. R. Beck. *Binding energies, hyperfine structure, and magnetic dipole decay rates for* Os^{-} $5d^{7}6s^{2}{}^{4}F$ *levels.* Phys. Rev. A **61**, 014501 (1999).

[O'Ma2009] S. M. O'Malley and D. R. Beck. *Valence calculations of lanthanide anion binding energies:* $6p$ *and* $6s$ *attachments to* $4f^{m}5d+6s+6p^{3}$ *thresholds.* Phys. Rev. A **79**, 012511 (2009).

[O'Ma2010] S. M. O'Malley and D. R. Beck. *Lifetimes and branching ratios of excited states in* La^{-}*,* Os^{-}*,* Lu^{-}*,* Lr^{-}*, and* Pr^{-}. Phys. Rev. A **81**, 032503 (2010).

[Pan2010] L. Pan and D. Beck. *Candidates for laser cooling of atomic anions:* La^{-} *versus* Os^{-}. Phys. Rev. A **82**, 014501 (2010).

[Pegg1987] D. J. Pegg, J. S. Thompson, R. N. Compton, and G. D. Alton. *Evidence for a stable negative ion of calcium.* Phys. Rev. Lett. **59**, 2267 (1987).

[Pegg2004] D. J. Pegg. *Structure and dynamics of negative ions.* Rep. Prog. Phys. **67**, 857 (2004).

[Pegg2007] D. J. Pegg. *Correlated processes in negative ions.* Nucl. Instr. Meth. Phys. Res. B **261**, 138 (2007).

[Pene1988] F. Penent, R. L. Champion, L. D. Doverspike, V. A. Esaulov, J. P. Grouard, R. I. Hall, and J. L. Montmagnon. *Positive ion production in halogen negative ion collisions.* J. Phys. B **21**, 3375 (1988).

[Rein2009] P. Reinhed, A. Orbán, J. Werner, S. Rosén, R. D. Thomas, I. Kashperka, H. A. B. Johansson, D. Misra, L. Brännholm, M. Björkhage, H. Cederquist, and H. T. Schmidt. *Precision Lifetime Measurements of* He^{-} *in a Cryogenic Electrostatic Ion-Beam Trap.* Phys. Rev. Lett. **103**, 213002 (2009).

[Robb1911] A. A. Robb. *Optical geometry of motion.* W. Heffer and sons Ltd., Cambridge; Simpkin Marshall and Co. Ltd., London (1911).

[Sche1989] M. Scheer, C. A. Brodie, R. C. Bilodeau, and H. K. Haugen. *Laser spectroscopic measurements of binding energies and fine-structure splittings of* Co^{-} *,* Ni^{-} *,* Rh^{-} *, and* Pd^{-}. Phys. Rev. A **58**, 2051 (1989).

[SK2014] E. Stanca-Kaposta, F. Schwaneberg, M. R. Fagiani, T. Wende, F. Hagemann, and A. Wünschmann. *Infrared Photodissociation Spectroscopy of* $C_{2n+1}N^{-}$ *Anions with n=1–5.* Z. Phys. Chem. **228**, 351 (2014).

[Smit1978] G. P. Smith, L. C. Lee, P. C. Cosby, J. R. Peterson, and J. T. Moseley. *Photodissociation and photodetachment of molecular negative ions. V. Atmospheric ions from 7000 to 8400 A.* J. Chem. Phys. **68**, 3818 (1978).

[Stap1991] H. Stapelfeldt, C. Brink, and H. K. Haugen. *Two-photon detachment cross sections for O^- , Cu^- , Ag^- and Au^- at 1064 nm.* J. Phys. B **24**, L437 (1991).

[Ting1957] Y. Ting. *Hyperfine Structure and Quadrupole Moment of Lanthanum 139.* Phys. Rev. **108**, 295 (1957).

[Voge2013] J. S. Vogel. *Neutral resonant ionization in the high-intensity cesium sputter source.* AIP Conference Proceedings **1515**, 89 (2013).

[Vosk1991] S. H. Vosko, J. B. Lagowski, I. L. Mayer, and J. A. Chevary. *Theoretical study of even- and odd-parity states in La^- and Ac^-: Evidence for the uniqueness of La^-.* Phys. Rev. A **43**, 6389 (1991).

[Walt2007] C. W. Walter, N. D. Gibson, C. M. Janczak, K. A. Starr, A. P. Snedden, R. L. Field, and P. Andersson. *Infrared photodetachment of Ce^-: Threshold spectroscopy and resonance structure.* Phys. Rev. A **76**, 052702 (2007).

[Walt2011] C. W. Walter, N. D. Gibson, Y.-G. Li, D. J. Matyas, R. M. Alton, S. E. Lou, R. L. Field, D. Hanstorp, L. Pan, and D. R. Beck. *Experimental and theoretical study of bound and quasibound states of Ce^-.* Phys. Rev. A **84**, 032514 (2011).

[Walt2014] C. W. Walter, N. D. Gibson, D. J. Matyas, C. Crocker, K. A. Dungan, B. R. Matola, and J. Rohlén. *Candidate for Laser Cooling of a Negative Ion: Observations of Bound–Bound Transitions in La^-.* Phys. Rev. Lett. **113**, 063001 (2014).

[Warr2009] U. Warring, M. Amoretti, C. Canali, A. Fischer, R. Heyne, J. O. Meier, C. Morhard, and A. Kellerbauer. *High-Resolution Laser Spectroscopy on the Negative Osmium Ion.* Phys. Rev. Lett. **102**, 043001 (2009).

[Whit1933] H. E. White and A. Y. Eliason. *Relative Intensity Tables for Spectrum Lines.* Phys. Rev. **44**, 753 (1933).

[Wign1948] E. P. Wigner. *On the Behavior of Cross Sections Near Thresholds.* Phys. Rev. **73**, 1002 (1948).

[Wine1978] D. J. Wineland, R. E. Drullinger, and F. L. Walls. *Radiation-Pressure Cooling of Bound Resonant Absorbers.* Phys. Rev. Lett. **40**, 1639 (1978).

[Wine1987] D. J. Wineland, W. M. Itano, J. C. Bergquist, and R. G. Hulet. *Laser-cooling limits and single-ion spectroscopy.* Phys. Rev. A **36**, 2220 (1987).

[Yzom2015] P. Yzombard, M. Hamamda, S. Gerber, M. Doser, and D. Comparat. *Laser Cooling of Molecular Anions.* Phys. Rev. Lett. **114**, 213001 (2015).